



저작자표시-비영리-변경금지 2.0 대한민국

이용자는 아래의 조건을 따르는 경우에 한하여 자유롭게

- 이 저작물을 복제, 배포, 전송, 전시, 공연 및 방송할 수 있습니다.

다음과 같은 조건을 따라야 합니다:



저작자표시. 귀하는 원저작자를 표시하여야 합니다.



비영리. 귀하는 이 저작물을 영리 목적으로 이용할 수 없습니다.



변경금지. 귀하는 이 저작물을 개작, 변형 또는 가공할 수 없습니다.

- 귀하는, 이 저작물의 재이용이나 배포의 경우, 이 저작물에 적용된 이용허락조건을 명확하게 나타내어야 합니다.
- 저작권자로부터 별도의 허가를 받으면 이러한 조건들은 적용되지 않습니다.

저작권법에 따른 이용자의 권리는 위의 내용에 의하여 영향을 받지 않습니다.

이것은 [이용허락규약\(Legal Code\)](#)을 이해하기 쉽게 요약한 것입니다.

[Disclaimer](#)

이학박사 학위논문

천리안 해양위성의 대기보정 및 대리교정 연구

**A study on the atmospheric correction and vicarious calibration
for the Geostationary Ocean Color Imager**



2017년 2월


한국해양대학교 해양과학기술전문대학원

해양과학기술융합학과

안재현

본 논문을 안재현의 이학박사 학위논문으로 인준함.

위원장 노재훈 (인)
위원 박영제 (인)
위원 박경애 (인)
위원 이권호 (인)
위원 김원국 (인)



2016년 11월 29일

한국해양대학교 해양과학기술전문대학원

Table of Contents

List of Tables	v
List of Figures	vi
Abstract	xi
Chapter 1. Introduction	1
1.1 Ocean color remote sensing	1
1.2 Geostationary Ocean Color Imager (GOCI)	2
1.3 Atmospheric correction and vicarious calibration	5
Chapter 2. Initial atmospheric correction for the GOCI data	10
2.1 Introduction	10
2.2 Method	11
2.2.1 Correction for gaseous absorption and whitecap radiance	13
2.2.2 Solar irradiance normalization	15
2.2.3 Correction for molecular (Rayleigh) scattering	17
2.2.4 Cloud mask	18
2.2.5 Correction for multiple scattering by aerosols	19
2.2.6 Correction for atmospheric transmittance	22
2.2.7 Correction for near-infrared water reflectance over turbid waters	22
2.3 Conclusion	24
Chapter 3. Algorithm updates and vicarious calibration for the GOCI atmospheric correction	25
3.1 Backgrounds	25
3.2 Updates to the initial GOCI atmospheric correction algorithm	26
3.2.1 Correction for gaseous absorption and whitecap radiance	26
3.2.2 Sun-glint correction	28
3.2.3 Considering gravity effect for Rayleigh scattering	29

3.2.4 Correction for multiple scattering by aerosols - SRAMS	30
3.2.5 Correction for bidirectional effects for water reflectance	35
3.2.6 Correction for near-infrared water reflectance over turbid waters	39
3.2.7 Atmospheric transmittance with considering anisotropic angular distribution of water reflectance	40
3.3 Vicarious calibration of GOCI near-infrared bands	41
3.3.1 Method	44
3.3.2 Inter-calibration of GOCI near-infrared bands	45
3.3.3 Vicarious calibration of GOCI visible bands	49
Chapter 4. Validation results	51
4.1 Data	51
4.1.1 Synthetic data derived by simulations	51
4.1.2 <i>In situ</i> radiometric data measured from shipboard	52
4.1.3 AERONET-OC radiometric data	56
4.2 Validation of SRAMS scheme with simulation data	58
4.3 Assessment of the atmospheric correction improvements with <i>in situ</i> radiometric data	59
Chapter 5. Discussions	61
5.1 Impacts of water vapor correction on ocean color products	61
5.2 Stability for high solar and satellite zenith angle for diurnal observation	62
5.3 Cloud masking on fast-moving clouds and quality analysis	63
5.4 Evaluation of the GOCI aerosol correction scheme compared with other approaches	64
5.4.1 Aerosol correction approach for OCTS	64
5.4.2 Aerosol correction approach for MERIS	67
5.4.3 Evaluation results	69
5.5 Pitfalls in estimation of aerosol reflectance using 2-NIR bands	71
5.6 Issues in the vicarious calibration of GOCI VIS and NIR bands	72

5.7 Uncertainties from bidirectional effect	75
Chapter 6. Conclusion	76
Appendix. Glossary of symbols	81
Acknowledgements	85
References	87



List of Tables

Table 1. Specification of the GOCI observation (Cho et al., 2009)	4
Table 2. Characteristics of the spectral bands of GOCI (Ryu et al., 2012)	4
Table 3. Statistics (mean and RMSE) of atmospheric correction's validation results for two types of waters with different bands (Ahn et al., 2012)	9
Table 4. Comparison of the SeaWiFS atmospheric correction algorithm with the GOCI algorithm	24
Table 5. Derived coefficients for the water vapor absorption model	28
Table 6. Summary of the spectral relationships for GOCI bands	22
Table 7. Adjusted coefficients (Eq.(37)) for GOCI bands (Wang, 2006; Ahn et al., 2015)	37
Table 8. Statistics of R_{rs} match-ups for KOSC cruises and AERONET-OC	60
Table 9. Summary of primary schemes to correct aerosol reflectance with using 2 NIR bands for determining aerosol optical properties	64
Table 10. Summary of the GOCI atmospheric correction algorithm developed for GDPS version 1.1 and 1.5	77

List of Figures

Fig. 1. Ocean color spectra can be varied by various water constituents such as phytoplankton, suspended sediments, and dissolved organic matter. Photos were taken by the Korea Ocean Satellite Center of the Korea Institute of Ocean Science and Technology (KIOST) during the KORUS-OC 2016 campaign from 2016/05/20 to 2016/06/06 (Mannino, 2015; Kim et al., 2016; Salisbury, 2016).	1
Fig. 2. Past and future ocean color missions. The first Geostationary Ocean Color Imager (GOCI) has been successfully launched and operated since 2010 with 7.5 years lifetime. ..	2
Fig. 3. The main unit of the GOCI without multi-layer insulation protection (left) and Communication-Ocean-Meteorological Satellite (COMS) geostationary satellite (right). GOCI is one of three payloads onboard COMS (Faure et al., 2008; Kang et al., 2010)	3
Fig. 4. GOCI observes ocean environment of the Northeast Asia area from a geostationary orbit (Kang et al., 2010)	3
Fig. 5. GOCI RGB (660 nm, 555 nm, and 443 nm, respectively) composite images of TOA reflectance in same color scale before the atmospheric correction (a), and water reflectance after the atmospheric correction (b) over the East Sea. The example imagery are obtained in 2011/04/05 03:16 UTC	5
Fig. 6. Spectra of TOA radiance contributors at 2011/04/05 03:16 UTC, in the middle of East Sea, from GOCI observation. In the observation, water-leaving radiance to atmospheric path radiance is less than ~7% in blue bands	6
Fig. 7. Contributors of the TOA radiance. (a) Multiply scattered radiance by air molecules (Rayleigh scattering), (b) multiply scattered radiance by aerosols, (c) radiance by interactions between air molecules and aerosols, (d) water-leaving radiance that has to be retrieved eventually	12
Fig. 8. Flow chart describing the overall atmospheric correction process	13
Fig. 9. Temporal sequence of each band and slot acquisition	16

Fig. 10. An example of Rayleigh reflectance correction (2013/08/13 03:16 UTC). (Left) Rayleigh reflectance at 555 nm. (Right) Rayleigh corrected reflectance ($\rho_{TOA} - \rho_r$) at 555 nm	18
Fig. 11. An example result of cloud masking for both clear and turbid waters (2011/04/05 03:16 UTC). Left image is Rayleigh corrected reflectance at 865 nm and right image is result of cloud screening	19
Fig. 12. Scheme of the $\rho_{am}(VIS)$ estimation used by SeaWiFS and initial GOCI atmospheric correction (Gordon and Wang, 1994; Wang and Gordon, 1994; Ahn et al., 2012). The method uses the relationship between single-scattering and multiple-scattering aerosol reflectance to select optimum aerosol models.	21
Fig. 13. Flow chart of the turbid water $\rho_{wm}(NIR)$ correction scheme for the GOCI standard atmospheric correction (Ahn et al., 2012, 2015)	23
Fig. 14. Water vapor and oxygen absorption spectra in red and NIR bands. Both the oxygen and water vapor absorption spectrum is crossing in the range of out-of-band responses	26
Fig. 15. Radiative transfer simulation (6SV version 2.1) results for the gaseous transmittance of water vapor absorption at 660, 745, and 865 nm with water vapor concentration ranging from 0 to 9 g/cm ² and solar or sensor zenith angle ranging from 0 to 85°	27
Fig. 16. The 2 nd order polynomial relationships between $\ln\{-\ln(wv)\}$ and $\ln\{(1/\cos\theta_s + 1/\cos\theta_v) \times wv\}$ for 660, 745, and 865 nm	27
Fig. 17. Verification results of the established water vapor correction model with simulations	28
Fig. 18. An example of sun-glint reflectance (2013/08/13 03:16 UTC) estimated by Cox & Munk (1955)	29
Fig. 19. Earth gravity for various latitudes and altitudes (Bodhain et al., 1999). The gravity at the surface (0 m altitude) is varied ~0.53% with depending on the latitude	30
Fig. 20. (a) Spectral dependence of ρ_{am} for a range of aerosol optical depth $\tau_a(865)$ from 0.01 to 1.2 for the maritime aerosol model with RH = 50% and solar-sensor geometries $\theta_s=60^\circ$, $\theta_v=40^\circ$, $\phi_{sv}=40^\circ$. (b) Spectral relationships between aerosol multiple-scattering reflectances at several	

wavelengths for the same aerosol model and solar-sensor geometries.	32
Fig. 21. Flow chart describing the process of SRAMS approach for estimating $\rho_{am}(\text{VIS})$ from $\rho_{am}(\text{NIR})$	34
Fig. 22. Impacts of bidirectional effect on level-2 product, $R_{rs}(555 \text{ nm})$ and Chl_a	35
Fig. 23. An example of BRDF correction factor (c_{BF}) at 555 nm in the GOCI atmospheric correction process (2011/08/13, 3:16 UTC) (Morel et al., 2005; Wang, 2006; Ahn et al., 2015)	38
Fig. 24. Relationships between $\rho_{wn}(660 \text{ nm})$ and $\rho_{wn}(745 \text{ nm})$ and $\rho_{wn}(865 \text{ nm})$. The dashed line represents the linear relationship from the model of Ruddick et al. (2006) that the ratio of $\rho_{wn}(745 \text{ nm})$ to $\rho_{wn}(865 \text{ nm})$ is 1.936 used in Ahn et al. (2012)	39
Fig. 25. Conceptual diagram of the vicarious calibration	43
Fig. 26. Map of the calibration site for the GOCI NIR bands. Region within the box of 25.7-26.7°N and 138.4-139.4°E (red rectangle) in the GOCI coverage is established for the NIR vicarious calibration. The region is selected so as to avoid continental aerosols and slot boundary stray-light effects. NIR calibration sites previously established by Wang et al. (2013a) and Ahn et al. (2015) are discarded in this study	46
Fig. 27. Flow chart describing the scheme for estimating the TOA radiance at 745 nm	48
Fig. 28. The result of NIR bands inter-calibration with/without considering the water vapor effect. In the NIR calibration site, water vapor effects the $g_{vc}(745 \text{ nm})$ more than 0.5%	48
Fig. 29. A flow chart describing the scheme for estimating the TOA radiance in the visible bands	49
Fig. 30. The result of the VIS band calibration. Blue marks and red marks are match-ups without/with the calibration in clear waters, respectively	50
Fig. 31. Remote-sensing reflectance for chl_a concentrations 0.03, 0.1, 0.3, and 1.0 mg/m^3 without inorganic particulate 0.03, 0.1, 0.3, and 1.0 mg/m^3 by using biogenic ocean color model (Morel and Maritorena, 2001)	52
Fig. 32. Locations of <i>in situ</i> radiometric measurements in coastal and open-ocean waters around Korea. A total of 421 samples were collected, and subsequently reduced to 65	

(blue diamonds) through strict quality control of both the *in situ* measurements and GOCI observations. Of these data, only 14 spectra were used in the vicarious calibration process (green squares) 53

Fig. 33. R_b correction applied to $R_{rs}^m(\lambda)$ from clear (a) and turbid (b) waters. Red solid lines represent the corrected R_{rs} , and black dotted lines indicate uncorrected data directly derived from Eq. (57) with R_b is zero. Grey dashed lines show the results obtained by subtracting the $R_{rs}(755\text{ nm})$ value from each wavelengths (Mobley, 1999) 55

Fig. 34. R_{rs} spectral relationships obtained through HYDROLIGHT simulations (Ahn et al., 2015). For this simulation, the range of chl_a concentration varied from 0.1~30 mg m^{-3} , CDOM absorption at 440 nm from 0.1~0.3 m^{-1} , and suspended sediment concentration from 0.1~1000 g m^{-3} 57

Fig. 35. Quality control adopted for the AERONET-OC data (Ahn et al., 2015).
 (a) R_{rs} spectra accepted by the quality control screening criteria.
 (b) R_{rs} spectra rejected by the scheme because of spurious outliers 58

Fig. 36. Validation results from simulation data; the aerosol reflectance error $\Delta\rho_{am}$ for the SRAMS (a) and the SSE scheme (b), and errors in the ρ_{wn} , the chl_a , aerosol optical thickness at 555 nm (AOT555), and the Ångström exponent for 443 nm relative to 865 nm (Å) in the absolute percentage deviation (APD) for the SRAMS (c) and the SSE scheme (d). (Ahn et al., 2016) 59

Fig. 37. Validation result of *in situ* R_{rs} match-ups for the previous (Ahn et al., 2012) and the improved (this thesis) atmospheric correction. *In situ* R_{rs} are collected from KOSC cruises for 2010~2016 and AERONET-OC sites 60

Fig. 38. Water vapor correction impacts on the GOCI R_{rs} in percentage difference 61

Fig. 39. Water vapor correction impacts on the GOCI chl_a in percentage difference.
 (a) Chl_a is derived by band ratio (blue/green) algorithm (O'Reilly et al., 1998).
 (b) Chl_a is derived by fluorescence line height algorithm (Gower, 1980; Gower and Borstad, 1981) 62

Fig. 40. (a) Aerosol reflectance at NIR used by atmospheric correction process. In the scene,

aerosol pattern shows high spatial frequency and fast-moving in winter.

(b) Atmospheric correction result over fast moving aerosols. R_{rs} at 443 nm shows spatially scattered values at fast-moving aerosol edge.

(c) Significantly chl_a overestimated results represented as speckles due to erroneously produced R_{rs} 63

Fig. 41. Scheme of the $\rho_{am}(VIS)$ estimation used by OCTS atmospheric correction (Fukushima et al., 1998). The method uses relationship between AOT and multiple-scattering aerosol reflectance to select optimum aerosol model 66

Fig. 42. Scheme of the $\rho_{am}(VIS)$ estimation used by MERIS atmospheric correction (Antoine and Morel, 1999; Antoine, 2010) 68

Fig. 43. Accuracy of relationships test used for each $\rho_{am}(VIS)$ estimation scheme for SeaWiFS, OCTS, MERIS and GOCI algorithms. For moderate solar/sensor zenith angles, errors during the aerosol reflectance estimation is less than 0.003 69

Fig. 44. Comparison result of the SRAMS scheme with other three major methods by the radiative transfer simulations. The assessment is performed for not only candidate aerosol models but also different aerosol models. Two of the most accurate schemes are the MERIS approach and the SRAMS-based method which select aerosol models in multiple-scattering domain 70

Fig. 45. Analysis results for 745 nm calibration gain sensitivity to calibration site. Furthestmost site (site 3) has the least scattered result 73

Fig. 46. The result of NOAA HYSPLIT model (Stein et al., 2015) to trace one-week backward aerosol trajectories of GOCI NIR calibration site (at 300 and 1500 m altitude) in winter (2015/12/26 ~ 2016/01/01). This result indicates that the NIR calibration site may be affected by continent aerosols 74

정지궤도 해색센서를 위한 원격반사도 추정 알고리즘

안 재 현

Department of Convergence Study on the Ocean Science and Technology

Graduate School of

Ocean Science and Technology School

요 약 문

본 학위논문은 세계최초의 정지궤도 해색 위성인 천리안 해양 위성 (GOCI : Geostationary Ocean Color Imager)에 표준으로 사용되는 대기보정 이론에 대하여 기술하고 있다. 타 극궤도 해색위성들이 1~2일 주기로 한 장소를 방문하며 전 지구를 관측하는 것과 달리 천리안 해양위성은 한반도를 포함한 동북아해역을 0.5 km 공간해상도로 낮 시간 동안 1시간의 시간간격으로 관측하고 있으며 (하루 8회 관측) 가시광~근적외파장대 (412, 443, 490, 555, 660, 680, 745, 865 nm) 영역에서 관측한다.

대기상층 위성궤도에서 일반적인 맑은 해역을 대상으로 관측된 가시광~근적외파장대 신호 중 90%이상은 대기신호이며, 해수신호의 크기는 10% 미만을 차지한다. 대기신호의 크기가 해수신호의 크기보다 10배 이상 크기 때문에 1%의 대기신호 추정 오차는 10%이상의 해수 광 스펙트럼 추정오류를 일으킨다. 이런 이유로 위성을 통한 해색원격탐사 임무는 높은 대기보정 정밀도를 요구하고 있으며 대기보정의 개발이 해색원격탐사 알고리즘 개발 중 가장 핵심이 된다.

천리안 해양위성 표준 대기보정은 NASA가 해색원격탐사 임무를 위해 개발한

SeaWiFS 표준 대기보정에 이론적인 기반을 두고 있다. SeaWiFS 방법은 우선 두개의 근적외 파장대 관측결과와 복사전달시뮬레이션 결과(조건표)를 서로 비교하여 대기 중 에어로졸 입자의 종류 및 농도 최적값을 추정해 내며 이 추정결과를 바탕으로 모든 가시광 파장의 에어로졸 반사도 스펙트럼을 다시 조건표를 이용하여 계산한다. 천리안 해양위성의 대기보정도 유사하게 두 근적외파장대 에어로졸 반사도 상관관계를 이용하여 에어로졸 종류 및 농도를 계산하는데, 이 연구를 통하여 SeaWiFS 및 다른 유사 대기보정 방법들과 비교하여 정확도 뿐 아니라 계산 효율 또한 개선하였다. 추가적으로 SeaWiFS에 적용된 수증기 흡광 보정 모델을 천리안 해양위성의 분광특성에 맞게 수정하여 적용하였으며, 탁도가 높은 해역에서 대기보정 오차를 줄이는 방법도 천리안 해양위성 관측영역의 해수 광 특성 및 반사도 정보들을 이용하여 개발하였다.

초기버전의 천리안 해양위성 표준 대기보정의 검보정 결과 탁도가 높은 연안해역에서는 10% 내외의 만족할 만한 오차수준을 보여주었으나, 탁도가 낮은 해역에서는 50% 이상의 오차를 발생되었다. 이는 대리교정 수행의 부재가 주된 요인이며, 본 연구에서는 이를 보완하기 위해 SeaWiFS 표준 대리교정 프로세스에 기반을 두고 천리안 해양위성에 맞게 대리교정을 수행하였다. 이 대리교정 방법에서는 특정 해역의 에어로졸 광특성이 항상 해양성 에어로졸이라 가정하고 이를 바탕으로 근적외 파장대 위성 관측 조도를 시뮬레이션 하여 두 근적외 파장대를 먼저 상대교정 한다. 이후, 상대교정된 두 근적외 파장대를 이용하면 맑은 해역에서 복사전달시뮬레이션을 통하여 가시광 파장대 대기조도를 모의 할 수 있게 되고, 여기에 맑은 해역의 현장 광 측정 자료가 추가되면 가시광파장대 위성관측조도의 시뮬레이션이 가능하다. 이 가시광파장대 모의 결과와 실제 위성관측조도와 비교하면 가시광파장대 대리교정을 완료할 수 있다. 본 대리교정 결과 대리교정 상수가 최대 3.2% 바뀌었으며 (490 nm 밴드) 새 대리교정 상수 적용 시 맑은 해역 대기보정 정확도가 최대 50% 이상 상승하였다.

본 연구에서는 천리안해양위성 대기보정의 성능을 평가하기 위해서 대기보정

결과 원격반사도 (remote-sensing reflectance: R_{rs})를 한국해양과학기술원 해양위성연구센터에서 2010년 이후로 한반도 주변 해역 현장조사를 통해 수집한 원격반사도 자료들과 비교검정 하였으며, 검정결과 76, 84, 88, 90, 81, 82%의 정확도를 보여주었다. 추가로 현장자료가 아닌 시뮬레이션 자료를 통해 천리안 해양위성 알고리즘 뿐 아니라 다른 해색원격탐사 임무를 위해 개발된 주요 대기보정 알고리즘들 구현하여 함께 비교검증 하였고, 본 비교검증에서도 천리안 해양위성 표준 대기보정이 다른 대기보정 방법들과 비교하여 가장 낮은 오차율을 보여주었으며, 특히 다중산란 효과가 큰 작은 입자크기의 에어로졸 모델에서 더 좋은 성능을 보여주었다.

본 연구결과는 이론적으로 SeaWiFS 등 비슷한 밴드 특성을 가진 타 해색위성의 대기보정방법으로도 적용이 가능하며, 천리안 해양위성 자료처리시스템 (GOCI data processing system: GDPS) 1.5버전에서의 적용될 예정이다.

주요어 : 천리안, 대기보정, 대리교정, 해색, 원격탐사

keywords: GOCI, atmospheric correction, vicarious calibration, ocean color, remote sensing

Chapter 1. Introduction

1.1. Ocean color remote sensing

The ocean color represents characteristics of oceanic environmental parameters by light (from the sun) interactions with underwater constituents such as phytoplankton, inorganic suspended particles, detritus, dissolved organic matter (Morel and Puieur, 1977; Mobley, 2010) as shown in Fig. 1. Remotely sensing the oceanic environment using from visible (VIS) to near infrared (NIR) wavelengths at a satellite level has successfully extracted oceanic environmental information in a large spatial and temporal scale. At the initial phase of the ocean color mission, it had focused on a monitoring of chlorophyll-a (chl_a) concentration that indicates an abundance of phytoplankton on the ocean. This monitoring has made the study of a global-scale biogeochemical dynamics and cycle possible (Gordon et al., 1980, 1983).

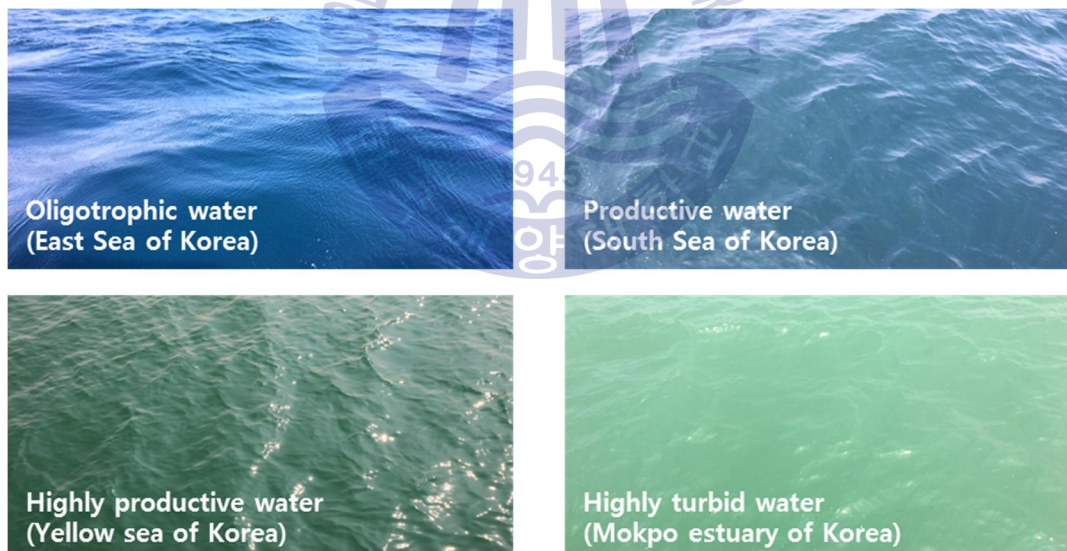


Fig. 1. Ocean color spectra can be varied by various water constituents such as phytoplankton, suspended sediments, and dissolved organic matter. Photos were taken by the Korea Ocean Satellite Center of the Korea Institute of Ocean Science and Technology (KIOST) during the KORUS-OC 2016 campaign from 2016/05/20 to 2016/06/06 (Mannino, 2015; Kim et al., 2016; Salisbury, 2016).

Since the first ocean color satellite Coastal Zone Color Scanner (CZCS) launched in 1978, the ocean color remote sensing research has been developed rapidly. Because satellite remote-sensing data can be acquired by several series of ocean color missions (Fig.2) from a large area and fast access. The growth of ocean color remote sensing technique has involved an extension of coastal environment monitoring and its diurnal variations.

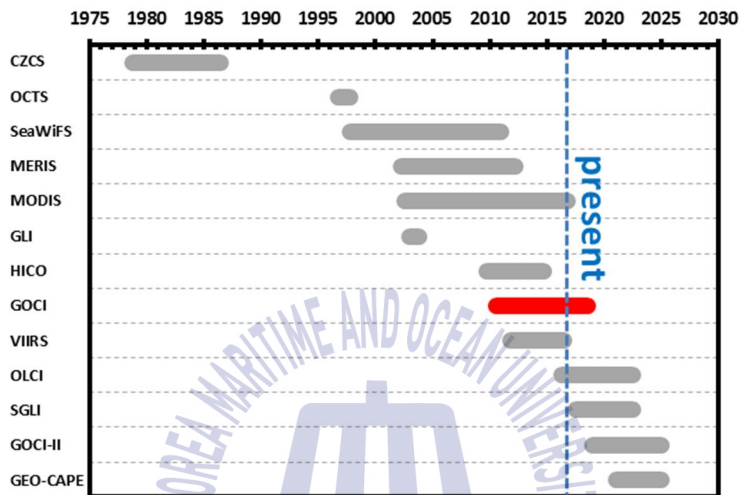


Fig. 2. Past and future ocean color missions. The first Geostationary Ocean Color Imager (GOCI) has been successfully launched and operated since 2010 with 7.5 years lifetime.

1.2. Geostationary Ocean Color Imager (GOCI)

The first Geostationary Ocean Color Imager (GOCI) is one of the three payloads on the Communication-Ocean-Meteorological Satellite (COMS) (Fig. 3) operated by Korea Ocean Satellite Center (KOSC) of Korea Institute of Ocean Science and Technology (KIOST). From the geostationary orbit, GOCI has provided the regional synoptic perspectives of coastal and open ocean phenomena around the Northeast Asia Seas (Fig. 4). It is the first space-borne ocean color sensor that can take daytime images with unprecedented temporal resolution (8 times a day from 09:15 to 16:15, local time GMT+9) at six visible bands (412, 443, 490, 555, 660, and 680nm) and

two NIR bands (745 and 865nm) and a moderate spatial resolution (~500m at the scene center) (Faure et al., 2008; Kang et al., 2010; Ryu and Ishijaka, 2012; Ryu et al., 2012). Further descriptions of specifications associated with requirements and spectral requirements are tabulated in Table 1 and Table 2 (Cho et al., 2009; Ryu et al., 2012), respectively

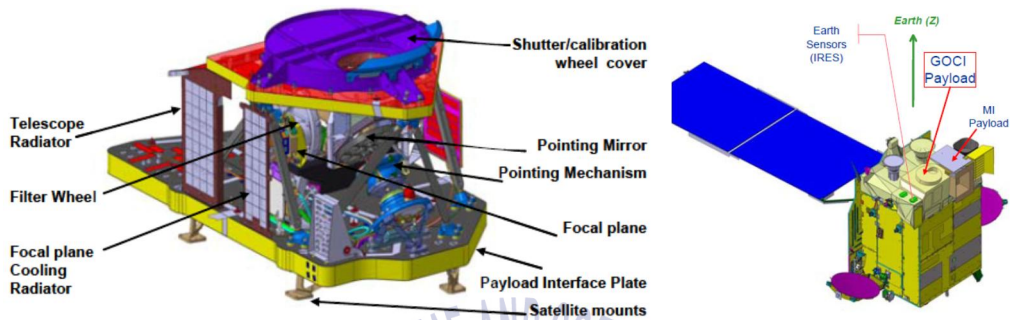


Fig. 3. The main unit of the GOCI without multi-layer insulation protection (left) and Communication-Ocean-Meteorological Satellite (COMS) geostationary satellite (right). GOCI is one of three payloads onboard COMS (Faure et al., 2008; Kang et al., 2010).

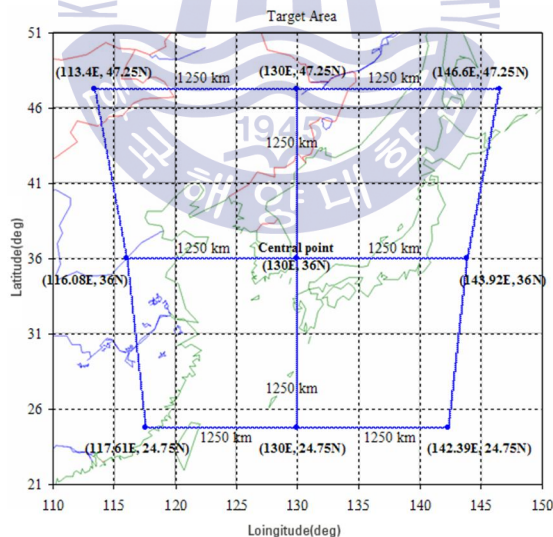


Fig. 4. GOCI observes ocean environment of the Northeast Asia area from a geostationary orbit (Kang et al., 2010).

Table 1. Specification of the GOCI observation (Cho et al., 2009).

Detector	CMOS (2D, 1415×1432 pixels)
Image capture (sequence)	2D Staring frame capture Dark Signal → High gain → Low gain → Dark Signal
Radiometric Calibration	Solar diffuser & DAMD(Diffuser Aging Monitoring Device)
Resolution (GSD)	500m×500m
Total FOV	16 slots, 5,300×5,300 Pixels
Coverage	2,500km×2,500km
Longitude	128.2°E
Altitude	35,786km
Pupil Diameter of Pointing Mirror	140mm
SNR	> 1,000
MTF	> 0.3
Number of Spectral Bands	8 Bands (6-Visible and 2-NIR)
Digitization	≥ 12 bits

Table 2. Characteristics of the spectral bands of GOCI (Ryu et al., 2012)

Band	Center wavelength	Band width	SNR	Type	Primary application
B1	412nm	20nm	1000	Visible	Dissolved organic carbon absorption
B2	443nm	20nm	1090	Visible	<i>Chl_a</i> absorption
B3	490nm	20nm	1170	Visible	<i>Chl_a</i> absorption, suspended sediment absorption
B4	555nm	20nm	1070	Visible	Backscattering of suspended particles (phytoplankton or sediments)
B5	660nm	20nm	1010	Visible	<i>Chl_a</i> absorption, backscattering of suspended sediment, vegetation
B6	680nm	10nm	870	Visible	Fluorescence emission of <i>chl_a</i>
B7	745nm	20nm	860	NIR	Atmospheric correction
B8	865nm	40nm	750	NIR	Atmospheric correction, vegetation

1.3. Atmospheric correction

The GOCI remotely senses ocean color information from geostationary orbit (altitude: ~36,000km) compare to sun-synchronous orbit sensors (altitude: ~700km). Extracting the water-leaving radiance from total radiance recorded at the top-of-atmosphere (TOA), however, contains more than 90% of atmospheric path radiance resulted from multiple-scattering of light by air molecules and aerosols including their interactions (Fig. 5 and 6) (Gordon, 1998; Eplee et al., 2001; Wang and Gordon, 2002; Franz et al., 2007). Therefore, the atmospheric correction is an essential process for the ocean color remote sensing including the GOCI mission. The atmospheric correction is a sensitive process due to the relatively low ratio of water radiance to atmospheric radiance, i.e. 1% error in estimation of the atmospheric radiance would cause more than 10% error in the ocean radiance estimation (Eplee et al., 2001).

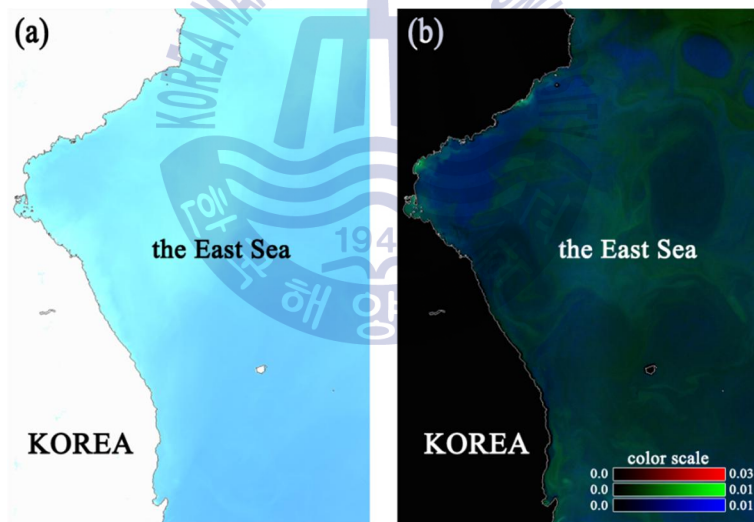


Fig. 5. GOCI RGB (660 nm, 555 nm, and 443 nm, respectively) composite images of TOA reflectance in same color scale before the atmospheric correction (a), and water reflectance after the atmospheric correction (b) over the East Sea. The example imagery have been obtained in 2011/04/05 03:16 UTC.

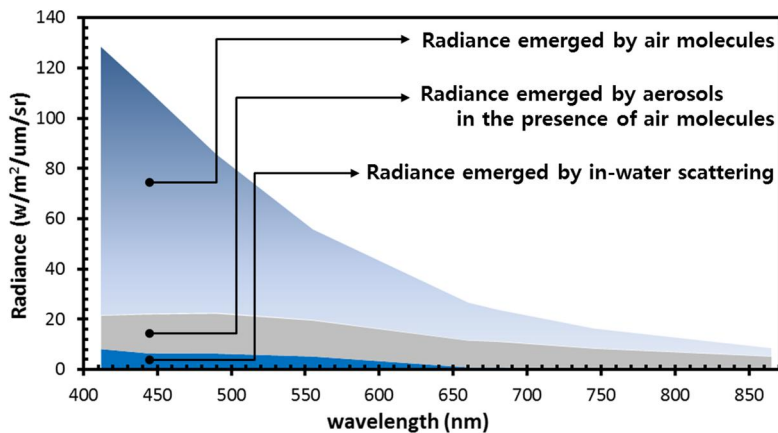


Fig. 6. Spectra of TOA radiance contributors at 2011/04/05 03:16 UTC, in the middle of the East Sea, from GOCI observation. In the observation, water-leaving radiance to atmospheric path radiance is less than ~7% in blue bands.

Earlier atmospheric correction for the ocean color remote sensing considered only the open seas. Thus it assumed that the water-leaving radiance is negligible in the near-infrared (NIR) spectral range and is called a black pixel assumption (BPA). The BPA has made possible to know the atmospheric radiance in NIR wavelengths over the ocean. The initial BPA-based atmospheric correction algorithm was first developed for the CZCS data processing by Gordon (1978, 1983). This algorithm is based on the single-scattering approximation for aerosol particles. For low aerosol optical thickness (AOT) conditions (i.e., $AOT < 0.1$), this single-scattering-based atmospheric correction had worked acceptably. Later, an improved atmospheric correction algorithm considering a multiple-scattering for various aerosol type for the operational data processing of the Sea-viewing Wide Field-of-view Sensor (SeaWiFS) was developed by Gordon and Wang (1994) and Wang and Gordon (1994). This algorithm is an update version of the CZCS approach regarding the aerosol correction scheme. Thus the process first converted the multiple-scattering into the single-scattering to select aerosol models and extrapolate aerosol's single-scattering reflectance in NIR band to VIS bands. After the aerosol model selection, the aerosol single-scattering reflectances in the VIS bands are converted back into the VIS bands. Later, the SeaWiFS algorithm was slightly modified for the Ocean Color and Temperature Scanner (OCTS) by Fukushima et al. (1998). The OCTS algorithm replaced the single-scattering reflectance to the AOT to simplify the process, and subsequently

enhanced the aerosol model selection scheme with considering weighted-average technique. More recently, a new multiple-scattering atmospheric correction algorithm was developed by Antoine and Morel (1999) for the Medium Resolution Imaging Spectrometer (MERIS) data processing. The MERIS algorithm also converts the multiple-scattering reflectance to the AOT similar to the OCTS approach. However, it selects the appropriate aerosol models in the multiple-scattering space. The performance of those three primary algorithms was evaluated by the International Ocean-Colour Coordinating Group (IOCCG) report No. 10 (2010), and it showed all of three algorithms were working well within the acceptable error range (– less than 5% error in the blue band for general sun-sensor geometries).

The GOCI atmospheric correction algorithm is also developed based on the SeaWiFS and CZCS atmospheric correction approach with partial improvements with focusing on aerosol correction scheme, turbid water NIR correction, and vicarious calibration (Ahn et al., 2012, 2015, 2016). The aerosol correction scheme in the GOCI standard atmospheric correction algorithm is developed to overcome some assumptions and limitations associated with existing methods that rely on either single-scattering reflectance or aerosol optical depth. The new aerosol correction scheme is simpler and methodologically more straightforward. Moreover, it estimates the aerosol multiple-scattering reflectances at the visible wavelengths more accurately by using the spectral relationships in the aerosol multiple-scattering reflectance between different wavelengths (called SRAMS).

To extend the ocean color remote sensing to the coastal environment monitoring, atmospheric correction over turbid water (where the BPA is not valid) has become important. Several studies has addressed the atmospheric correction over the turbid waters (Hu et al., 2000; Ruddick et al., 2000; Siegel et al., 2000; Wang and Shi, 2007; Stumpf et al., 2003; Bailey et al., 2010; Wang et al., 2012; Jiang and Wang, 2014). Especially, the GOCI coverage contains highly turbid water areas such as the Yellow Sea, the East China Sea, and the coastal areas of the Korean peninsula. Thus, an implementation of the GOCI atmospheric correction algorithm can be applied to both the turbid waters and the clear waters. This study also focuses on an improvement of the turbid water (i.e., inorganic particles are dominant) atmospheric correction for GOCI target area. A strong empirical relationship between water reflectances derived by satellite at red and two NIR bands can be

established in a wide range of water turbidity. The GOCI atmospheric correction process iteratively separates water reflectance and multiple-scattering reflectance of aerosols by the empirical relationship model.

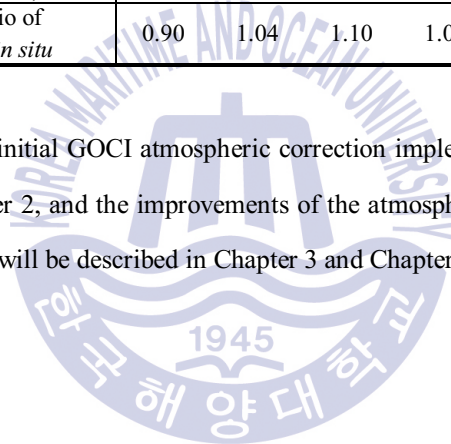
The vicarious calibration is applied to the GOCI data to enhance the agreement between the actual observation and the atmospheric correction system (Ahn et al., 2015). The validation of the first GOCI standard atmospheric correction implemented in the GOCI Data Processing System (GDPS) Version 1.1 (Moon et al., 2012; Ahn et al., 2012) in the turbid waters showed errors around 10% in the blue and green bands (412, 443, 490, and 555 nm) and errors around 15% in red bands (660 and 680 nm) (Table 3 – turbid waters), indicating that the correction for NIR water reflectance works reasonably. However, for clear waters, there still exist considerable discrepancies between the *in situ* measurements and the water-leaving radiance derived after the atmospheric correction in the blue to green bands (412, 443, 490 and 555 nm), most likely because a vicarious calibration has not been applied to the GOCI data (Table 3 – clear waters). The vicarious calibrations can be normally applied in the satellite ocean color missions (Gordon, 1998; Eplee et al., 2001; Wang and Gordon, 2002; Murakami et al., 2005; Lerebourg et al., 2011; Werdell et al., 2007; Franz et al., 2007; Wang et al., 2013a, 2013b, Ahn et al., 2015), since small calibration errors in an atmospheric correction algorithm can cause significant differences in the derived value of normalized water-leaving radiance (nL_w). Only a 1% increase of the TOA radiance with the same atmospheric radiance can cause more than a 10% change of the satellite-derived value of nL_w (Gordon, 1998; Eplee et al., 2001; Wang and Gordon, 2002; Franz et al., 2007; Ahn et al., 2012; Ahn et al., 2015).

The vicarious calibration approach described here relies on the assumed constant aerosol characteristics over the open-ocean sites to accurately estimate atmospheric radiances for the two near-infrared (NIR) bands. The vicarious calibration of visible bands is performed using *in situ* water-leaving radiance measurements and the satellite-estimated atmospheric radiance using two NIR bands over the case-1 waters. These gain factors are independent of angular geometry and possible temporal variability.

Table 3. Statistics (mean and RMSE) of atmospheric correction's validation results for two types of waters with different bands (Ahn et al., 2012)

parameters		412nm	443nm	490nm	555nm	660nm	680nm
all waters	mean value of <i>in situ</i> nLw (w/m ² /um/sr)	11.29	14.75	19.25	17.75	4.80	4.21
	root mean square error (w/m ² /um/sr)	4.43	3.26	2.98	2.66	1.37	0.98
	mean ratio of derived / <i>in situ</i>	1.17	1.24	1.26	1.15	0.86	1.00
clear waters	mean value of <i>in situ</i> nLw (w/m ² /um/sr)	6.08	6.42	6.89	4.96	0.89	0.89
	root mean square error (w/m ² /um/sr)	2.74	2.32	2.07	1.26	0.53	0.37
	mean ratio of derived / <i>in situ</i>	1.56	1.54	1.51	1.18	0.56	0.93
turbid waters	mean value of <i>in situ</i> nLw (w/m ² /um/sr)	13.89	18.92	25.42	24.14	6.76	5.88
	root mean square error (w/m ² /um/sr)	4.32	2.86	2.66	2.91	1.57	1.13
	mean ratio of derived / <i>in situ</i>	0.90	1.04	1.10	1.04	0.83	0.88

Further description of the initial GOCI atmospheric correction implemented in GDPS version 1.1 will be introduced in Chapter 2, and the improvements of the atmospheric correction developed by this thesis and its validation will be described in Chapter 3 and Chapter 4, respectively.



Chapter 2. Atmospheric correction for the GOCI data

2.1. Introduction

To retrieve colored water constituents such as chl_a or suspended sediment concentrations by ocean color remote sensing, accurate estimations of the water-leaving radiance or reflectance are required. To extract the precise amount of radiance emerging from the ocean, atmospheric radiances due to the molecular and aerosol scattering must be accurately retrieved from satellite-measured radiances. Because these atmospheric radiances can account for more than 90% of the total satellite-measured radiances, i.e., a 1% error in the atmospheric correction can cause more than 10% error in ocean radiance estimations (Eplee et al., 2001).

Initial atmospheric correction algorithms for ocean color assumed that the ocean radiance is negligible at the near-infrared (NIR) spectral range, implying that only atmospheric radiance remains in these bands in what is known as the black pixel assumption (Gordon, 1978). This atmospheric correction algorithm with its black pixel assumption methodology was initially developed for the Coastal Zone Color Scanner (CZCS) by Gordon (1978) and Gordon and Clark (1983). This algorithm is based on the single-scattering approximation for atmospheric particles. When the aerosol optical thickness (AOT) is less than 0.1, this single-scattering-based estimation scheme is approximately reasonable. For more general cases and better accuracy, improved atmospheric correction applied by a multiple-scattering and per-pixel aerosol model was developed for the SeaWiFS by Gordon and Wang (1994). The algorithm uses the single-scattering epsilon (SSE) that is the ratio of the aerosol single-scattering reflectance between two wavelengths to select best-fit aerosol models and to extrapolate aerosol single-scattering reflectance in VIS bands from NIR. In the single-scattering domain, the aerosol reflectance has linear relationship to the AOT. Moreover, the aerosol reflectance has linear inter-band relationship (i.e., linear SSE) for given aerosol model and sun-sensor geometries. Thus, the single-scattering concept provides aerosol reflectance model in analytic way.

The first official GOCI atmospheric correction implemented in the GDPS version 1.1 is theoretically based on the SeaWiFS atmospheric correction which relies on the SSE concept then partially modified. It especially focuses on the turbid water NIR correction to considering significant NIR water-leaving radiance in coastal region while the initial atmospheric correction is developed based on the BPA in NIR. The GOCI coverage contains highly turbid water areas such as the Yellow Sea, the East China Sea, and the coastal areas of the Korean peninsula. Then, the BPA atmospheric correction over those regions will fail in retrieving the water-leaving radiance due to its erroneous overestimation of aerosol radiance.

This first atmospheric correction method for GOCI has not considered effects of sun-glint effect and directionality due to their relatively less contributions to R_{rs} extraction.

2.2. Method

An atmospheric correction algorithm aims to retrieve the water reflectance (ρ_w) or remote-sensing reflectance (R_{rs}) from the total radiance recorded by a satellite ocean color sensor at the top-of-the-atmosphere (TOA) by removing atmospheric path radiance. Contributors of atmospheric path radiance at TOA level can be separately considered that are multiple scattering by air molecules (Rayleigh scattering) in the absence of aerosols (Fig. 7 (a)), multiple scattering by aerosols in the absence of air molecules (Fig. 7 (b)), and interactions between aerosols and molecules (Fig. 7 (c)) with considering not only radiances between sea surface and satellite but also Fresnel-reflected atmospheric radiances at the air-sea interface. An atmospheric correction algorithm aims to retrieve the water-leaving reflectance or remote-sensing reflectance (Fig. 7 (d)) from the total radiance recorded by a satellite ocean color sensor by removing atmospheric path radiance.

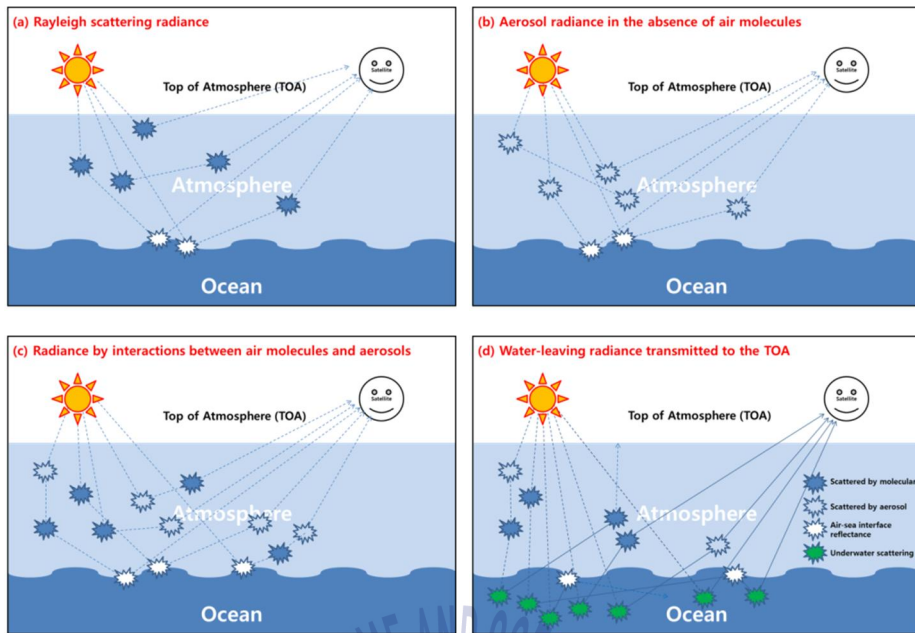


Fig. 7. Contributors of the TOA radiance. (a) Multiply scattered radiance by air molecules (Rayleigh scattering), (b) multiply scattered radiance by aerosols, (c) radiance by interactions between air molecules and aerosols, (d) water-leaving radiance that has to be retrieved eventually.

In addition to above, the process also corrects gaseous absorption, whitecap radiance, the bidirectional effect by the anisotropic angular distribution of water-leaving radiances, and water-leaving radiance at NIR wavelengths for turbid waters that initially assumed to be zero as shown in Fig. 8.

In this section, the current status of the GOCI standard atmospheric correction algorithm will be described which includes 1) gaseous absorption correction by ozone, 2) whitecap radiance correction by wind stress at the sea level, 3) solar irradiance normalization, 4) correction for molecular (Rayleigh) scattering with considering sea-surface roughness, 5) enhanced cloud mask over turbid waters, 6) correction scheme for aerosol radiance or reflectance based on SSE concept, 7) atmospheric transmittance estimation, and 8) near-infrared water-leaving reflectance correction over turbid waters using empirical

relationships of water-leaving reflectances between red and two NIR bands.

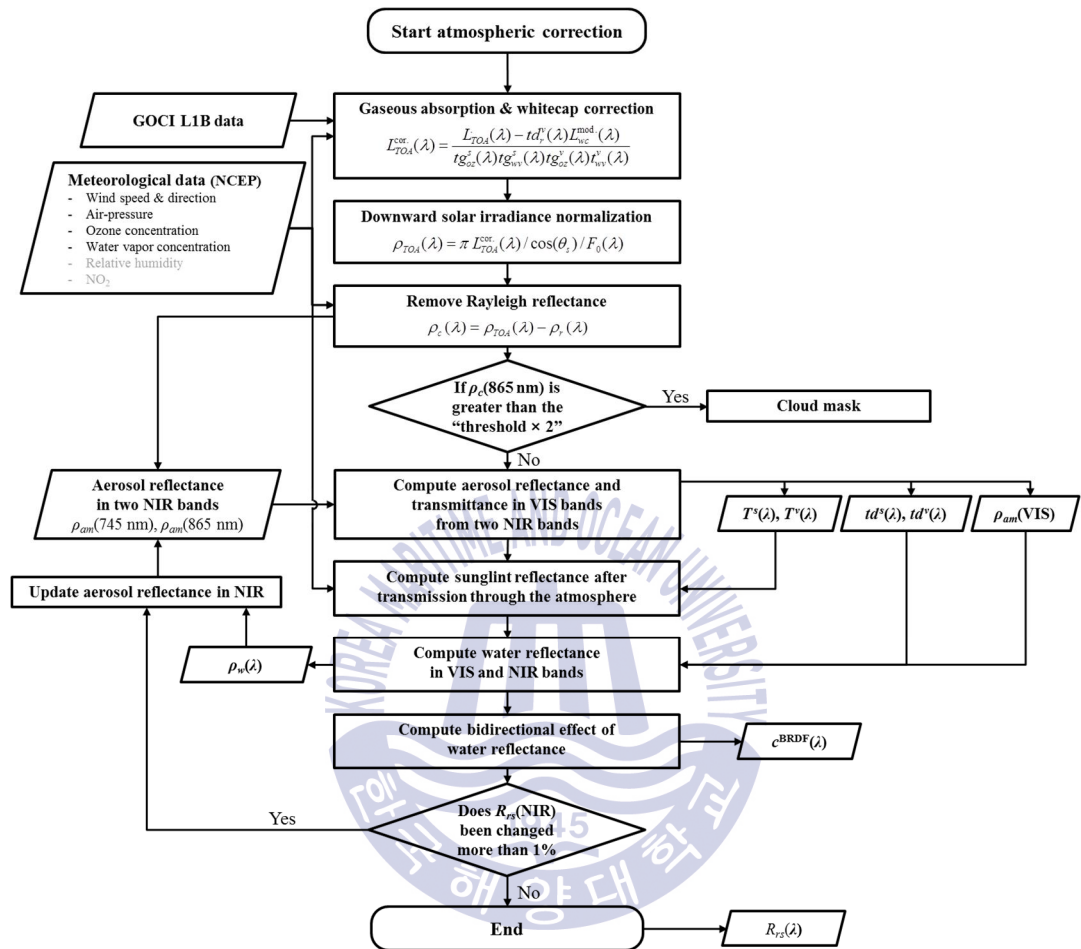


Fig. 8. Flow chart describing the overall atmospheric correction process.

2.2.1. Correction for gaseous absorption and white cap

Atmospheric correction algorithms generally start with correcting the gaseous absorption and white cap radiance emerged by wind stress at the sea level which can be predicted by meteorological information that are ozone, water vapor concentration, and wind speed as

$$L_{\text{TOA}}^{\text{cor.}}(\lambda) = \frac{L_{\text{TOA}}(\lambda) - td_r^v L_{\text{wc}}(\lambda)}{t_{\text{oz}}^s(\lambda)t_{\text{oz}}^v(\lambda)}, \quad (1)$$

where $L_{\text{TOA}}(\lambda)$ is the TOA radiance observed by satellite at a wavelength λ , $L_{\text{TOA}}^{\text{cor.}}$ is the TOA radiance after the correction of white cap and gaseous absorption, and td_r^v is the upward diffuse transmittance by air molecules from the sea surface to the sensor. Terms t_{oz}^s and t_{oz}^v are the downward gaseous transmittance by ozone from the sun to the sea surface and upward gaseous transmittance from the sea surface to the sensor, respectively. These ozone-absorptive transmittances t_{oz}^s and t_{oz}^v can be computed by quasi-analytic model as

$$t_{\text{oz}}^s(\lambda) = e^{\frac{-\tau_{\text{oz}}(\lambda)}{\cos(\theta_s)}}, \quad (2)$$

$$t_{\text{oz}}^v(\lambda) = e^{\frac{-\tau_{\text{oz}}(\lambda)}{\cos(\theta_v)}}, \quad (3)$$

where $\tau_{\text{oz}}(\lambda)$ is the optical thickness of ozone, θ_s is the solar zenith angle at the sea surface of the target point, and θ_v is the satellite zenith angle at the sea surface of the target point.

Whitecap reflectance can be simplified as a function of wind speed (Stramska and Petelski, 2003) and wavelength (Frouin et al., 1996). In this study, the effect of gas transfer efficiency by temperature is ignored due to its negligible contribution (Blanchard, 1971). The whitecap radiance L_{wc} can be expressed as

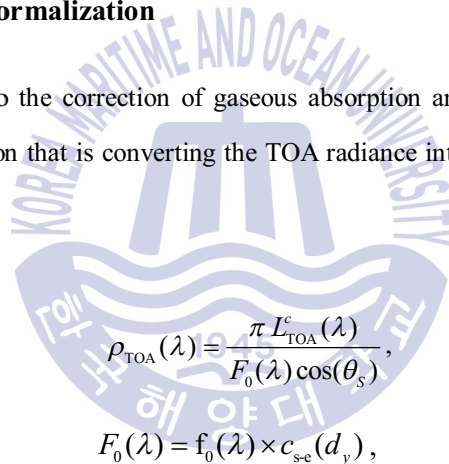
$$L_{\text{wc}}(\lambda) = F_0(\lambda) \times \cos \theta_s \times td_r^s(\lambda) \times \frac{c_{\text{wc}}(\lambda) \times 0.0000418 \times (w_s - 4.93)^3}{\pi}, \quad (4)$$

where F_0 is the extraterrestrial solar irradiance with considering sun-earth distance, td_r^s is the downward diffuse transmittance by air molecules, and c_{wc} is the spectral correction function (Frouin et al., 1996) for whitecap reflectance (i.e., 1.0, 1.0, 1.0, 1.0, 0.89, 0.89, 0.76, and 0.64 for

wavelength 412, 443, 490, 555, 660, 680, 745, and 865 nm, respectively), and w_s is the wind speed at the sea level in m/s. Recent atmospheric correction methods use the predefined look-up table (LUT) for the diffuse transmittance of the atmosphere with considering anisotropic oceanic radiances. Moreover, a precise atmospheric correction requires not only air molecules but also aerosols effect for diffuse transmittance. However, quasi-analytical model for Rayleigh diffuse transmittance is enough for the whitecap radiance estimation, because whitecap radiance has near isotropic angular distribution for water-leaving radiance field and residual whitecap radiance by omitted aerosol diffuse transmittance will be corrected as maritime aerosol radiance (Gordon and Wang, 1994)

2.2.2. Solar irradiance normalization

The next step subsequent to the correction of gaseous absorption and whitecap correction is the solar irradiance normalization that is converting the TOA radiance into the TOA reflectance (ρ_{TOA}) as



$$\rho_{\text{TOA}}(\lambda) = \frac{\pi L_{\text{TOA}}^c(\lambda)}{F_0(\lambda) \cos(\theta_s)}, \quad (5)$$

$$F_0(\lambda) = f_0(\lambda) \times c_{s-e}(d_y), \quad (6)$$

where θ_s is the solar zenith angle. The term f_0 is the extraterrestrial solar irradiance without considering sun-earth distance. Terms c_{s-e} and d_y are the sun-earth distance coefficient and day of year.

A full scene of GOCI is consisted by 16 sub-images (and is called as slots) that is obtained by step and stare method. Each slot is consisted by 8 band subsequently and band sequence is 660 nm (B5)→ 555 nm (B4)→ 745 nm (B7)→ 443 nm (B2)→ 680 nm (B6)→ 412 nm (B1)→ 865 nm (B8)→ 490 nm (B3) (Fig. 13). Therefore, each band and each slot are obtained in different time,

thus the time differences by introducing solar angles changes while compute the geometries should be considered.

After converting to the reflectance, the TOA reflectance can be divided by following contributions as

$$\rho_{\text{TOA}}(\lambda) = \rho_r(\lambda) + \rho_a(\lambda) + \rho_{ra}(\lambda) + tg^s(\lambda)tg^v(\lambda)\rho_g + td^s(\lambda)td^v(\lambda)\rho_{wn}(\lambda) \quad (7)$$

where ρ_r is the multiple scattering by air molecules (Rayleigh scattering) in the absence of aerosols, ρ_a is the multiple scattering by aerosols in the absence of air molecules, ρ_{ra} is the light interaction between air molecules and aerosols. Terms tg^s and tg^v are the total upward and downward direct transmittances including both the aerosols and the air molecules. Terms td^s and td^v are the total upward and downward diffuse transmittances including both the aerosols and the air molecules. The term ρ_{wn} is the water reflectance at sea surface in the absence of atmosphere. The term ρ_g is the sun-glint reflectance that is spectrally independent. However, the sun-glint has been omitted due to its relatively small contribution in GOCI sun-sensor geometries.

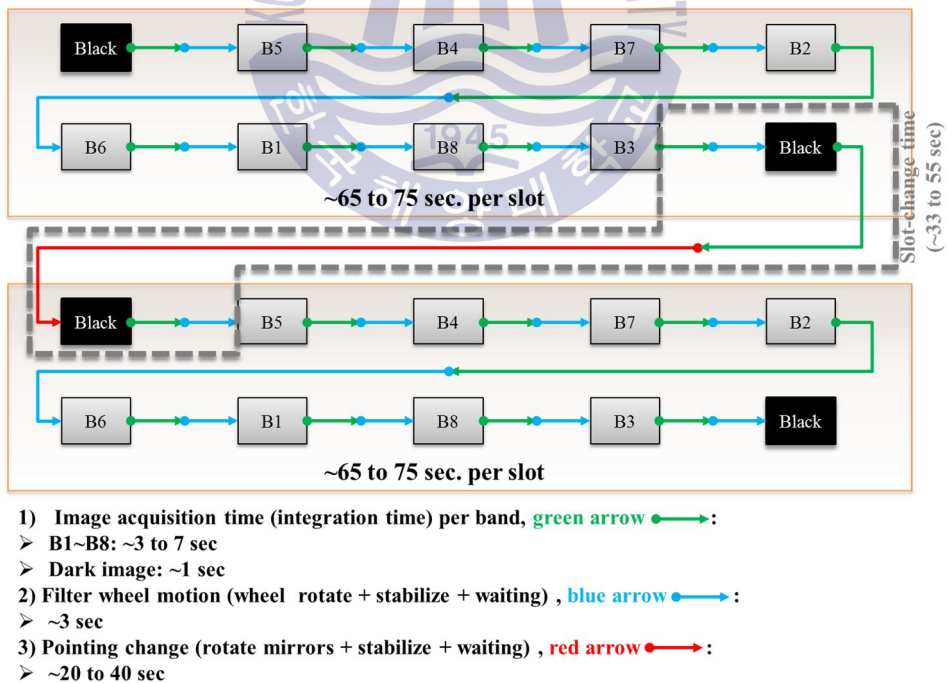


Fig. 9. Temporal sequence of each band and slot acquisition.

2.2.3. Correction for molecular (Rayleigh) scattering

Rayleigh scattering (ρ_r) takes the major quantitative part of the atmospheric reflectance (Wang, 2016). It can be horizontally fluctuated within a few percent by the air pressure changing, different geometries, and wind field distribution at the sea surface level. By the radiative transfer simulation, the Rayleigh component can be predicted less than one percent of error (Gordon et al., 1988; Gordon and Wang, 1992; Wang, 2002, 2016).

It is computationally intensive to directly calculate each pixel's Rayleigh reflectance. Thus, interpolated data from a pre-computed values from radiative transfer simulation is generally employed (Wang, 2003) for the Rayleigh correction. Four-dimensional lookup table is established for the most dominant parameters that are solar zenith angle, sensor zenith angle, relative azimuth angle, and wind. 6SV version 1 radiative transfer code and US Standard 62 atmospheric composition and profile model (McClatchey et al., 1971) are used for the simulation.

Subsequently, following model for the correction of air-pressure effect (Wang, 2005) is used as,

$$\rho_r(\lambda, c_p) = \rho_r^{1\text{atm}}(\lambda) \times \frac{1.0 - e^{-\text{coef}_r(\lambda) \times \tau_r^{\text{corr}}(\lambda, c_p) \times m^{\text{air}}}}{1.0 - e^{-\text{coef}_r(\lambda) \times \tau_r(\lambda) \times m^{\text{air}}}}, \quad (8)$$

where

$$\text{coef}_r(\lambda) = -\{0.6543 - 1.608 \times \tau_r(\lambda)\} + \{0.8192 - 1.2541 \times \tau_r(\lambda)\} \times \log(m^{\text{air}}), \quad (9)$$

$$\tau_r^{\text{corr}}(\lambda, c_p) = \left(\tau_r(\lambda) \times \frac{c_p}{1013.25} \right), \quad (10)$$

$$m^{\text{air}}(\theta_s, \theta_v) = \frac{1.0}{\cos \theta_s} + \frac{1.0}{\cos \theta_v}, \quad (11)$$

where $\rho_r^{1\text{atm}}$ and τ_r are the preliminary computed Rayleigh scattering reflectance and optical thickness (Bodhaine et al., 1999) for 1 atmospheric pressure (i.e., 1013.25 mb). The term

c_p is the air pressure in mb.

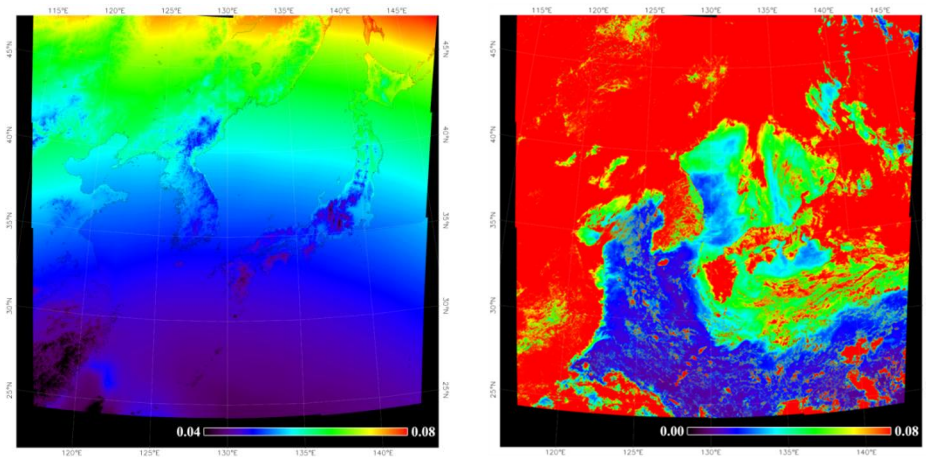


Fig. 10. An example of Rayleigh reflectance correction (2013/08/13, 03:16 UTC). (Left) Rayleigh reflectance at 555 nm. (Right) Rayleigh corrected reflectance ($\rho_{TOA} - \rho_r$) at 555 nm.

Figure 10 is an example result of Rayleigh reflectance correction used for the GOCI standard atmospheric correction in 2013/08/ 13 03:16 UTC.

2.2.4. Cloud mask

Earlier studies, the cloud mask had accounted for only the high aerosol optical thickness (AOT) or clouds. In this cases, the simplest way of detecting clouds or high AOT is the use of a $\rho_{TOA}(NIR) - \rho_r(NIR)$ threshold, with the underlying assumption that relatively high absorbance of water at NIR wavelengths. However, since the ocean color remote sensing had been considered in turbid coastal waters, those masks over turbid waters should also be considered (Wang and Shi, 2006). For highly turbid waters, the ocean has a considerable reflectance by the backscattering of suspended sediment. Thus use a threshold of a band's reflectance over turbid waters can be failed. To separate turbid water and a high AOT, it is needed to use multiple bands. In this study, the scheme used two NIR bands' (745 nm and 865 nm) slope and threshold of $\rho_{TOA}(NIR) - \rho_r(NIR)$ value of the GOCI based on the theory of water's absorption always make two NIR wavelengths' slope higher than the aerosol's slope, and these threshold values were decided by a simple test based method. It can be

approximated that reflectance ratio of ocean's two NIR bands' is always same (Ruddick et al., 2006) and give constraint that aerosol's slope range is around 0.9 to 1.2 from the assumption of aerosol types are only the oceanic or maritime. Selected pixels by threshold are applied to around 3x3 pixels due to the removal of sparkles that coming from the cloud's movement during band change. The result of this masking method is shown in the Fig. 11.

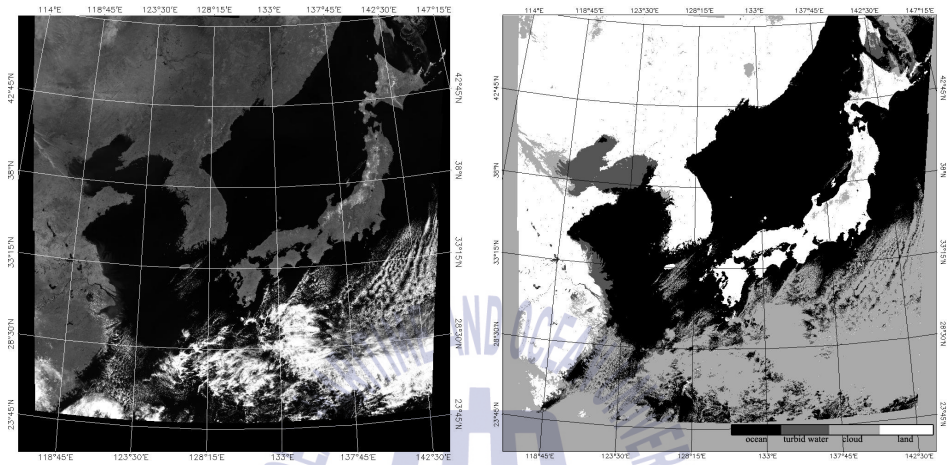


Fig. 11. An example result of cloud masking for both clear and turbid waters (2011/04/05 03:16 UTC). Left image is Rayleigh corrected reflectance at 865 nm and right image is result of cloud screening.

2.2.5. Aerosol multiple-scattering reflectance correction based on the SSE

The SSE aerosol correction scheme uses the aerosol multiple-scattering reflectances in presence of air molecules ($\rho_{ra} + \rho_a$, hereafter it will be denoted as ρ_{am}) in two NIR bands as $\rho_{am}(NIR_{S,L}) = \rho_{TOA}(NIR_{S,L}) - \rho_r(NIR_{S,L})$ using the BPA. The sensor-measured aerosol reflectance values in the two NIR bands $\rho_{am}(NIR)$ are used to select the two closest aerosol models and determine the corresponding weighting factor. In the process, the observed $\rho_{am}(NIR)$ values are first converted to the aerosol single-scattering reflectance $\rho_{as}(M_i, NIR)$ using the following fourth-order polynomial relationship which is empirical (Wang and Gordon, 1994; Gordon and Wang, 1994):

$$\rho_{as}(M_i, \lambda, \theta_s, \theta_v, \phi_{sv}) = \sum_{n=1}^4 a_n(M_i, \lambda, \theta_s, \theta_v, \phi_{sv}) \rho_{am}(\lambda)^n, \quad (12)$$

where a_n is the polynomial coefficient stored in the look-up tables for the i^{th} candidate aerosol model (M_i), solar zenith angle (θ_s), sensor zenith angle (θ_v), and relative azimuth angle (ϕ_{sv}). The $\rho_{as}(M_i, \text{NIR})$ values are used to calculate the epsilon value (ε) for selecting the aerosol models:

$$\varepsilon(M_i, \lambda_1, \lambda_2, \theta_s, \theta_v, \phi_{sv}) = \rho_{as}(M_i, \lambda_1, \theta_s, \theta_v, \phi_{sv}) / \rho_{as}(M_i, \lambda_2, \theta_s, \theta_v, \phi_{sv}). \quad (13)$$

Theoretically, each model M_i has its own AOT-independent SSE value (ε^{pre}) for a specific geometry. The scheme selects two appropriate aerosol models M_L and M_H by comparing each model's $\varepsilon^{pre}(M_i, \text{NIR}_S, \text{NIR}_L)$ with the average epsilon value (ε^{ave}) of the candidate aerosol models' $\varepsilon(M_i, \text{NIR}_S, \text{NIR}_L)$ with assuming that multiple-scattering effects for any given model are nearly same in NIR (Gordon and Wang, 1994), i.e.:

$$\varepsilon^{pre}(M_L, \text{NIR}_S, \text{NIR}_L) \leq \varepsilon^{ave}(\text{NIR}_S, \text{NIR}_L) < \varepsilon^{pre}(M_H, \text{NIR}_S, \text{NIR}_L), \quad (14-1)$$

$$\varepsilon^{ave}(\text{NIR}_S, \text{NIR}_L) = N^{-1} \sum_{i=1}^N \varepsilon(M_i, \text{NIR}_S, \text{NIR}_L). \quad (14-2)$$

Then, the weighting factor w^{M_i} of the two contributing aerosols (M_L and M_H) is estimated from the following two equations:

$$w^{M_L} = \frac{\varepsilon^{pre}(M_H, \text{NIR}_S, \text{NIR}_L) - \varepsilon^{ave}(\text{NIR}_S, \text{NIR}_L)}{\varepsilon^{pre}(M_H, \text{NIR}_S, \text{NIR}_L) - \varepsilon^{pre}(M_L, \text{NIR}_S, \text{NIR}_L)}, \quad \text{and} \quad (15-1)$$

$$w^{M_H} = 1 - w^{M_L}. \quad (15-2)$$

Having derived the values for M_L , M_H , w^{M_L} , and w^{M_H} , the aerosol multiple-scattering reflectances (ρ_{am}) in the VIS bands are estimated using the two selected aerosol models through the inversion of Eq. (12):

$$\rho_{am}(\lambda) = w^{M_L} \sum_{n=1}^4 b_n(M_L, \lambda, \theta_s, \theta_v, \phi_{sv}) \rho_{as}(M_L, \lambda)^n + w^{M_H} \sum_{n=1}^4 b_n(M_H, \lambda, \theta_s, \theta_v, \phi_{sv}) \rho_{as}(M_H, \lambda)^n, \quad (16)$$

where b_n is the polynomial coefficient for the respective M_i , θ_s , θ_v , and ϕ_{sv} .

Although directly applying the weighting factors in the multiple-scattering domain which is

computed in single-scattering space is not an exact solution, estimating the $\rho_{am}(\lambda)$ values in this way provides a reasonable approximation because the relationships between the single-scattering and multiple-scattering of aerosols are near linear. The $\rho_{am}(\lambda)$ values synthesized in this way are a reasonable approximation with an error of $\pm 0.002\%$ and explained some success with SeaWiFS (Gordon and Wang, 1994; Wang and Gordon, 1994).

Overall scheme of the SeaWiFS aerosol correction method is summarized in Fig. 12.

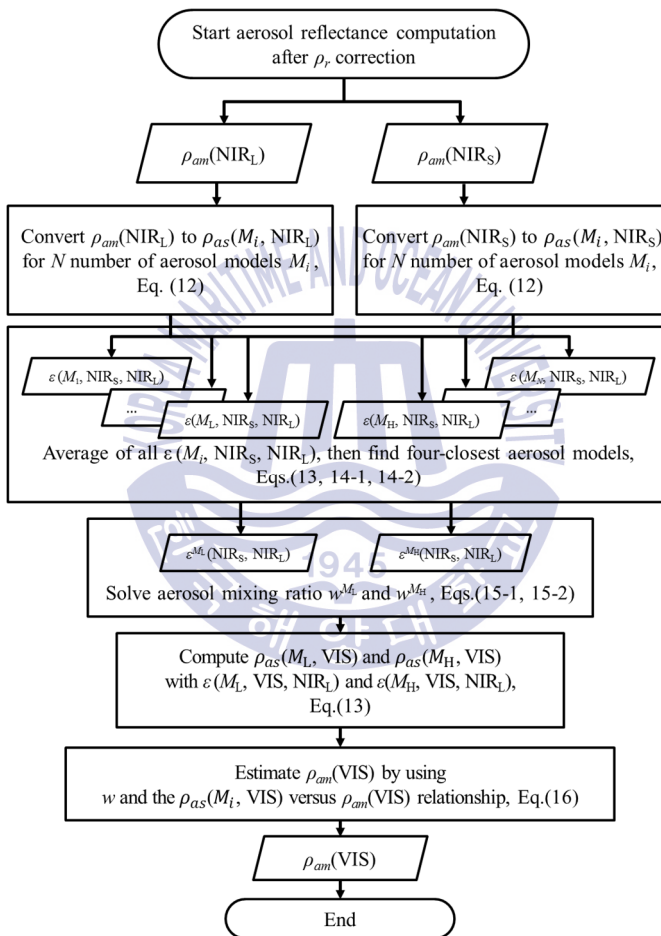


Fig. 12. Scheme of the $\rho_{am}(\text{VIS})$ estimation used by SeaWiFS and initial GOCI atmospheric correction (Gordon and Wang, 1994; Wang and Gordon, 1994; Ahn et al., 2012). The method uses the relationship between single-scattering and multiple-scattering aerosol reflectance to select optimum aerosol models.

2.2.6. Correction for atmospheric diffuse transmittance

The diffuse transmittances from the sun to the surface (td^s) and from the surface to the sensor td^v used for general ocean surface reflectance terms are consisted by air molecules term and aerosol term, i.e.,

$$td^s(\lambda) = td_r^s(\lambda) \times td_a^s(\lambda) \times td_{ra}^s(\lambda), \quad (17-1)$$

$$td^v(\lambda) = td_r^v(\lambda) \times td_a^v(\lambda) \times td_{ra}^v(\lambda), \quad (17-2)$$

where $td_r(\lambda)$ is diffuse transmittance air molecules (in the absence of aerosol) and $td_a(\lambda) \times td_a(\lambda)$ is diffuse transmittance of aerosols in the presence of air molecules.

These can be estimated by analytic models with single-scattering approximation (Gordon et al., 1983) as,

$$td_r^v(\lambda) = e^{\frac{-\tau_r(\lambda)}{2\cos(\theta_v)}}, \quad (18-1)$$

$$td_r^s(\lambda) = e^{\frac{-\tau_r(\lambda)}{2\cos(\theta_s)}}, \quad (18-2)$$

$$td_a^v(\lambda) \times td_a^v(\lambda) = e^{\left[\frac{-\{1-\omega_a(\lambda)\eta(\lambda)\} \times \tau_a(\lambda)}{\cos(\theta_v)} \right]}, \quad (19-1)$$

$$td_a^s(\lambda) \times td_a^s(\lambda) = e^{\left[\frac{-\{1-\omega_a(\lambda)\eta(\lambda)\} \times \tau_a(\lambda)}{\cos(\theta_s)} \right]}, \quad (19-2)$$

where term $\tau_a(\lambda)$ is optical thickness of aerosols and $\eta(\lambda)$ is forward scattering probability of aerosols.

2.2.7. Correction for near-infrared water reflectance over turbid waters

For the majority of the open ocean, the general atmospheric correction method (Wang and Gordon, 1994; Gordon and Wang, 1994; Fukushima et al., 1998; Antoine and Morel, 1999) estimates $\rho_a(\text{NIR}) + \rho_{ra}(\text{NIR})$ by the black pixel assumption (i.e., $\rho_w(\text{NIR}) = 0$). In more turbid coastal waters, the black pixel assumption (BPA) is invalidated by the enhanced contributions due to suspended particles in the water (Hu et al., 2000; Ruddick et al., 2000; Siegel et al., 2000; Stumpf et al., 2003; Wang and Shi, 2007; Wang et al, 2012; Ahn et al., 2012; Goyen et al., 2013a, 2013b). This demands

an exact separation between $\rho_w(\text{NIR})$ and $\rho_a(\text{NIR})+\rho_{rd}(\text{NIR})$ in the process of atmospheric correction. As shown in Fig. 11, the GOCI standard atmospheric correction algorithm iteratively subtracts water reflectance $\rho_w(\text{NIR})$ estimated by the model from the $\rho_{\text{TOA}}(\text{NIR})-\rho_r(\text{NIR})$. To estimate $\rho_w(\text{NIR})$, Ahn et al. (2012) suggested an empirical relationship of water reflectance between the red and two NIR bands (Eq. 33 and Eq. 34) (Ruddick et al., 2006),

$$\rho_{wn}(745 \text{ nm}) = \sum_{n=1}^4 j_n \rho_{wn}(660 \text{ nm})^n, \quad (20)$$

$$\rho_{wn}(865 \text{ nm}) = \rho_{wn}(745 \text{ nm}) / 1.936. \quad (21)$$

The relationship between $\rho_{wn}(745 \text{ nm})$ and $\rho_{wn}(680 \text{ nm})$ instead of $\rho_{wn}(660 \text{ nm})$ can also be used. However, $\rho_{wn}(680 \text{ nm})$ is not considered in this study, since the effect of GOCI's inter-slot-radiometric-discrepancy (ISRDR) is more prominent at 680 nm than at 660 nm (Kim et al., 2015).

Fig. 13 is summarizing the iterative scheme for turbid water NIR correction as a flow chart.

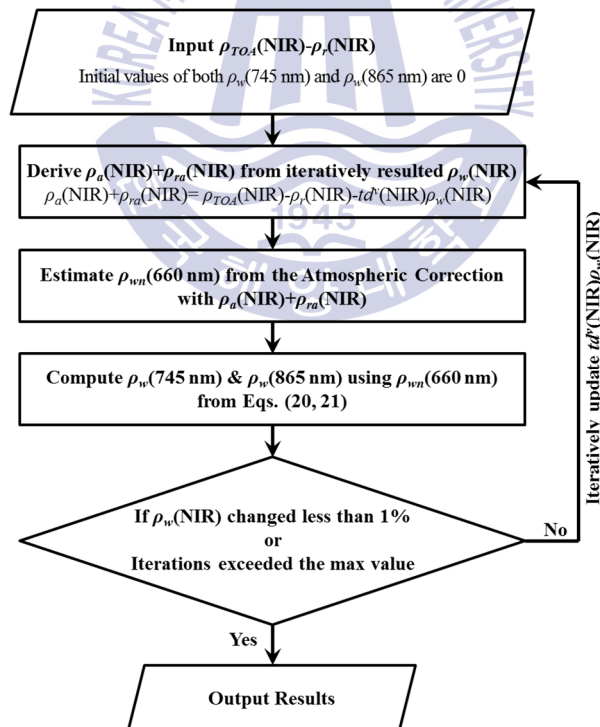


Fig. 13. Flow chart of the turbid water $\rho_{wn}(\text{NIR})$ correction scheme for the GOCI standard atmospheric correction (Ahn et al., 2012, 2015).

2.3. Conclusion

This chapter has described the initial GOCI standard atmospheric correction schemes implemented in GDPS version 1.1 (Ahn et al., 2012) in detail. This GOCI atmospheric correction algorithm was developed based on the SeaWiFS algorithms because the SeaWiFS algorithm has used most widely and SeaWiFS bands' characteristics are similar to GOCI sensor. The turbid water NIR correction model for GOCI algorithm uses spectral relationship of water reflectance between red band and two NIR bands (Ahn et al., 2012) while the SeaWiFS algorithm uses biogenic ocean color model (Bailey et al., 2010). This first GOCI atmospheric correction has omitted the bidirectional effect correction and sun-glint effect correction due to their relatively small contributions to the atmospheric correction system. Differences of two algorithms are summarized in Table 4.

Table 4. Comparison of the SeaWiFS atmospheric correction algorithm with the GOCI algorithm

	SeaWiFS algorithm (NASA standard)	GOCI algorithm (GDPS ver. 1.1)
Aerosol correction method	Using SSE (Gordon and Wang, 1994; Wang and Gordon, 1994)	Using SSE (Gordon and Wang, 1994; Wang and Gordon, 1994)
Turbid water NIR correction	Biogenic ocean color model (Bailey et al., 2010)	4 th order spectral relationship of water reflectance between 660 and 745 nm, and linear relationship between 745 and 865 nm (Ahn et al., 2012)
Sun-glint correction	Wind field dependent correction model (Cox and Munk, 1954)	Omitted
Atmospheric transmittance	Radiative-transfer-simulation-based model with considering anisotropic water reflectance angular distribution (Yang and Gordon, 1997; Wang, 1999)	Analytic model without considering anisotropic water reflectance angular distribution (Gordon et al, 1983)
Bidirectional effect correction	In-water bidirectional effect correction model (Morel et al., 2002), and air-sea interface bidirectional effect correction model (Franz et al., 2003)	Omitted

Chapter 3. Algorithm updates and vicarious calibration for the GOCI atmospheric correction

3.1. Backgrounds

The first GOCI atmospheric correction algorithm introduced in Chapter 2 has been developed theoretically based on the SeaWiFS atmospheric correction approach (Gordon and Wang, 1994) because the SeaWiFS algorithm has been most widely used in ocean color community with efforts for verifications, and GOCI has a similar spectral band design with SeaWiFS. Compared to SeaWiFS algorithm, This GOCI algorithm includes different NIR correction model for turbid water using spectral reflectance relationship between red and two NIR bands. In the process, the modeled NIR water reflectance is iteratively updated by red band water reflectance resulted by the atmospheric correction (Ahn et al., 2012). This GOCI algorithm has been modified through the GDPS update since version 1.1.

This chapter describes updated-items of the GOCI atmospheric algorithm developed by this thesis. The updates includes the water-vapor gaseous absorption, sun-glint correction, Rayleigh reflectance correction, aerosol reflectance correction, bidirectional effect of water reflectance correction, atmospheric transmittance correction with considering anisotropic angular distribution of water reflectance, and adjustment of turbid water NIR correction model. Additionally, vicarious calibration is applied to enhance agreement between GOCI atmospheric correction system and the observation.

The updates especially focuses on the alternative correction method for multiple-scattering aerosol reflectance (Ahn et al., 2016) to avoid uncertainties from multiple-scattering to single-scattering conversion and determining the appropriate aerosol model and their contribution quantities in the Gordon and Wang (1994) process.

Validations for the first GOCI atmospheric correction algorithm has shown encouraged result for turbid waters, however validations for relatively clear water has shown considerable errors due to a

lack of vicarious calibration (Ahn et al., 2012; Moon et al., 2012). In the thesis, the vicarious calibration approach based Franz et al. (2007) is applied to the GOCI atmospheric correction system following the atmospheric correction algorithm updates.

3.2. Updates to the initial GOCI atmospheric correction algorithm

3.2.1. Correction for the water vapor absorption

Meanwhile, the effect of water vapor absorption for correction of gaseous absorption in the GOCI algorithm has been ignored, because GOCI bands are designed to avoid the absorption spectra. Recently revised investigation has showed that water vapor absorption effect on GOCI bands 660, 745, and 865 nm for large zenith angles can be significant (Fig. 15) due to the absorption spectrum crossing in the out of band response range (Fig. 14).

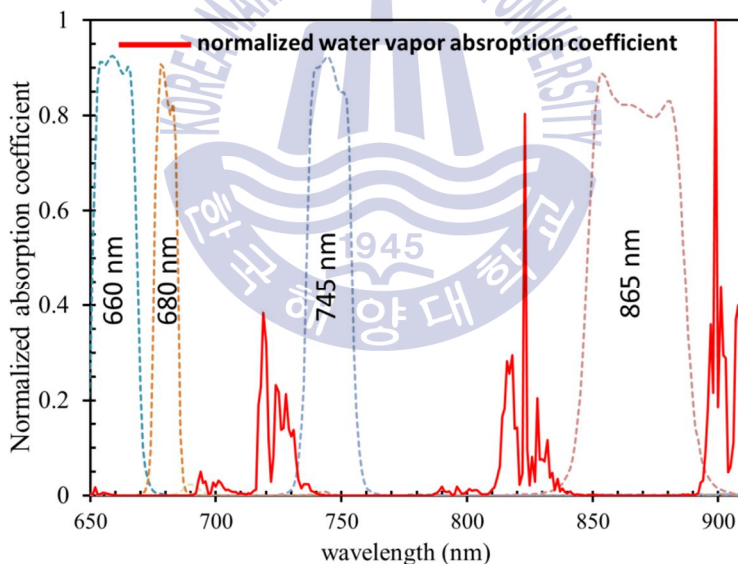


Fig. 14. Water vapor and oxygen absorption spectra in red and NIR bands. Both the oxygen and water vapor absorption spectrum are overlapped in the range of out-of-band responses.

For the correction, 2nd order polynomial relationship between $\ln\{-\ln(wv)\}$ and $\ln\{(1/\cos \theta_s + 1/\cos \theta_v) \times wv\}$ is used contrariwise method for SeaWiFS, MODIS, and VIIRS uses linear relationship

(Vermeulen, SeaWiFS Data Analysis System source code), then a simple estimating model for water vapor absorption (i.e., $t_{wv} = t_{wv}^s \times t_{wv}^v$) at the TOA level is developed using the radiative transfer simulation (Fig. 16) as

$$t_{wv}(\lambda) = t_{wv}^s(\lambda) t_{wv}^v(\lambda) = \exp \left[-\exp \left\{ a_n \sum_{n=0}^2 \ln \left(\frac{wv}{\cos \theta_s} + \frac{wv}{\cos \theta_v} \right)^n \right\} \right], \quad (22)$$

where wv is the water vapor concentration in g/cm^2 . Terms a_n are the coefficients for the correction model and is tabulated in the Table 5, and verification of the correction model is represented in Fig.17. For the simulation, the Second Simulation of a Satellite Signal in the Solar Spectrum, Vector (6SV), version 1 (Vermeulen et al., 2006) was used with assuming that the water vapor vertical profile is following the US standard 62 model (McClatchey et al., 1971).

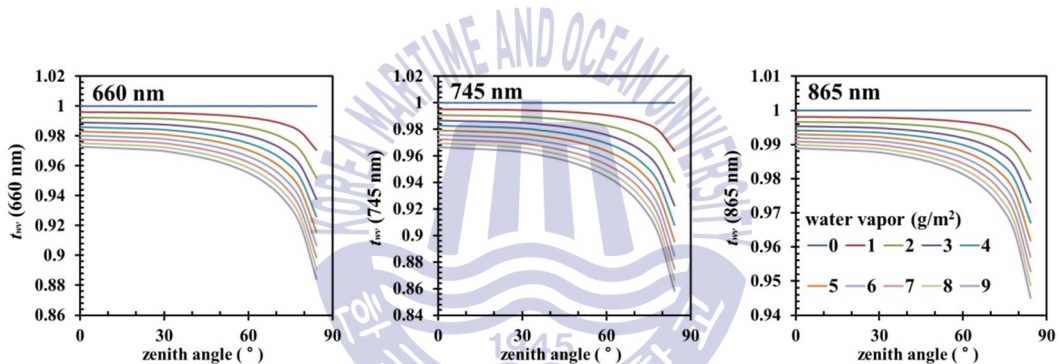


Fig. 15. Radiative transfer simulation (6SV version 2.1) results for the gaseous transmittance of water vapor absorption at 660, 745, and 865 nm with water vapor concentration ranging from 0 to 9 g/cm^2 and solar or sensor zenith angle ranging from 0 to 85° .

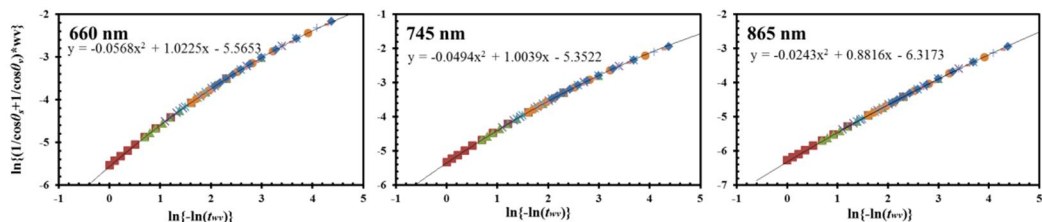


Fig. 16. The 2nd order polynomial relationships between $\ln\{-\ln(wv)\}$ and $\ln\{(1/\cos\theta_s+1/\cos\theta_v)\times wv\}$ for 660, 745, and 865 nm.

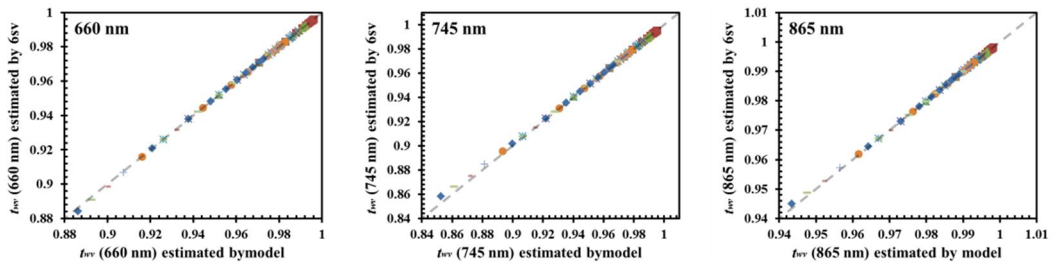


Fig. 17. Verification results of the established water vapor correction model with simulations.

Table 5. Derived coefficients for the water vapor absorption model.

	a_0	a_1	a_2
660 nm	-5.5653	1.0225	-0.0568
745 nm	-5.3522	1.0039	-0.0494
865 nm	-6.3173	0.8816	-0.0243

3.2.2 Sun-glint correction

Sun-glint is the specular reflectance of sunlight at the roughened sea surface. The effect has been omitted for the GOCI atmospheric correction initially because the sun-glint effect is relatively small for GOCI sun-sensor geometries. Nevertheless sun-glint effect in GOCI data is less than other polar orbit sensors, a small direct reflectance of sunlight by ocean surface can cause a considerable error in the southern part of GOCI imagery during summer season because the sun light itself is still relatively massive. Generally, the model of Cox & Munk (1954) is used to remove the sun-glint effect ρ_g , and denoted as equation (23) where ω is the specular reflection angle, θ_n is reflected direction and $p(z_x, z_y)$ is the probability distribution of facet slopes that depends on the wind speed and direction.

$$\rho_g = \frac{\pi f(\omega, \lambda) p(z_x, z_y)}{4 \cos \theta_v \cos \theta_s \cos^4 \theta_n}, \quad (23)$$

where $\cos 2\omega = \cos \theta_v \cos \theta_s + \sin \theta_v \sin \theta_s \cos(\phi_v - \phi_s)$,

$$\cos \theta_n = \frac{\cos \theta_v + \cos \theta_s}{2 \cos \omega}. \quad (24)$$

Fig. 18 is an example image of sun-glint reflectance for an GOCI scene in 2013/08/13 03:16 UTC.

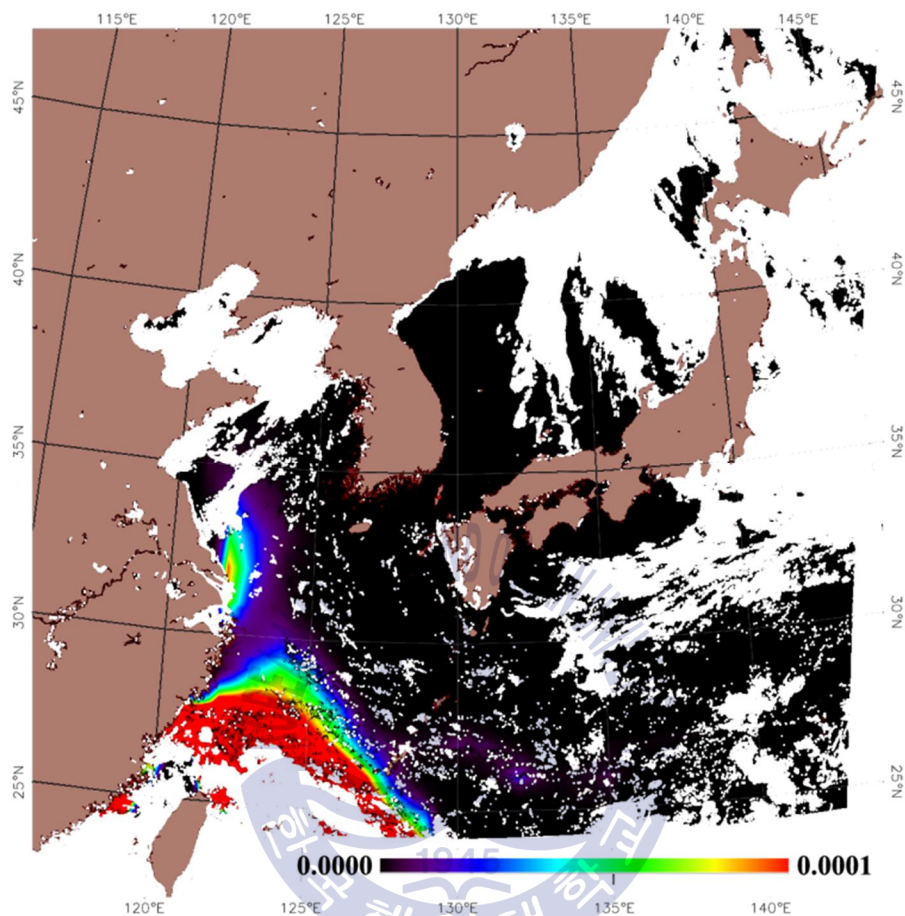


Fig. 18. An example of sun-glint reflectance (2013/08/13 03:16 UTC) estimated by Cox & Munk (1954).

3.2.3. Considering gravity effect for the Rayleigh scattering

The reflectance from the air-molecules (Rayleigh scattering reflectance) takes the largest part of atmospheric reflectance. It contributes about 70~90% of TOA reflectance in blue bands. Therefore, the atmospheric correction accuracy performance is sensitive to the Rayleigh scattering reflectance computation. A recent study has shown that the Rayleigh reflectance can be changed by gravity for the same air-pressure because Rayleigh optical thickness is in inverse proportion to gravity controlled by latitude and altitude changes (Bodhaine et al., 1999). The gravity (G) has maximum

value in pole, and minimum value in equator due to the rotation of earth and the sea surface gravity can be expressed as (Fig.19),

$$G = 980.616 \times \{1 - 0.0026373 \cos(2L) + 0.0000059 \cos^2(2L)\} \quad (25)$$

where L is the latitude in radian.

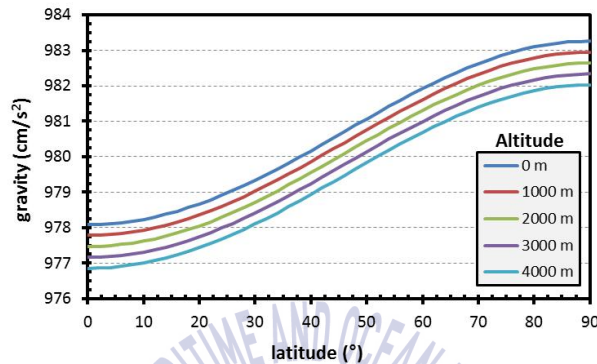


Fig. 19. Earth gravity for various latitudes and altitudes (Bodhain et al., 1999). The gravity at the surface (0 m altitude) is varied ~0.53% with depending on the latitude.

After applying the gravity correction of Rayleigh optical thickness into equation (10), sensitivity test for the R_{rs} retrieval can be changed up to ~3% for GOCI observation area and up to ~5% for polar orbit sensors.

3.2.4. Correction for the multiple scattering by aerosols - SRAMS

The SSE aerosol correction scheme (Gordon and Wang, 1994; Wang and Gordon, 1994) has been widely adopted for not only the GOCI and SeaWiFS but also the Moderate Resolution Imaging Spectroradiometer (MODIS), the Visible Infrared Imaging Radiometer Suite (VIIRS), and the Global Imager (GLI) (Toratani et al., 2007). However, the aerosol correction approach based on the SSE has several issues regarding the determination of appropriate aerosol models and their fraction (Ahn et al., 2016; Ahmad and Franz, 2016). In the process, the two most appropriate aerosol models and their mixture ratio (*i.e.*, weighting factor) are determined by comparison of the average SSE in NIR for all candidate aerosol models with assuming that multiple- to single-scattering conversion is

not sensitive to aerosol models in NIR. It implies that all candidate models contribute to the model selection process although some of them are not really part of any cause. And the linear weighting factor computed in the single-scattering domain is directly used in the multiple-scattering domain to be used for extrapolation to the visible bands. Therefore, the estimated aerosol reflectances of the two models do not add up to the observed aerosol reflectance in NIR, and it may cause some residual errors. These irrelevant models can erroneously effect the mixture ratio of two appropriate models with inducing residual errors that will be amplified during the aerosol reflectance extrapolation from NIR to VIS wavelengths.

This section describes an alternative aerosol correction scheme for GOCI atmospheric correction that estimates reflectance fraction of the two models in the multiple-scattering domain directly, without going through the single-scattering domain to select appropriate aerosol models and the spectral extrapolation of their reflectances from NIR to VIS bands. Spectral relationships of aerosol multiple-scattering reflectance (and is named SRAMS) between several wavelengths can be established with polynomial functions while aerosol optical thickness (τ_a) changes for i^{th} candidate aerosol model (M_i), θ_s , θ_v , and ϕ_{sv} (maritime example for GOCI 8 bands is shown in Fig. 20) (Ahn et al., 2016) as

$$\rho_{am}^{\text{Mod}}(M_i, \lambda_2) = \sum_{n=1}^D c_n (M_i, \lambda_1, \lambda_2, \theta_s, \theta_v, \phi_{sv}) \rho_{am}(\lambda_1)^n, \quad (26)$$

where D is the degree of the polynomial, $\rho_{am}^{\text{Mod}}(M_i, \lambda)$ is the theoretically computed $\rho_{am}(\lambda)$ for the considered model M_i , geometries and band pairs. The term c_n represents the constants of the polynomial equation stored in the look-up table (LUT) for each model M_i , θ_s , θ_v , and ϕ_{sv} . For all cases, the mean correlation coefficient is close to unity, and the mean absolute error in $\rho_{am}(412 \text{ nm})$ is <0.0002 for general solar-sensor geometries ($1/\cos \theta_s + 1/\cos \theta_v < 5.0$). The established polynomial relationships corresponding to various GOCI spectral responses (412, 443, 490, 555, 660, 680, 745, and 865 nm) are listed in Table 6. For the correlation test, simulations were carried out for τ_a from 0.05–0.45 in steps of 0.05 at 865 nm, θ_s from 0–75° in steps of 25°, θ_v from 0–60° in steps of 20°, and ϕ_{sv} from 0–180° in steps of 15° using Shettle and Fenn (1979) aerosol models the oceanic model with relative humidity (RH) 99% (this model has the smallest spectral slope

compared with the other candidate aerosol models), the maritime model with RH 50, and the tropospheric model with RH 50 (this model has the greatest spectral slope compared with the other candidate aerosol models) that will be used for parts of candidate aerosol models in aerosol selection process.

Table 6. Summary of the spectral relationships for various GOCI bands.

λ_1 (nm)	865	745	745	745	555	555	555
λ_2 (nm)	745	680	660	555	490	430	412
D	2	3	3	4	4	4	4
Min. R^2	0.9998	1.0000	1.0000	1.0000	0.9999	1.0000	1.0000

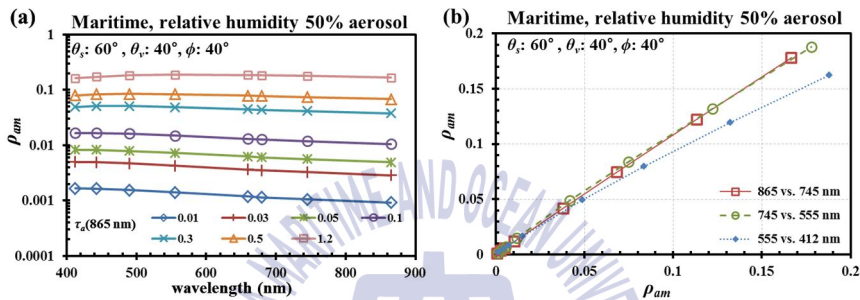


Fig. 20 (a) Spectral dependence of ρ_{am} for a range of aerosol optical depth τ_a (865) from 0.01 to 1.2 for the maritime aerosol model with RH = 50% and solar-sensor geometries $\theta_s=60^\circ, \theta_v=40^\circ, \phi_{sv}=40^\circ$. (b) Spectral relationships between aerosol multiple-scattering reflectances at several wavelengths for the same aerosol model and solar-sensor geometries.

To estimates $\rho_{am}(\text{VIS})$ with using the SRAMS explained above, the process first computes the $\rho_{am}^{M_i}(\text{NIR}_S)$ (Eq.26) for all aerosol models, then find two closest models M_L and M_H by comparison of the $\rho_{am}(\text{NIR}_S)$ from observation to $\rho_{am}^{\text{Mod}}(M_i, \text{NIR}_S)$ from candidates as

$$\rho_{am}^{\text{Mod}}(M_L, \text{NIR}_S) \leq \rho_{am}(\text{NIR}_S) < \rho_{am}^{\text{Mod}}(M_H, \text{NIR}_S). \quad (27)$$

Therefore, two aerosol models, M_L and M_H , contribute to $\rho_{am}(\text{NIR}_S)$:

$$\rho_{am}(\text{NIR}_S) = \sum_{n=1}^2 c_n(M_H, \lambda, \theta_s, \theta_v, \phi_{sv}) \left[w^{M_H} \rho_{am}(\text{NIR}_L) \right]^n + \sum_{n=1}^2 c_n(M_L, \lambda, \theta_s, \theta_v, \phi_{sv}) \left[w^{M_L} \rho_{am}(\text{NIR}_L) \right]^n. \quad (28)$$

Then the weighting factor w^{M_H} can be computed by solving the following quadratic formula,

$$A(w^{M_H})^2 + B(w^{M_H}) + C = 0, \quad (29-1)$$

where

$$A = \rho_{am}(\text{NIR}_L)^2 \left\{ \begin{array}{l} c_2(M_L, \lambda, \theta_s, \theta_v, \phi_{sv}) \\ +c_2(M_H, \lambda, \theta_s, \theta_v, \phi_{sv}) \end{array} \right\},$$

$$B = \rho_{am}(\text{NIR}_L) \left\{ \begin{array}{l} c_1(M_H, \lambda, \theta_s, \theta_v, \phi_{sv}) \\ -c_1(M_L, \lambda, \theta_s, \theta_v, \phi_{sv}) \\ -2c_2(M_L, \lambda, \theta_s, \theta_v, \phi_{sv})\rho_{am}(\text{NIR}_L) \end{array} \right\}, \quad (29-2)$$

$$C = \rho_{am}(\text{NIR}_L) \left\{ \begin{array}{l} c_1(M_L, \lambda, \theta_s, \theta_v, \phi_{sv}) \\ +c_2(M_L, \lambda, \theta_s, \theta_v, \phi_{sv})\rho_{am}(\text{NIR}_L) \end{array} \right\} - \rho_{am}(\text{NIR}_S).$$

Using the above equations, the SRAMS method solves the reflectance fraction (w) for the combination of $\rho_{am}(\text{NIR}_L)$ (i.e., $\rho_{am}(\text{NIR}_L) = w^{ML} \rho_{am}^{\text{Mod}}(M_L, \text{NIR}_L) + w^{MH} \rho_{am}^{\text{Mod}}(M_H, \text{NIR}_L)$, Eq. (28)) and therefore does not produce any residual errors.

Hence, it can be extrapolated $\rho_{am}(\text{VIS})$ with the known aerosol models (M_L and M_H) and their reflectance fractions (w^{ML} and w^{MH}) as following

$$\rho_{am}(\lambda_2) = \sum_{n=1}^D c_n(M_H, \lambda, \theta_s, \theta_v, \phi_{sv}) \left[w^{M_H} \rho_{am}^{\text{Mod}}(M_H, \lambda_1) \right]^n + \sum_{n=1}^D c_n(M_L, \lambda, \theta_s, \theta_v, \phi_{sv}) \left[(1 - w^{M_H}) \rho_{am}^{\text{Mod}}(M_L, \lambda_1) \right]^n. \quad (30)$$

Finally, the desired $\rho_w(\lambda)$ can be derived with known quantities $\rho_r(\lambda)$ and $\rho_{am}(\lambda)$, and $td^v(\theta_v, \lambda)$.

For this study, following nine aerosol models based on the Shettle and Fenn (1979) is used as candidates, an oceanic model with relative humidity (RH) 99% (O99), maritime models with RH 50, 70, 90, and 95% (M50, M70, M90, and M95), coastal models with RH 50 and 70% (C50 and C70),

tropospheric models with RH 50 and 80% (T50 and T80). From above models, O99 has the lowest spectral slope due to the largest particle size (a mixture of accumulate-mode mean radius 0.995 μm and coarse-mode mean radius 8.59 μm), and T50 has the highest spectral slope due to smallest particle size (mean radius 0.0275 μm).

The overall process for the $\rho_{am}(\text{VIS})$ estimation using the SRAMS is summarized as a flow chart in Fig. 21.

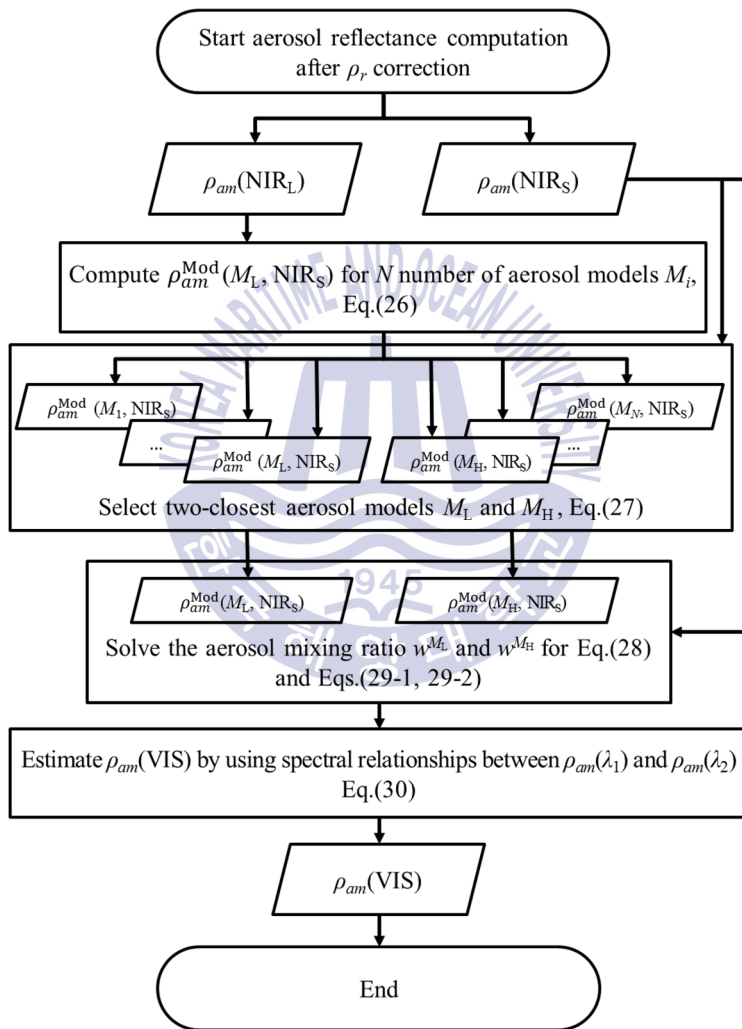


Fig. 21. Flow chart describing the process of SRAMS approach for estimating $\rho_{am}(\text{VIS})$ from $\rho_{am}(\text{NIR})$

3.2.5. Correction for bidirectional effects of water reflectance

Angular dependence of R_{rs} or nL_w is initially ignored for GOCI atmospheric correction because the bidirectional effect is normally less contributed compared with other atmospheric correction schemes (Ahn et al., 2012). When zenith angles become large (i.e., high airmass), however, this bidirectional effect (c_{BF}) can be significant, thus the R_{rs} varies more than $\pm 10\%$ as figure 22.

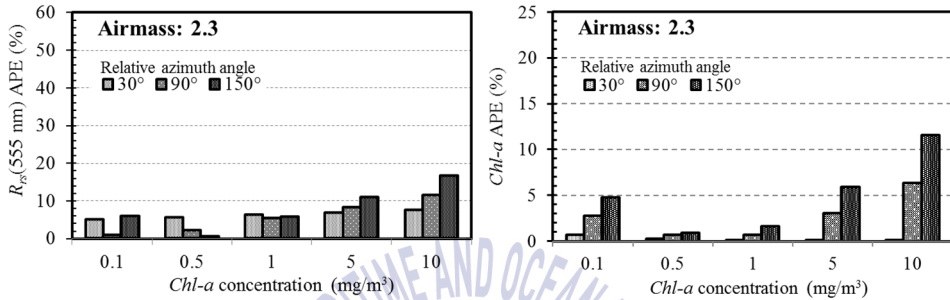


Fig. 22. Impacts of bidirectional effect on level-2 product, $R_{rs}(555 \text{ nm})$ and Chl_a .

The bidirectional effect correction factor can be emerged by two major factors, one is the underwater contributions (f/Q) by volumetric phase function of suspended particles (e.g., phytoplankton, inorganic suspended matters, detritus, etc.) and the other is Fresnel transmittance (\mathfrak{R}) at the air-sea interface (i.e., $c_{BF} = \mathfrak{R} \cdot f/Q$). In the case of the lower zenith angle, the effects are dominated by the underwater constituents. In contrast the higher zenith angle case, the directionality is more affected by the sea surface's Fresnel effect (Park and Ruddick, 2005).

The Fresnel transmittance term \mathfrak{R} can be separately considered into downward transmittance \mathfrak{R}_s and upward transmittance \mathfrak{R}_v , as,

$$\mathfrak{R} = \mathfrak{R}_s \mathfrak{R}_v, \quad (31)$$

$$\mathfrak{R}_s = Ed^{0-} / Ed^{0+}, \quad (32)$$

$$\mathfrak{R}_v = Eu^{0+} / Eu^{0-}, \quad (33)$$

where Ed^{0-} and Ed^{0+} are the downward irradiance respectively just beneath the water and just above the water. And terms Eu^{0+} and Eu^{0-} are upward irradiance respectively just above the water and just beneath the water. The upward Fresnel transmittance coefficient \mathfrak{R}_v is the function of viewing zenith angle and sea surface roughness by wind stress. For ocean color applications, the \mathfrak{R}_v can be simplified with assuming wind speed is zero at the surface level then it can be modeled (Franz et al., 2007) as

$$\mathfrak{R}_v(\theta_v) = \frac{0.9795218}{1.0 - t_w^f(\theta_v)}, \quad (34)$$

$$t_w^f(\theta_v) = \frac{t_w(0^\circ)}{t_w(\theta_v)}, \quad (35)$$

where $t_w(\theta_v)$ is the Fresnel transmittance of air-sea interface.

For the downward Fresnel transmittance coefficient \mathfrak{R}_s , Wang (2006) suggested a sun-angle and wind-speed dependent \mathfrak{R}_s correction model as Eq. 36,

$$\frac{\mathfrak{R}_s(\lambda, \theta_s = 0, W = 0)}{\mathfrak{R}_s(\lambda, \theta_s, W)} = 1 + \sum_{i=1}^4 c_i^{\mathfrak{R}}(\lambda, W) [\ln(\cos \theta_s)]^i. \quad (36)$$

where $c_i^{\mathfrak{R}}$ is constants of 4th order polynomial model.

In this study, $c_i^{\mathfrak{R}}$ values were derived from the successive-order-of-scattering simulation including polarization for SeaWiFS VIS bands (*i.e.*, 412, 443, 490, 510, 555, and 670 nm). These coefficients were readjusted according to GOCI bands characteristics (Ahn et al., 2015). Here, a three-step strategy was employed wherein the model for all simulation cases with given coefficients were first solved, then generated hyper-spectral values for each case by the spectral linear interpolation, and finally updated the correlation coefficients for GOCI bands by the least mean square error method as provided in Table 7.

Table 7. Adjusted coefficients (Eq.(47)) for GOCI bands (Wang,2006; Ahn et al., 2015).

λ (nm)	W (m/s)	$c_1^{\text{R}}(\lambda, W)$	$c_2^{\text{R}}(\lambda, W)$	$c_3^{\text{R}}(\lambda, W)$	$c_4^{\text{R}}(\lambda, W)$
412	0.0	-8.70×10^{-3}	6.38×10^{-2}	-3.79×10^{-2}	-3.11×10^{-2}
	1.9	-1.10×10^{-3}	9.26×10^{-2}	-5.30×10^{-4}	-2.05×10^{-2}
	7.5	6.80×10^{-5}	1.15×10^{-1}	6.49×10^{-2}	6.50×10^{-3}
	16.9	-8.80×10^{-3}	6.97×10^{-2}	4.24×10^{-2}	4.70×10^{-3}
	30.0	-8.10×10^{-3}	4.82×10^{-2}	2.90×10^{-2}	2.90×10^{-3}
443	0.0	-1.22×10^{-2}	4.15×10^{-2}	-7.80×10^{-2}	-4.27×10^{-2}
	1.9	-3.70×10^{-3}	7.46×10^{-2}	-3.71×10^{-2}	-3.25×10^{-2}
	7.5	-1.80×10^{-3}	1.12×10^{-1}	3.79×10^{-2}	-3.90×10^{-3}
	16.9	-9.70×10^{-3}	6.78×10^{-2}	3.28×10^{-2}	1.30×10^{-3}
	30.0	-8.90×10^{-3}	4.66×10^{-2}	2.20×10^{-2}	4.00×10^{-4}
490	0.0	-1.56×10^{-2}	1.88×10^{-2}	-1.16×10^{-1}	-5.11×10^{-2}
	1.9	-6.80×10^{-3}	5.34×10^{-2}	-7.62×10^{-2}	-4.38×10^{-2}
	7.5	-1.10×10^{-3}	1.08×10^{-1}	3.42×10^{-2}	-3.60×10^{-3}
	16.9	-1.04×10^{-2}	6.57×10^{-2}	2.33×10^{-2}	-1.60×10^{-3}
	30.0	-9.60×10^{-3}	4.50×10^{-2}	1.50×10^{-2}	-1.70×10^{-3}
555	0.0	-1.72×10^{-2}	4.80×10^{-3}	-1.37×10^{-1}	-5.26×10^{-2}
	1.9	-9.00×10^{-3}	3.68×10^{-2}	-1.05×10^{-1}	-5.06×10^{-2}
	7.5	-1.50×10^{-3}	1.04×10^{-1}	2.32×10^{-2}	-6.20×10^{-3}
	16.9	-1.10×10^{-2}	6.40×10^{-2}	1.66×10^{-2}	-3.10×10^{-3}
	30.0	-1.01×10^{-2}	4.39×10^{-2}	1.03×10^{-2}	-2.90×10^{-3}
660	0.0	-1.72×10^{-2}	4.30×10^{-5}	-1.43×10^{-1}	-4.82×10^{-2}
	1.9	-1.05×10^{-2}	2.47×10^{-2}	-1.24×10^{-1}	-5.39×10^{-2}
	7.5	-1.31×10^{-3}	1.03×10^{-1}	1.64×10^{-2}	-7.14×10^{-3}
	16.9	-1.11×10^{-2}	6.37×10^{-2}	1.29×10^{-2}	-3.57×10^{-3}
	30.0	-1.04×10^{-2}	4.34×10^{-2}	7.25×10^{-3}	-3.28×10^{-3}
680	0.0	-1.72×10^{-2}	-6.20×10^{-4}	-1.43×10^{-1}	-4.74×10^{-2}
	1.9	-1.07×10^{-2}	2.28×10^{-2}	-1.28×10^{-1}	-5.43×10^{-2}
	7.5	-1.29×10^{-3}	1.03×10^{-1}	1.52×10^{-2}	-7.24×10^{-3}
	16.9	-1.11×10^{-2}	6.37×10^{-2}	1.21×10^{-2}	-3.63×10^{-3}
	30.0	-1.04×10^{-2}	4.34×10^{-2}	6.79×10^{-3}	-3.32×10^{-3}

The in-water bidirectional function f/Q is modeled with assuming that the living and non-living biogenic particles in the water column are the major regulating factor in f/Q fluctuations ($-f/Q$ is a function of chl_a concentration). The f/Q value is computed using a look-up table simulated (Monte Carlo method) and provided by Morel et al. (2005). The theoretical basis of their work was reported in Morel et al. (2002).

The R_{rs} or nL_w that is the sun-sensor geometries are regulated to both zenith angles are set to be zero can be modeled as,

$$\begin{aligned}
 R_{rs}(\lambda) &= c_{BF}(\lambda, \theta_s, \theta_v, \phi_{s-v}, chl_a) \frac{\rho_{wm}(\lambda)}{\pi} \\
 &= \frac{\rho_{wm}(\lambda)}{\pi} \times \frac{\mathfrak{R}_s(\lambda, \theta_s=0, W) \mathfrak{R}_v(\lambda, \theta_v=0, W)}{\mathfrak{R}_s(\lambda, \theta_s, W) \mathfrak{R}_v(\lambda, \theta_v, W)} \\
 &\quad \times \frac{f(\lambda, \theta_s=0, chl_a) Q(\lambda, \theta_s, \theta_v, \phi_{s-v}, chl_a)}{Q(\lambda, \theta_s=0, \theta_v=0, \phi_{s-v}, chl_a) f(\lambda, \theta_s, chl_a)},
 \end{aligned} \tag{37}$$

$$nL_w(\lambda) = f_0(\lambda) R_{rs}(\lambda). \tag{38}$$

Fig. 23 is an example of the BRDF correction result (c_{BF}) computed in the GOCI atmospheric correction (13th/Aug./2013 03:16 UTC).

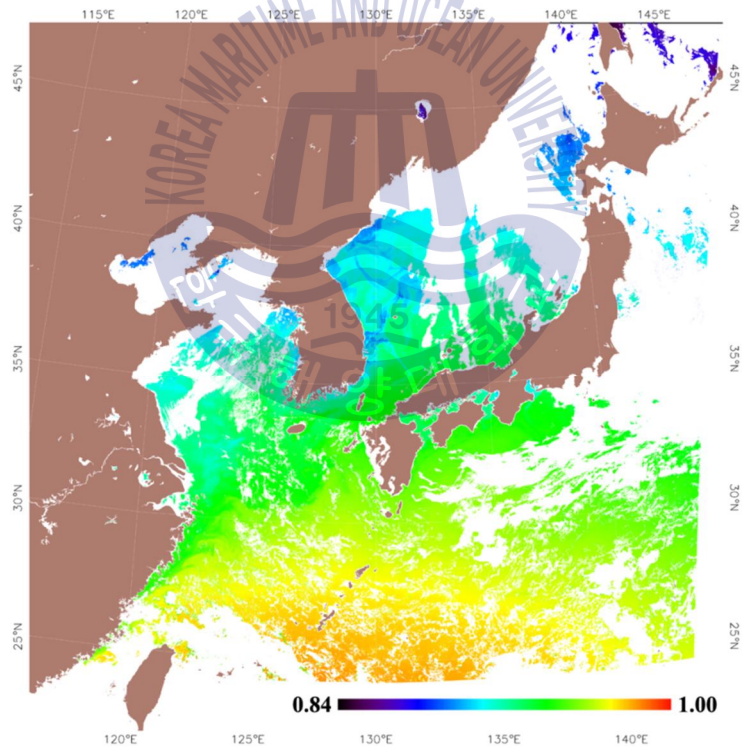


Fig. 23. An example of BRDF correction factor (c_{BF}) at 555 nm in the GOCI atmospheric correction process(2011/08/13, 3:16 UTC) (Morel et al., 2005; Wang, 2006; Ahn et al., 2015).

3.2.6. Correction for near-infrared water reflectance over turbid waters

In order to enhance the correlation between $\rho_{wn}(660 \text{ nm})$ and $\rho_{wn}(745 \text{ nm})$ used in the previous atmospheric correction scheme, the latest GOCI standard atmospheric correction method updated the spectral relationship model (Eq.39 rather than Eq.40). Besides, to better describe the non-linear relationship of extremely turbid-water reflectance values between these two NIR bands (Doron et al., 2011; Wang et al., 2012; Goyens et al., 2013a; Goyens et al., 2013b), the spectral relationship is updated in this study as Eq. 40.

$$\rho_{wn}(660 \text{ nm}) = \sum_{n=1}^5 j_n \rho_{wn}(745 \text{ nm})^n, \quad (39)$$

$$\rho_{wn}(865 \text{ nm}) = \sum_{n=1}^2 k_n \rho_{wn}(745 \text{ nm})^n. \quad (40)$$

This model has a dependency on the vicarious calibration because it is built with the satellite-collected water reflectance spectra (Ahn et al., 2012) through the nearest non-turbid water pixel atmospheric correction (Hu et al., 2000). Hence, coefficients of this model are adjusted after application of the vicarious gain factors (– it will be described in the next chapter). To obtain a new set of empirical data, turbid water reflectance spectra were collected from the Mokpo coastal region and East China Sea (denoted as MP and ECS, respectively) for several seasons.

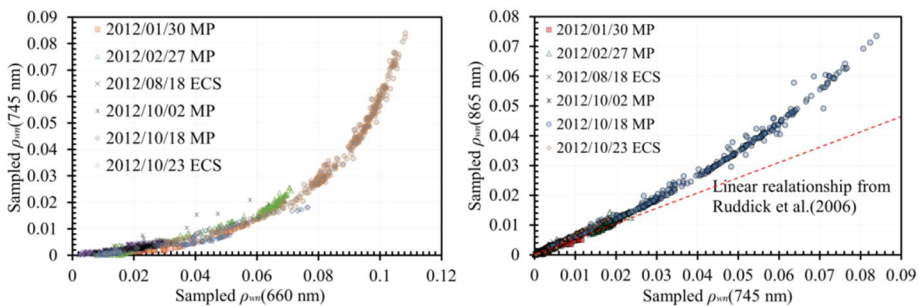


Fig. 24. Relationships between $\rho_{wn}(660 \text{ nm})$ and $\rho_{wn}(745 \text{ nm})$ and $\rho_{wn}(865 \text{ nm})$. The dashed line represents the linear relationship from the model of Ruddick et al. (2006) that the ratio of $\rho_{wn}(745 \text{ nm})$ to $\rho_{wn}(865 \text{ nm})$ is 1.936 used in Ahn et al. (2012).

To minimize any fluctuations of the water spectral relationship induced by the variation of aerosols, the nearest non-turbid pixel is accepted only when the $\rho_{\text{TOA}}(865 \text{ nm}) - \rho_r(865 \text{ nm})$ is less than 0.006. In addition, cases of high wind speed ($W < 6 \text{ m/s}$) and pixels affected by the ISRD and adjacency effects are excluded as well.

Finally, new statistical relationships are derived (Fig. 24). In these models, coefficients $j_1, j_2, j_3, j_4, j_5, k_1$ and k_2 of Eq. 39 and Eq. 40 are -0.00148, 0.4865, -22.93, 615.8, -6760.0, 30210.0, 0.5012, and 4.0878, respectively.

3.2.7. Atmospheric transmittance with considering anisotropic angular distribution of water reflectance

The diffuse transmittances implemented in the GDPS ver.1.1 atmospheric correction have been estimated by a quasi-analytic model with an assumption of isotropic water-leaving radiance and single-scattering assumption (Gordon et al., 1983; Ahn et al., 2012). However, this assumption is no more stand for high zenith angles and high aerosol optical thickness, and then it starts to produce errors up to 15% (Antoine, 2010).

To simulate anisotropic water reflectance in diffuse transmittance estimation, Chl_a concentration is fixed as 0.7 mg/m^3 acceptable because in-water bidirectional effect by water constituents is relatively less sensitive compared to other terms (Park and Ruddick, 2005; Antoine, 2010) for large zenith angles. The Rayleigh diffuse transmittance is simply predicted by using RTE-organized LUT regarding solar zenith angles and viewing zenith angles.

For the diffuse transmittance of aerosols in the presence of air molecules ($td_a \times td_{ra}$: hereafter refer to as td_{am}), the GOCI atmospheric correction employed a similar method with Wang (1999) and Antoine (2010) that uses a relationship between an approximate model and result of radiative transfer simulation. The approximate diffuse transmittance models tdm^s and tdm^v are established with assuming that the single scattering albedo multiply forward scattering probability is 0.95 for i^{th} aerosol models M_i as

$$tdm_{am}^s(M_i, \lambda) = \left(\exp - 0.05 \tau_a^{M_i}(\lambda) / \cos \theta_s \right), \quad (41)$$

$$tdm_{am}^v(M_i, \lambda) = \left(\exp - 0.05 \tau_a^{M_i}(\lambda) / \cos \theta_v \right), \quad (42)$$

where $\tau_a^{M_i}$ is aerosol optical thickness for i^{th} candidate aerosol model.

In the method, the 4th order polynomial relationship between the approximate model and the simulation result td_{am}^s and td_{am}^v is used as

$$td_{am}^s(M_i, \lambda) = \sum_{n=1}^4 \left(b_n^s tdm_{am}^s(M_i, \lambda) \right)^n, \quad (43)$$

$$td_{am}^v(M_i, \lambda) = \sum_{n=1}^4 \left(b_n^v tdm_{am}^v(M_i, \lambda) \right)^n, \quad (44)$$

where b_n^s and b_n^v are the constants of polynomial equation respectively for td_{am}^s and td_{am}^v that is stored in the look-up table (LUT) for each model M_i , θ_s , θ_v , and ϕ_{sv} .

From above equations, the aerosol optical thickness of i^{th} model ($\tau_a^{M_i}$) can be derived by the 3rd order polynomial relationship suggested by Fukushima et al. (1998) (– this will be further described in Chapter 5).

Direct transmittance is implemented to consider sun-glint attenuation by atmosphere. For estimating direct transmittance by aerosols in the presence of air molecules ($tg_a \times tg_{ra}$: hereafter refer to as tg_{am}) and air-molecules in the absence of aerosols (tg_r), the traditional quasi-analytic model (Eqs. 45 ~ 48) is applied as,

$$tg_{am}^s(\lambda) = \exp \left\{ -\tau_a^{M_i}(\lambda) / \cos(\theta_s) \right\}, \quad (45)$$

$$tg_{am}^v(\lambda) = \exp \left\{ -\tau_a^{M_i}(\lambda) / \cos(\theta_v) \right\}, \quad (46)$$

$$tg_r^s(\lambda) = \exp \left\{ -\tau_r(\lambda) / \cos(\theta_s) \right\}, \quad (47)$$

$$tg_r^v(\lambda) = \exp \left\{ -\tau_r(\lambda) / \cos(\theta_v) \right\}. \quad (48)$$

3.3. Vicarious calibration for GOCI system

Space-borne ocean color sensors record the total radiance exiting the top-of-atmosphere (TOA) at several wavelengths within the visible (VIS) and near-infrared (NIR) spectral domain. The physical interpretation of these ocean color data needs an additional vicarious calibration other than

instrument calibration and characterization to achieve the desired accuracy on the normalized water-leaving radiance (nL_w) product retrieved by an atmospheric correction algorithm. Vicarious calibration of ocean color sensors is generally achieved through the application of gain factors to TOA-radiances (L_{TOA}), which effectively update the prelaunch and onboard instrument calibration to account for characterization errors or undetermined post-launch changes in sensor response, as well as any systematic bias associated with the atmospheric correction algorithm (Gordon, 1998; Eplee et al., 2001; Wang and Gordon, 2002; Murakami et al., 2005; Lerebourg et al., 2011; Werdell et al., 2007; Franz et al., 2007; Wang et al., 2013a; Wang et al., 2013b, Ahn et al., 2015). The atmospheric correction is required to retrieve the surface radiance from remotely sensed TOA-radiances by removing the atmospheric effects. In a typical open-ocean region of oligotrophic waters, the upwelling radiance emerging out of the water surface contributes $\sim 10\%$ to the radiance at the TOA (Gordon, 1998; Eplee et al., 2001; Wang and Gordon, 2002; Franz et al., 2007). Therefore, it is crucial to retrieve this small portion of the water-leaving radiance by removing the major portion of atmospheric (molecules and aerosols) contributions and specular reflection at the sea surface.

For retrieving water-leaving radiances with the desired accuracy for all channels, the atmospheric path radiances resulting from scattering by air molecules and aerosols must be estimated precisely, and this is often achieved through simulation of TOA radiance with a radiative transfer code. In general, the TOA radiances atmospherically corrected within an accuracy of less than 1% error (Eplee et al., 2001) secure high-quality level-2 ocean color products. However, this is seldom achieved by the atmospheric correction process which often results in systematic errors in retrieved water-leaving radiance. Thus, the vicarious calibration gain factors are applied in combination with the atmospheric correction algorithm to force the instrument response to retrieving the expected values of $nL_w(\lambda)$ (Franz et al., 2007). This procedure has been adopted for many ocean color sensors (Gordon, 1998; Eplee et al., 2001; Wang and Gordon, 2002; Murakami et al., 2005; Lerebourg et al., 2011; Werdell et al., 2007; Franz et al., 2007; Wang et al., 2013a; Wang et al., 2013b, Ahn et al., 2015), e.g., Moderate Resolution Imaging Spectroradiometer (MODIS), Sea-Viewing Wide Field-of-View Sensor (SeaWiFS), Global Imager (GLI), MEduM Resolution

Imaging Spectrometer (MERIS), and Visible Infrared Imaging Radiometer Suite (VIIRS). Vicarious calibration is the process used to compute vicarious gains (g_{vc}) for the indirect calibration of space-borne sensors through simulation of TOA data. These gain factors are determined by the mean ratio of the simulated TOA radiance (L_{TOA}^{VC}) to the TOA radiance at-sensor observation (L_{TOA}):

$$g_{vc}(\lambda) = \left[\sum_{n=1}^N \left\{ L_{TOA}^{VC}(\lambda) / L_{TOA}(\lambda) \right\} \right] / N, \quad (49)$$

where λ denotes the wavelength and N is the number of samples used for deriving the vicarious calibration gain factors. The vicarious calibration gain factors aim to minimize the combined effects of uncertainties due to the pre-launch radiometric calibration and characterization of the satellite sensor corrected for temporal changes in radiometric sensitivity and inaccuracy of the atmospheric correction algorithm. Hence, this adjustment of the system (sensor+algorithm) response allows the determination of nL_w with the least uncertainty.

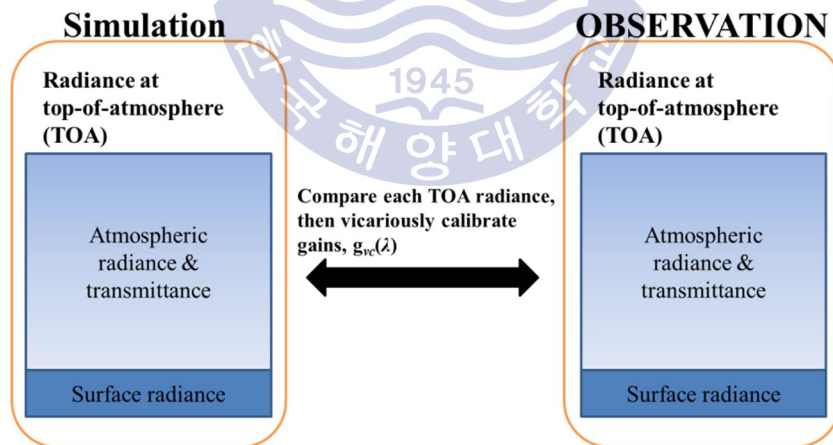


Fig. 25. Conceptual diagram of the vicarious calibration

In this chapter, a vicarious calibration approach for the GOCI mission is described in detail. The vicarious calibration process adopted here is almost identical to that previously employed to

calibrate polar-orbiting ocean color sensors (Gordon, 1998; Eplee et al., 2001; Wang and Gordon, 2002; Murakami et al., 2005; Lerebourg et al., 2011; Werdell et al., 2007; Franz et al., 2007; Wang et al., 2013b, Ahn et al., 2015). In a traditional way, the vicarious gain factors are derived for each band on the GOCI through simulations of the satellite radiance along with *in situ* radiometric measurements. Initially, the calibration of GOCI NIR (near-infrared) band is achieved over a pre-defined open-ocean site based on knowledge of the assumed aerosol type. Subsequently, the atmospheric path radiances (both Rayleigh and aerosol) are computed over arbitrary locations of the ocean using the calibrated NIR bands. To derive the calibration gain factors, the theoretical TOA radiances (L_{TOA}^{VC}) in the visible bands (412, 443, 490, 555, 660, and 680 nm) are generated through simulations for certain locations where *in situ* radiometric measurements (nL_w) are available.

3.3.1. Method

In view of describing the vicarious calibration process in detail, the simulated TOA radiance $L_{TOA}^{VC}(\lambda)$ representing the radiance contributions associated with air molecules (Rayleigh scattering), aerosols (including Rayleigh-aerosol interactions), sunglint, white-caps, and the water itself can be described by the following simplified model (Wang and Gordon, 1994; Wang, 2010) in a similar manner to the Eq.(7):

$$L_{TOA}^{VC}(\lambda) = \left[\begin{array}{l} L_r(\lambda) + L_a(\lambda) + L_{ra}(\lambda) \\ +td_r^v(\lambda) \times td_{am}^v(\lambda) \times \{L_w^{VC}(\lambda) + L_{wc}(\lambda)\} \\ +tg^s(\lambda) \times tg^v(\lambda) \times \rho_g(\lambda) \end{array} \right] \times t_{oz}^v(\lambda) \times t_{oz}^s(\lambda), \quad (50)$$

where $L_r(\lambda)$ is the Rayleigh radiance (arising due to single- and multiple-scattering) in the absence of aerosols, $L_a(\lambda) + L_{ra}(\lambda)$ is the radiance due to multiple-interactions between aerosols and air molecules, $L_{wc}(\lambda)$ is the radiance arising from light reflection on the whitecaps at the sea surface (Frouin et al., 1996; Stramska and Petelski, 2003), and $L_w^{VC}(\lambda)$ is the desired L_w that varies depending on the viewing angle of the sensor.

As the atmospheric correction scheme described in Chapter 2 and 3, the Rayleigh radiance $L_r(\lambda)$

can be reliably estimated given the radiant-path geometries and look-up tables (Gordon et al., 1988; Gordon and Wang 1992; Wang, 2002; Wang 2005). However, estimation of the radiance $L_a(\lambda)+L_{ra}(\lambda)$ is difficult due to the variation of aerosols in space and time, which constitutes a substantial limitation in the estimation of $L_{TOA}^{VC}(\lambda)$. The GOCI vicarious calibration follows a two steps strategy, *i.e.*, the GOCI NIR bands are calibrated first, and then the retrieved aerosol properties (aerosol type and concentration) for these bands to subsequently predict aerosol radiances are used for all visible bands. The aerosol radiance at two NIR bands can be reliably estimated over typical case-1 waters where the NIR water-leaving radiances approach to zero, thus validating the black pixel assumption (*i.e.*, water-leaving radiance is negligible in the NIR bands) (Wang and Gordon, 1994; Gordon and Wang, 1994). A similar approach was adopted in other studies (*e.g.*, Eplee et al., 2001; Wang and Gordon, 2002; Franz et al., 2007; Ahn et al., 2015). In the vicarious calibration, assuming the longest NIR band (865nm) is correct, the vicarious calibration gain factor for the shorter NIR band (745 nm) is determined based on the known aerosol type. To achieve the NIR calibration, an open-ocean site far away from land is chosen wherein the aerosol type is maritime that is of oceanic origin and generally stable. The calibration of these two NIR bands is the basis for deriving the aerosol properties in any arbitrary locations of non-turbid water, eventually allowing the estimation of the aerosol radiance $L_a(\lambda)+L_{ra}(\lambda)$ for all VIS bands.

3.3.2. Inter-calibration of GOCI near-infrared bands

Because of the lack of reliable, coincident, and co-located aerosol properties and water-leaving radiances from *in situ* measurements, the GOCI calibration approach used several assumptions to determine aerosol contribution and estimate $L_{TOA}^{VC}(745\text{ nm})$. To calibrate the shorter NIR band (745 nm), the $L_{TOA}^{VC}(745\text{ nm})$ can be estimated from the observed aerosol radiance at 865 nm. For the open ocean, it can be assumed that the aerosol type of the site is always identical to a maritime aerosol model (Eplee et al., 2001; Franz et al., 2007). The constant characteristics represent the mean of relative humidity (RH) 80% maritime aerosol model (M80) is accepted based on meteorological data. To avoid, as far as possible, aerosols originating from continents and the effects of inter-slot-radiometric-discrepancy (ISRD) (Kim et al., 2015), the *NIR* vicarious calibration site as

a boxed area of 25.7-26.7°N and 138.4-139.4°E is selected as shown in Fig. 26. It should be noted that NIR calibration sites previously established by Wang et al. (2013a) and Ahn et al. (2015) are discarded in this study to avoid aerosols from the continent. Because revised investigation has shown that the site of Wang et al. (2013a) is often effected by aerosols from the continent, and aerosol types in the site of Ahn et al. (2015) are not homogeneous. To perform the NIR calibration, the spatial and temporal (2011-2014) averages of GOCI observations of cloud-glint-free $L_{TOA}(\text{NIR})$ on a 10×10 pixel area are computed to minimize the effects of spurious outliers.

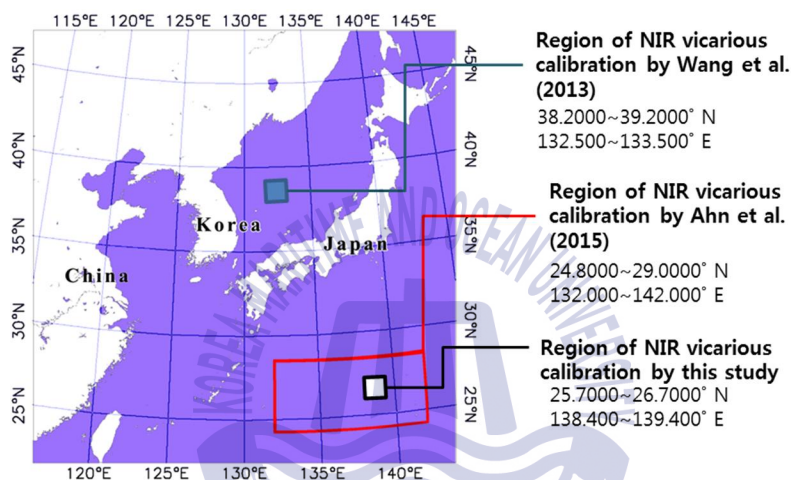


Fig. 26. Map of the calibration site for the GOCI NIR bands. The region within the box of 25.7-26.7°N and 138.4-139.4°E (red rectangle) in the GOCI coverage is established for the NIR vicarious calibration. The region is selected so as to avoid continental aerosols and slot boundary stray-light effects. NIR calibration sites previously established by Wang et al. (2013a) and Ahn et al. (2015) are discarded in this study.

To estimate the aerosol contribution at the shorter NIR band (745nm), the aerosol radiance estimated for the longer NIR band (865nm) (see the Chapter 2) was conveniently converted to reflectance, $\rho_a(865 \text{ nm}) + \rho_{ra}(865 \text{ nm})$. Subsequently, the $\rho_a(745 \text{ nm}) + \rho_{ra}(745 \text{ nm})$ was derived using the look-up table generated through radiative transfer simulations and the single-scattering reflectance model. For the radiative transfer simulation, the Second Simulation of a Satellite Signal in the Solar Spectrum, Vector, version 1 (6SV1) (Vermote et al., 2006) was used.

Since the NIR calibration site has the characteristic of typical case-1 waters, $L_w^{VC}(\text{NIR})$ in

equation (50) is negligible by the BPA. Then it is straightforward to reliably estimate the NIR aerosol multiple-scattering reflectance in the presence of air molecules $\rho_{am}(\text{NIR}_L)$ similar to the atmospheric correction scheme,

$$L_a(\text{NIR}) + L_{ra}(\text{NIR}) = \frac{L_{rOA}(\text{NIR})}{t_{oz}^s(\lambda) t_{oz}^v(\lambda)} - L_r(\text{NIR}) - td_r^v(\lambda) L_{wc}(\text{NIR}). \quad (51)$$

The aerosol radiance can be converted to reflectance as follow:

$$\rho_{am}(\lambda) = \pi \frac{L_a(\lambda) + L_{ra}(\lambda)}{F_0(\lambda) \cos(\theta_s)}. \quad (52)$$

From the derived $\rho_{am}(865 \text{ nm})$ and an assumed aerosol type (M80), aerosol reflectance for the GOCI NIR 745nm band is first estimated using the SRAMS. The aerosol multiple-scattering reflectance at 865 nm can be converted into aerosol multiple-scattering reflectance at 745 nm by using Eq. (26) as

$$\rho_{am}^{VC}(745 \text{ nm}) = \sum_{n=1}^2 c_n (M_{M80}, \lambda, \theta_s, \theta_v, \phi_{sv}) \rho_{am}(865 \text{ nm})^n. \quad (53)$$

Finally, the theoretical TOA radiance at 745 nm ($L_{TOA}^{VC}(745 \text{ nm})$) is calculated using an analytic model incorporated into the atmospheric correction process (Ahn et al., 2015) (Fig. 27):

$$L_a^{VC}(745 \text{ nm}) + L_{ra}^{VC}(745 \text{ nm}) = \rho_{am}^{VC}(745 \text{ nm}) \times F_0(745 \text{ nm}) \cos(\theta_s) / \pi, \quad (54)$$

$$\begin{aligned} L_{TOA}^{VC}(745 \text{ nm}) = & \left\{ L_r(745 \text{ nm}) + L_a^{VC}(745 \text{ nm}) + L_{ra}^{VC}(745 \text{ nm}) \right\} \\ & \times t_{oz}^v(745 \text{ nm}) t_{oz}^s(745 \text{ nm}) \\ & + L_{wc}(745 \text{ nm}) \\ & \times t_{oz}^v(745 \text{ nm}) td_r^v(745 \text{ nm}) td_{am}^v(745 \text{ nm}). \end{aligned} \quad (55)$$

In the above equations, the term $L_r(\lambda)$ can be reliably estimated to less than 1% error (Gordon et al, 1988; Gordon and Wang, 1992; Wang, 2002, Wang, 2005).

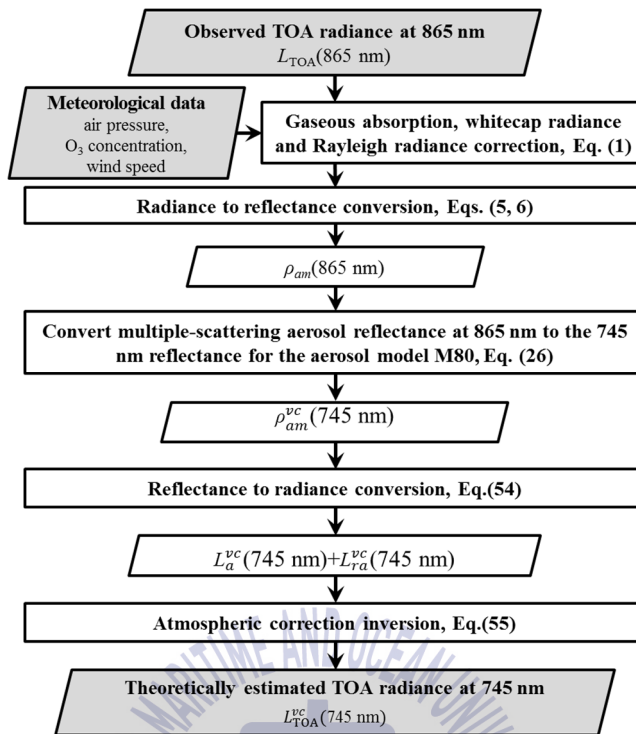


Fig. 27. Flow chart describing the scheme for estimating the TOA radiance at 745 nm.

To reduce uncertainties in $\rho_{am}(\lambda)$, strict accept criteria are followed; *i.e.*, the wind speed is below 4.6 m/s to reduce NIR inter-calibration errors involved by whitecap radiance error, $\rho_{am}(865 \text{ nm})$ is lower than 0.020, and scene observation times are only for period 2:16~4:16 (UTC) to avoid high air mass.

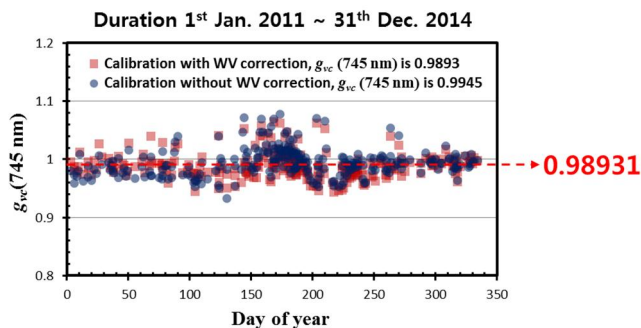


Fig. 28. The result of NIR bands inter-calibration with/without considering the water vapor effect. In the NIR calibration site, water vapor effects the $g_{vc}(745 \text{ nm})$ more than 0.5%.

Vicarious gain at 745 nm is determined as 0.98931. As shown in Fig. 28 water vapor effect in NIR is also considerable (~0.05% in 745nm vicarious gain).

3.3.3. Vicarious calibration of GOCI visible bands

The calibration process of the visible bands depends on a set of high-quality satellite-to-*in situ* match-up pairs that were sampled at discrete locations and subsequently reduced in number through quality screening. Approach to the vicarious calibration of the visible bands is based on the GOCI standard atmospheric correction algorithm (Ahn et al., 2012; Ahn et al., 2015; Ahn et al., 2016) which estimates the aerosol reflectance in the two NIR bands. Since the NIR bands are already inter-calibrated, the atmospheric correction process can be operated to determine aerosol multiple-scattered reflectance for all VIS bands ($\rho_{am}(\text{VIS})$). For each *in situ* $L_w^{VC}(\lambda)$ location, the theoretically estimated $L_{TOA}^{VC}(\text{VIS})$ values can be derived from the atmospheric path radiance, transmittance and whitecap radiance from the atmospheric correction process, and the $L_w^{VC}(\lambda)$ subsequently corrected the bidirectional effects (– it will be further described in Chapter 4) through equation (50) and Fig. 29 (Wang and Gordon, 2002; Franz et al., 2007; Ahn et al., 2012, Ahn et al., 2015):

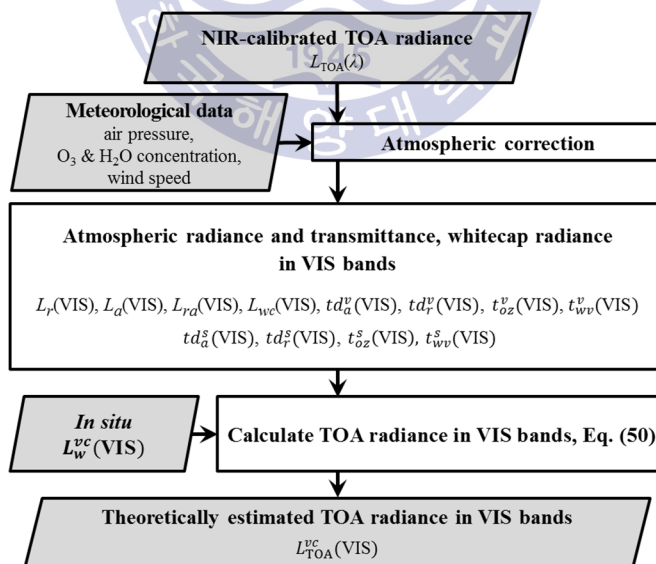


Fig. 29. A flow chart describing the scheme for estimating the TOA radiance in the visible bands.

To avoid uncertainties that would arise from case-2 waters during the atmospheric correction and f/Q correction processes, the extensive quality screening of the *in situ* and GOCI observations allows only the clear-water $L_w^{VC}(\lambda)$ such that $L_w^{VC}(660\text{ nm})/t_{oz}^s(660\text{ nm})/t_r^s(660\text{ nm})$ is less than $2.0\text{ w}\cdot\text{m}^{-2}\cdot\mu\text{m}^{-1}\cdot\text{sr}^{-1}$. To further assure the quality of these data, any of the pixels at each VIS bands calibration site flagged by the atmospheric correction process as being contaminated by bright pixel adjacency effects (from land or stray-light or cloudless than 5 km) and ISRD effects (slot distance $\sim 150\text{ km}$) is excluded from further consideration. In addition, both the sensor and solar zenith angle is restricted to less than 40 degrees to minimize errors from the large total air-mass.

After the VIS bands calibration, the GOCI vicarious gains are determined within instrument calibration uncertainty (around $\pm 3.8\%$) as 1.00531, 0.99113, 0.96805, 0.97044, 0.97391, 0.97698, 0.98931, and 1.0 for GOCI bands 412, 443, 490, 555, 660, 680, 745, and 865 nm, respectively. As shown in Fig. 30, the calibration reduced the clear water atmospheric correction errors in absolute percentage distribution (APD) by 54.4, 14.3, 25.7, 29.2, 7.0, and 3.3% for GOCI bands 412, 443, 490, 555, 660, 680, 745, and 865 nm, respectively.

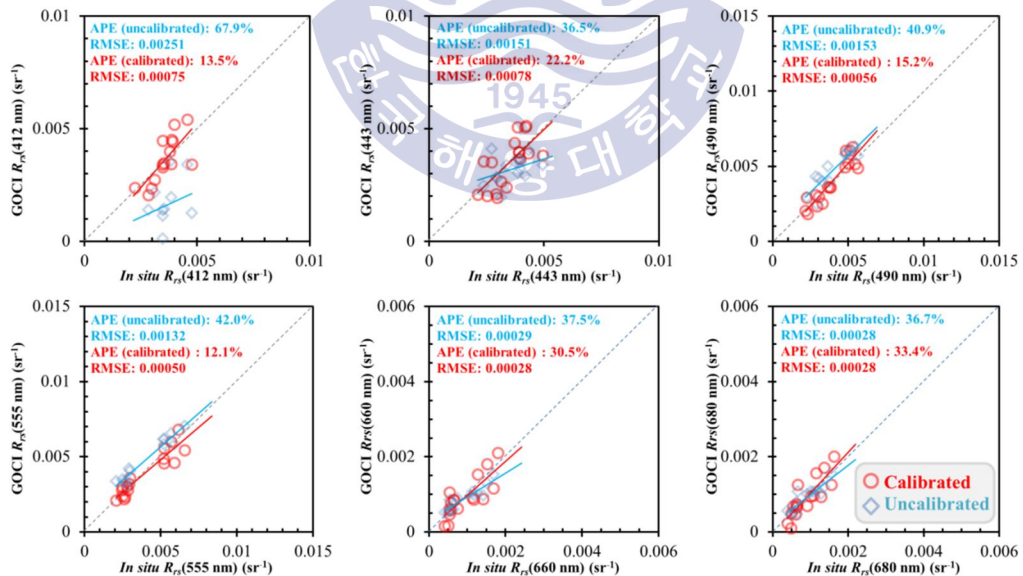


Fig. 30. The result of the VIS band calibration. Blue marks and red marks are matches without/with the calibration in clear waters, respectively.

Chapter 4. Validation results

4.1. Data

Performance of the GOCI standard atmospheric correction was assessed in two ways, one is by the radiative transfer simulation and the other is by *in situ* radiometric data after the application to the GOCI data.

This section will first describe *in situ* radiometric data acquisition and quality analyzing from a shipboard and the instrument equipped in observation towers (AERONET-OC). Then the detail information of the radiative transfer simulations for the comparison of primary atmospheric correction algorithms will be presented. This will also give the information for the processing of L_w^{VC} including the correction of bidirectional effects.

4.1.1. Synthetic data derived by simulations

To test the reliability of the atmospheric correction using the SRAMS approach, various pseudo-TOA reflectances were generated by Eq.(7) using a radiative transfer simulation (Vermote et al., 2006) for atmospheric components and an biogenic ocean color model (Morel and Maritorena, 2001) for water reflectances (Fig. 31). Six aerosol models based on Shettle and Fenn (1979) but not identical to 9 candidate models –Maritime, Coastal, and Tropospheric models with different RH (i.e., M98, M80, C90, C80, T90, and T50) were used to compute atmospheric reflectances and transmittances for observation geometries: $\theta_s = 0^\circ, 25^\circ, 50^\circ, \text{ and } 75^\circ$, $\theta_v = 0^\circ, 20^\circ, 40^\circ, \text{ and } 60^\circ$, and ϕ_{sv} are from 0° to 180° with 15° gap.

Water reflectances were computed (Fig.) for chl_a concentrations 0.03, 0.1, 0.3, and 1.0 mg/m^3 without inorganic particulate matter. It should be noted that case-2 water reflectance is ignored for the simulation because this study focuses on only the aerosol reflectance retrieval.

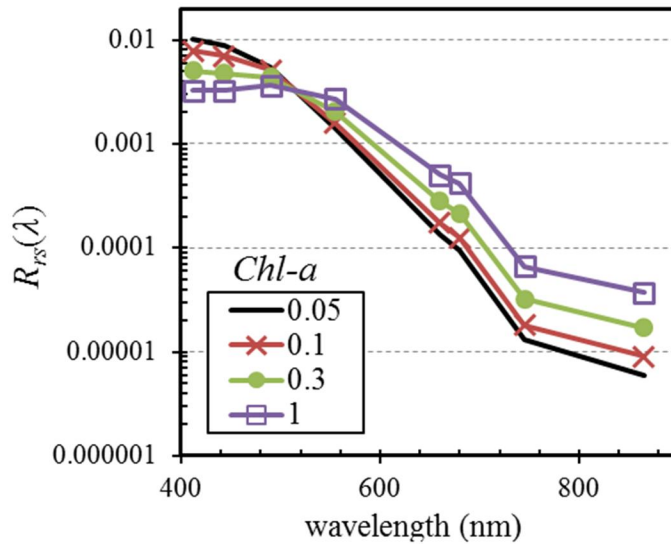


Fig. 31 Remote-sensing reflectance for *chl_a* concentrations 0.03, 0.1, 0.3, and 1.0 mg/m³ without inorganic particulate m0.03, 0.1, 0.3, and 1.0 mg/m³ by using biogenic ocean color model (Morel and Maritorena, 2001)

4.1.2. *In situ* radiometric data measured from shipboard

The Korea Ocean Satellite Research Center (KOSC), KIOST, has conducted a large number of field campaigns in coastal and open ocean waters around Korea and obtained 421 *in situ* above-water radiometric measurements since 2010 (Fig. 32). The normalized water-leaving radiance $nL_w(\lambda)$ or the remote-sensing reflectance $R_{rs}(\lambda)$ was measured by the ASD-FieldSpec and TriOS-RAMSES hyperspectral radiometers. Of the 421 samples, 356 spectra were discarded by the strict quality control process recommended by Moon et al. (2012), which left only 65 samples for the match-up process and analysis. Of those 65 samples, most of the shipboard data were collected from highly to moderately turbid waters in which the $R_{rs}(660 \text{ nm})$ is greater than 0.0013. After eliminating these turbid water measurements, a relatively small number of the potential match-ups from non-turbid water areas (*i.e.* 12 R_{rs} measurements) is eventually utilized in the VIS bands vicarious calibration process.

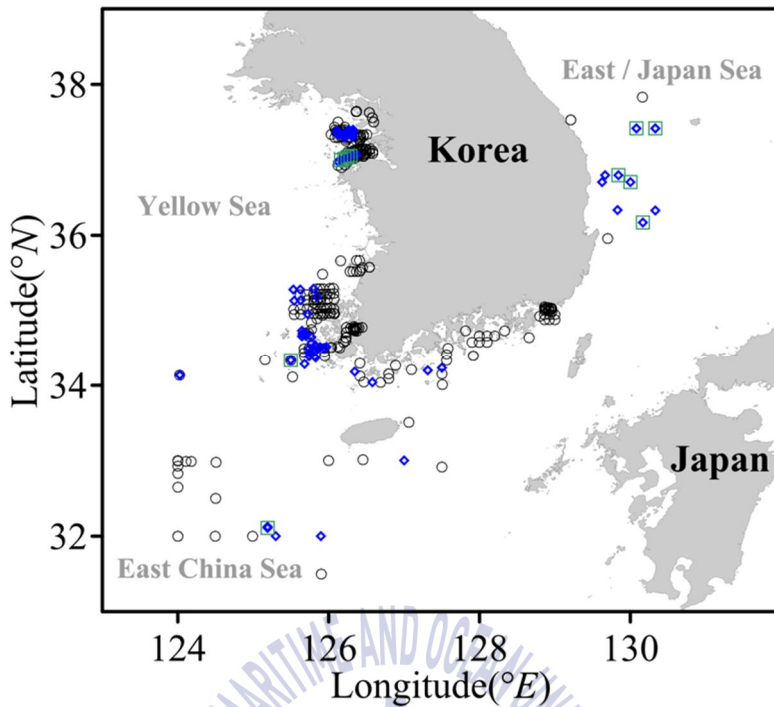


Fig. 32. Locations of *in situ* radiometric measurements in coastal and open-ocean waters around Korea. A total of 421 samples were collected, and subsequently reduced to 65 (blue diamonds) through strict quality control of both the *in situ* measurements and GOCI observations. Of these data, only 14 spectra were used in the vicarious calibration process (green squares).

In the above-water measurement system, three radiometric measurements are required for determination of the L_w or R_{rs} ; *i.e.*, the total radiance leaving the water surface $L_{sea}^{0+}(\lambda)$, sky radiance $L_{sky}(\lambda)$, and downwelling irradiance $E_d(\lambda)$ (Mobley, 1999; Mueller et al., 2000). The L_w and the remote sensing reflectance before the bidirectional effect correction (R_{rs}^m) can be determined as follows:

$$L_w(\lambda) = L_{sea}^{0+}(\lambda) - f_{surf} L_{sky}(\lambda) - L_b(\lambda), \quad (56)$$

$$R_{rs}^m(\lambda) = \frac{L_{sea}^{0+}(\lambda) - f_{surf} \times L_{sky}(\lambda)}{E_d(\lambda)} - R_b, \quad (57)$$

where f_{surf} is the air-sea Fresnel reflectance ratio, which is spectrally constant and can be estimated as a function of wind speed ($0.0256 + 0.00039W + 0.000034W^2$, where W is the wind speed in $m \cdot s^{-1}$). The unknown term $L_b(\lambda)$ is the residual radiance from light reflected by the ship's superstructure, microfoam, or fluctuated $f_{surf} \times L_{sky}(\lambda)$. The term R_b (i.e., L_b/E_d) is assumed to have no spectral dependency and thus is constant across the visible wavelengths.

To derive R_b , a remote-sensing reflectance model (linking R_{rs} to the inherent optical properties, IOP) is employed to fit the *in situ* R_{rs} measurements to the model R_{rs} (R_{rs}^{model}). The general expression of this model takes the form (Lee et al., 2009):

$$r_{rs}^{model}(\lambda) = 0.089 \left(\frac{b_b(\lambda)}{a(\lambda) + b_b(\lambda)} \right) + 0.125 \left(\frac{b_b(\lambda)}{a(\lambda) + b_b(\lambda)} \right)^2, \quad (58)$$

$$R_{rs}^{model}(\lambda) = \frac{0.52 r_{rs}^{model}(\lambda)}{1 - 1.7 r_{rs}^{model}(\lambda)}, \quad (59)$$

where r_{rs}^{model} is the remote-sensing reflectance just below the surface, $b_b(\lambda)$ is the total backscattering coefficient, and $a(\lambda)$ is the total absorption coefficient. In the NIR region, the water absorption (a_w) is dominant and thus determines the spectral shape of the $b_b(\text{NIR}) / \{a(\text{NIR}) + b_b(\text{NIR})\}$ term in Eq. (58) (Ruddick et al., 2006).

Here a spectral fitting technique (Moon et al., 2012) with measurements from Ruddick et al. (2006) is used to estimate the R_b over the wavelength range of 770-870 nm when $R_{rs}(660) > 0.0025$. The wavelength range is shifted to 700-745nm for relatively clear waters, where $R_{rs}(660) \leq 0.0025$, to avoid a low signal-to-noise ratio (SNR) in this red-NIR spectral region where $L_{sea}^{0+}(\lambda)$ is weak due to strong absorption. Fig. 33 shows examples of the R_b correction for both clear and turbid waters.

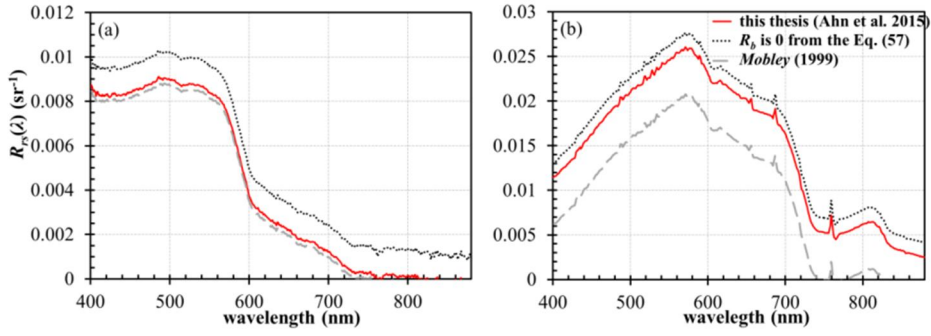


Fig. 33. R_b correction applied to $R_{rs}^m(\lambda)$ from clear (a) and turbid (b) waters. Red solid lines represent the corrected R_{rs} , and black dotted lines indicate uncorrected data directly derived from Eq. (57) with R_b is zero. Grey dashed lines show the results obtained by subtracting the $R_{rs}(755 \text{ nm})$ value from each wavelengths (Mobley, 1999).

Then, *in situ* R_{rs}^m is converted into R_{rs} and nL_w that normalized to both the sun and viewing angles as (see the Chapter 2 for a further description):

$$\begin{aligned}
 R_{rs}(\lambda) \text{ or } nL_w(\lambda) &= \left\{ R_{rs}^m(\lambda) \text{ or } nL_w^m(\lambda) \right\} \\
 &\times \frac{\mathfrak{R}_s(\lambda, \theta_s=0, W)}{\mathfrak{R}_s(\lambda, \theta_s=\theta_s^m, W)} \times \frac{\mathfrak{R}_v(\lambda, \theta_v=0, W)}{\mathfrak{R}_v(\lambda, \theta_v=\theta_v^m, W)} \\
 &\times \frac{f(\lambda, \theta_s=0, chl_a)}{f(\lambda, \theta_s=\theta_s^m, chl_a)} \times \frac{Q(\lambda, \theta_s=\theta_s^m, \theta_v=\theta_v^m, \phi_{s-v}=\phi_{s-v}^m, chl_a)}{Q(\lambda, \theta_s=0, \theta_v=0, \phi_{s-v}=0, chl_a)},
 \end{aligned} \tag{60}$$

$$nL_w(\lambda) = R_{rs}(\lambda) \times f_0(\lambda). \tag{61}$$

where θ_s^m , θ_v^m , and ϕ_{s-v}^m are each θ_s , θ_v , and ϕ_{s-v} associated with the time and location of each measurement.

For the vicarious calibration usage, the nL_w is finally converted to the L_w^{VC} with considering the bidirectional effect as following:

$$\begin{aligned}
L_w^{VC}(\lambda, \theta_s^m, \theta_v^m, \phi_{s-v}^m) = & \left\{ nL_w(\lambda) \times c_{s-e}(d_v) \times \cos(\theta_s = \theta_s^t) \times td_r^s(\lambda) \times td_a^s(\lambda) \times t_{oz}^s(\lambda) \right\} \\
& \times \frac{\mathfrak{R}_s(\lambda, \theta_s = \theta_s^t, W)}{\mathfrak{R}_s(\lambda, \theta_s = 0, W)} \times \frac{\mathfrak{R}_v(\lambda, \theta_v = \theta_v^t, W)}{\mathfrak{R}_v(\lambda, \theta_v = 0, W)} \\
& \times \frac{f(\lambda, \theta_s = \theta_s^t, chl_a)}{f(\lambda, \theta_s = 0, chl_a)} \times \frac{Q(\lambda, \theta_s = 0, \theta_v = 0, \phi_{s-v} = 0, chl_a)}{Q(\lambda, \theta_s = \theta_s^t, \theta_v = \theta_v^t, \phi_{s-v} = \phi_{s-v}^t, chl_a)},
\end{aligned} \tag{62}$$

where θ_s^t and θ_v^t are the desired-zenith angles for the sun and the sensor of each GOCI observations, respectively.

4.1.3. AERONET-OC radiometric data

At the Jeodo station (Shim et al., 2004), there is no level 2.0 AERONET-OC data that the quality is fully assured (Zibordi et al., 2006; Zibordi et al., 2009). Moreover, Moon et al. (2012) requires IOP pairs to build R_{rs} optical closure, however, AERONET-OC does not measure them. Therefore, a new data screening approach is applied that uses a different method from Moon et al. (2012). To set optical boundaries, a series of empirical relationships of R_{rs} spectra are simulated by HYDROLIGHT (Mobley and Sundman, 2008).

In this study, various R_{rs} spectra are computed using the following input parameters:

- Pure water IOPs are taken from Smith and Baker (1981), Pope and Fry (1997), and Kou et al.(1993).
- We set chl_a concentration range as 0.1~30.0 mg/m³. Then, its IOP are taken from Morel (1988), and Loisel and Morel (1998). Specific absorption of chl_a in 740~880 nm is assumed to be zero.
- CDOM absorption range at 440 nm considered is 0.1~0.3 m⁻¹.
- Suspended sediment concentration range is 0.1~1000.0 g/m³. From Ahn (1990), IOP of 4 mineral types, namely red clay (RC), yellow clay (YC), calcareous sand (CS), and brown earth (BE), were considered. Each absorption and backscattering coefficient spectra were extrapolated over the NIR range (Mobley and Sundman, 2008).
- Inelastic scattering effects (chl_a fluorescence, CDOM fluorescence, and Raman scattering) are considered.
- Wavelength range of the simulation considered is 400~880 nm per 5 nm bandwidth. Then convert into AERONET-OC bands.

Finally, the following spectral relationships are developed; between $R_{rs}(443 \text{ nm})/R_{rs}(555 \text{ nm})$ and $R_{rs}(668 \text{ nm})$ [Fig. 34(a)], between $R_{rs}(412 \text{ nm})/R_{rs}(443 \text{ nm})$ and $R_{rs}(668 \text{ nm})$ [Fig. 34(b)], between $R_{rs}(443 \text{ nm})/R_{rs}(490 \text{ nm})$ and $R_{rs}(668 \text{ nm})$ [Fig. 34(c)], between $R_{rs}(668 \text{ nm})/R_{rs}(555 \text{ nm})$ and $R_{rs}(668 \text{ nm})$ [Fig. 34(d)], and between $R_{rs}(869 \text{ nm})/R_{rs}(668 \text{ nm})$ and $R_{rs}(668 \text{ nm})$ [Fig. 34(e)]. Then some data are excluded which exhibited spectral relationships out of boundary conditions (blue-dashed closures) [Fig. 34]. Except the relationship between $R_{rs}(869 \text{ nm})/R_{rs}(668 \text{ nm})$ and $R_{rs}(668 \text{ nm})$ [Fig. 34(e)], those boundaries do not consider $R_{rs}(668)$ less than 0.0045 because these relationships showed high variations in this reflectance range.

It should be noted that the verification of IOP models is beyond the scope of this study. Moreover, those IOP models have not been developed for the GOCI area, hence they would not be consistent with the underwater optical environments of the calibration sites. Moreover, the extrapolated IOPs in the NIR may lead to unrealistic relationships between $R_{rs}(869 \text{ nm})/R_{rs}(668 \text{ nm})$ and $R_{rs}(668 \text{ nm})$. For these reasons, further investigations regarding IOPs at the study sites are needed for future improvement. Because of a lack of IOP verifications, the method excluded 60 unrealistic spectra as shown in Fig. 35.

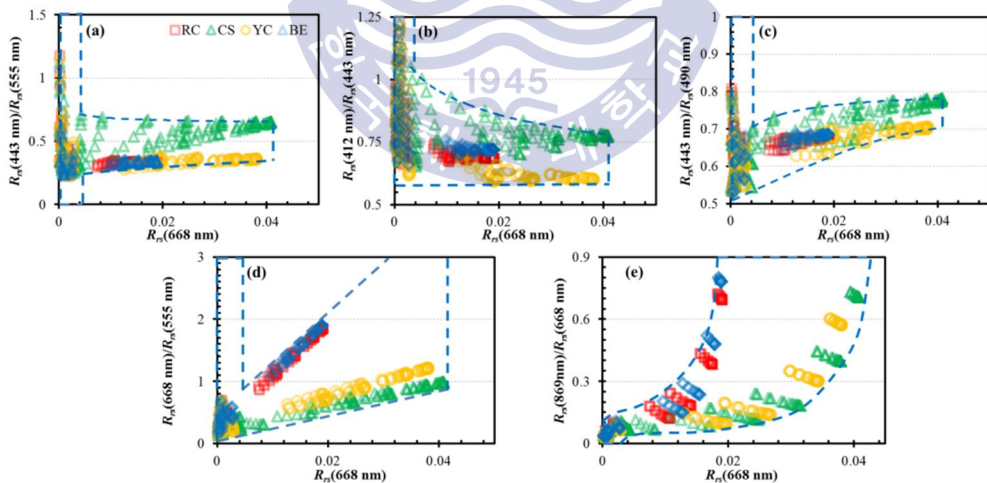


Fig. 34. R_{rs} spectral relationships obtained through HYDROLIGHT simulations (Ahn et al., 2015). For this simulation, the range of chl_a concentration varied from 0.1~30 mg m^{-3} , CDOM absorption at 440 nm from 0.1~0.3 m^{-1} , and suspended sediment concentration from 0.1~1000 g m^{-3} .

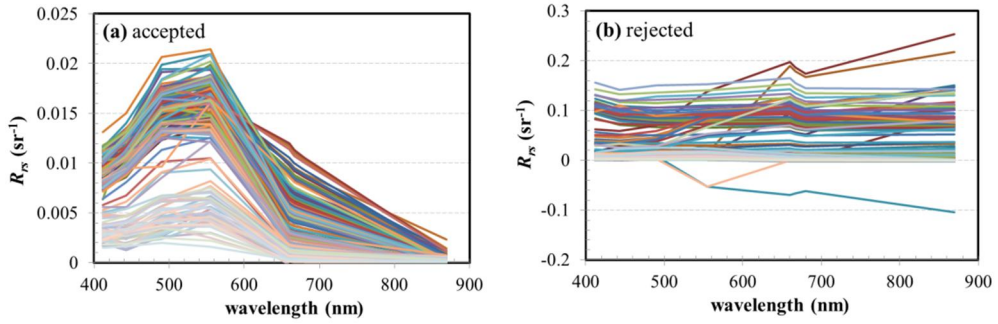


Fig. 35. Quality control adopted for the AERONET-OC data (Ahn et al., 2015). (a) R_{rs} spectra accepted by the quality control screening criteria, and (b) R_{rs} spectra rejected by the scheme because of spurious outliers.

4.2. Validation of SRAMS scheme with simulation data

Evaluation is analyzed by using the statistical indices such as the absolute percentage error (APE) (i.e. absolute percentage distribution: APD) and root mean square error (RMSE) defined as follows:

$$\text{APE} = \frac{100}{K} \sum_{n=1}^K \left(\frac{|V_T^n - V_E^n|}{V_T^n} \right), \quad (63)$$

$$\text{RMSE} = \sqrt{\frac{\sum_{n=1}^K (v_n^t - v_n^e)^2}{K}}, \quad (64)$$

where K is the total number of match-up pairs, and v_n^t and v_n^e are the true and derived values of n^{th} match-up entry, respectively.

Figure 36 (a) provides the errors in the retrieved aerosol reflectance $\Delta\rho_{am}$ for the simulation cases with comparing SSE scheme, and Figure 36 (b) is results of the SRAMS algorithm performance for entire atmospheric correction process with comparing SSE-based atmospheric correction.

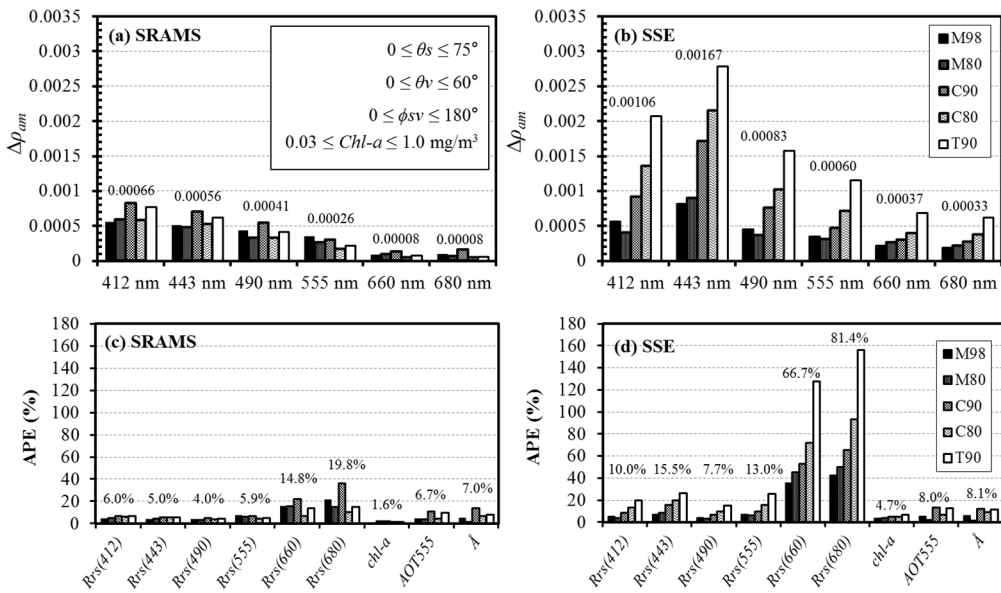


Fig. 36. Validation results from simulation data; the aerosol reflectance error $\Delta\rho_{am}$ for the SRAMS (a) and the SSE scheme (b), and errors in the ρ_{wn} , the chlorophyll-a (chl-a), aerosol optical thickness at 555 nm (AOT555), and the Ångström exponent for 443 nm relative to 865 nm (Å) in the absolute percentage deviation (APD) for the SRAMS (c) and the SSE scheme (d). (Ahn et al., 2016).

The errors in ρ_w are generally within the acceptable limits of 5.3 % APD from 412 to 555 nm. Although $\Delta\rho_{am}$ at red bands (660 and 680nm) are relatively small, the ρ_w errors at these bands are relatively significant due to relatively small ratio of water radiance to atmospheric radiance.

4.3. Assessment of the atmospheric correction improvements with *in situ* radiometric data

This section describes validation result of *in situ* match-ups for the previous (Ahn et al., 2012) and improved (this thesis) atmospheric correction using the GOCI data. To evaluate its performance with considering the bidirectional effects, the remote-sensing reflectance (R_{rs}) is used instead of the water-leaving reflectance (Wang, 2006; Morel et al., 2002; Morel et al., 2005).

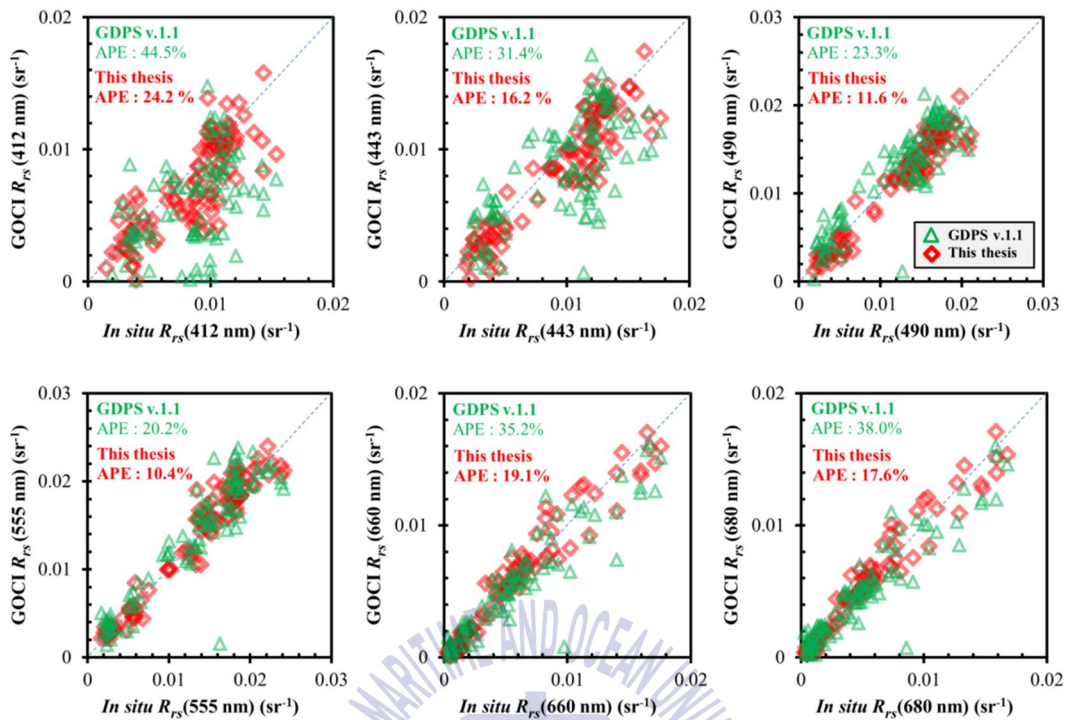


Fig. 37. Validation result of *in situ* R_{rs} match-ups for the previous (Ahn et al., 2012) and the improved (this thesis) atmospheric correction. *In situ* R_{rs} are collected from KOSC cruises for 2010–2016 and AERONET-OC sites.

As shown in Figure 37, the atmospheric correction process developed by this study retrieves R_{rs} with the mean APE values 26.9, 18.6, 13.5, 12.1, 21.9, and 22.9 % for 412, 443, 490, 555, 660, and 680 nm bands (total 19.3 %), respectively. The validation results of atmospheric correction associated with ship-measured R_{rs} and AERONET-OC R_{rs} are quantitatively summarized in Table 8.

Table 8. Statistics of R_{rs} match-ups for KOSC cruises and AERONET-OC

		$R_{rs}(412 \text{ nm})$	$R_{rs}(443 \text{ nm})$	$R_{rs}(490 \text{ nm})$	$R_{rs}(555 \text{ nm})$	$R_{rs}(660 \text{ nm})$	$R_{rs}(680 \text{ nm})$
APE (%)	Ahn et al. (2012)	44.45	31.42	23.29	20.24	35.18	38.02
	This thesis	24.18	16.24	11.59	10.41	19.10	17.59
Med. Error	Ahn et al. (2012)	29.77	25.28	14.56	14.11	20.00	19.08
	This thesis	16.16	13.65	7.06	6.74	14.46	12.14
R^2	Ahn et al. (2012)	0.1927	0.4909	0.7979	0.8525	0.8353	0.9191
	This thesis	0.6716	0.8566	0.9414	0.9488	0.9214	0.9166

Chapter 5. Discussions

5.1. Impacts of water vapor correction on ocean color products

As described in the chapter 2, water vapor absorption can significantly effect the GOCI observation in the red and the NIR bands (i.e., 660, 745, and 865 nm) because the absorption spectrum crosses the out-of-band spectral response, meanwhile, the absorption effect on GOCI bands that designed to avoid water vapor and oxygen absorption have not been considered. Therefore, a water vapor correction model is additionally applied to both the NIR vicarious calibration and the atmospheric correction scheme, and then compared its contribution regarding sensitivities on the GOCI level-2 products.

Three GOCI bands 660, 745, and 865 nm affected by water vapor absorption are used for the atmospheric correction. Two NIR bands 745 and 865 nm are used to know aerosol type and their concentration, and 660 nm band is used for the turbid water reflectance in NIR bands correction by the iterative scheme. This implies that this absorption can significantly effect on the aerosol model selection, aerosol load estimation, and contribution of turbid water reflectance in two NIR bands. Figure 38 is showing impact of water viper correction on the GOCI R_{rs} .

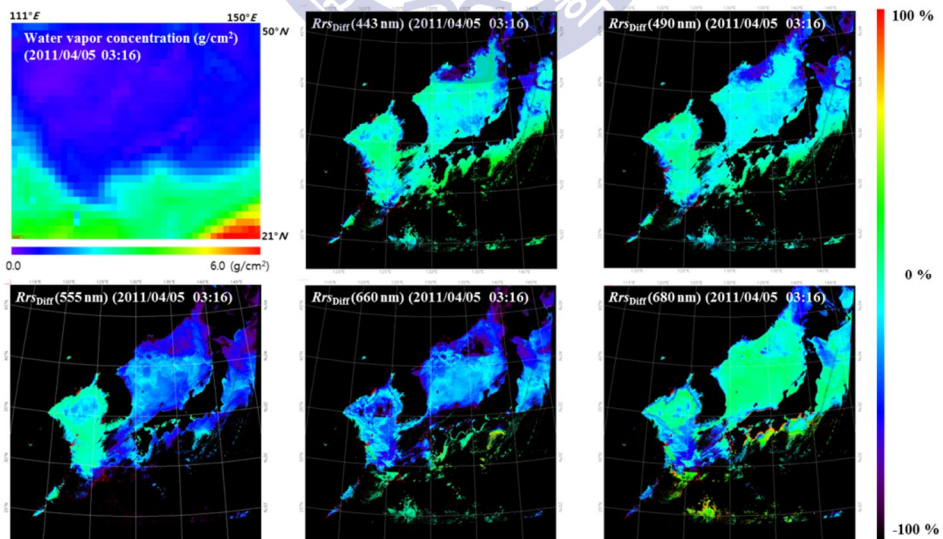


Fig. 38. Water vapor correction impacts on the GOCI R_{rs} in percentage difference.

As shown in Fig. 39, the water vapor absorption in the range of out of band responses can be change the R_{rs} results not only 660, 745, and 865 nm bands but also all other bands up to $\pm 70\%$.

The R_{rs} difference also effects to the chl_a products both blue and green band ratio algorithm and fluorescence line height (FLH) algorithm. Fluorescence chl_a algorithm is developed for CDOM-rich case-2 waters and uses 660, 680, and 745 nm that is directly affected by the water vapor absorption issue. Figure # is showing this water vapor impacts on the chl_a products with the band ratio technique (a) and the FLH technique. As shown in the result, water vapor effect can produce errors up to $\pm 50\%$ for band ratio technique and -50 to more than 200% for FLH technique.

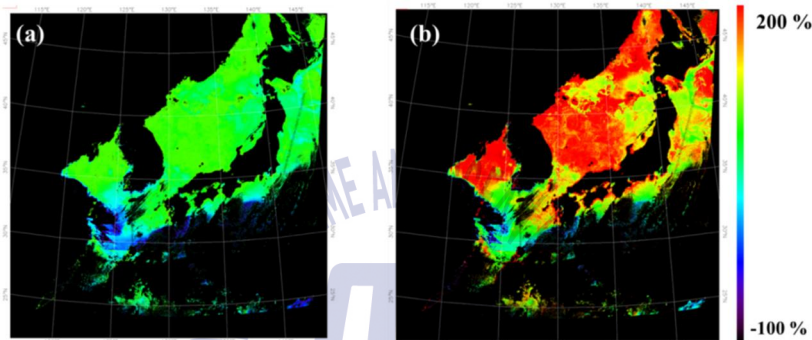


Fig. 39. Water vapor correction impacts on the GOCI chl_a in percentage difference. (a) Chl_a is derived by band ratio (blue/green) algorithm (O'Reilly et al., 1998). (b) Chl_a is derived by fluorescence line height algorithm (Gower, 1980; Gower and Borstad, 1981).

5.2. Stability for high solar and satellite zenith angle for diurnal observation

Estimation of ocean color products in the case of high solar zenith angle is an important issue for detecting diurnal variable of ocean environment. To achieve this, securing a diurnal stability of the atmospheric correction is required. However, there are various issue that producing uncertainties to remove the atmospheric effects, thus it is a major challenge for a geostationary ocean color mission. The issue is not practically a new problem. Other existing polar orbit sensors (e.g., SeaWiFS, MERIS, MODIS, and etc.) are already encountered by the high zenith angle issues in the polar oceans and at the scan edges. One of the major error source is the plane parallel assumption (PPA) on the implementation of radiative transfer simulation, in spite of atmospheric structure of earth is

spherical shell. In the case of solar zenith angle is 80%, errors from the PPA may produce errors up to ~2.5% on the Rayleigh scattering estimation at 865 nm (Ding and Gordon, 1994). This may impacts on the R_{rs} errors more than 25%. The secondary error source is extended atmospheric path that including inhomogeneous atmospheric constituent while the atmospheric correction assumes that the atmosphere is homogeneous in the upward and downward light paths. The extended atmospheric path also reduces the water radiance to atmospheric radiance ratio that makes the atmospheric correction more sensitive by any uncertainties. Moreover, this relatively enhanced atmospheric radiance will more produce bright pixel adjacency effect again. Accuracies on aerosol reflectance relationship polynomial models using the LUT-stored coefficients are also dropped for large zenith angles. This issue will be discussed on the section 5.4.

5.3. Cloud masking on fast-moving clouds and quality analysis

As described in Chapter 2 (section 2.2.2), each GOCI band is obtained in a different acquisition time by the time delaying during the filter wheel rotation. While the filter wheel is rotating, fast moving clouds or aerosol often makes mis-registered pixels that may produce significant errors regarding cloud masking or aerosol corrections (Fukushima et al., 2015; Robinson et al., 2016). This issue considerably impacts in cases of fast-moving cloud edges or spatially high frequent aerosols (Fig. 40 (a)). These fast-moving clouds significantly impacts on atmospheric correction (Fig. 40 (b)) and chl-a estimation (Fig. 40 (c))

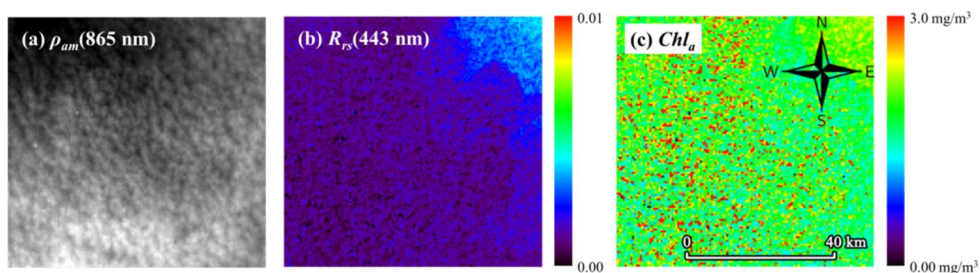


Fig. 40. (a) Aerosol reflectance at NIR used by atmospheric correction process. In the scene, aerosol pattern shows high spatial frequency and fast-moving in winter. (b) Atmospheric correction result over fast moving aerosols. R_{rs} at 443 nm shows spatially scattered values at fast-moving aerosol edge. (c) Significantly chl_a overestimated results represented as speckles due to erroneously produced R_{rs} .

The fast moving and spatially high frequent aerosols are mostly happens in winter season and the errors involved by the issue are often occurs on the observation of level-3 composition or trend of ocean color products.

5.4. Evaluation of the GOCI aerosol correction scheme compared with other approaches

The GOCI atmospheric correction uses a new aerosol correction scheme using the SRAMS. This approach is more direct and accurate in terms of optimization for determining the appropriate aerosol models from candidates. To evaluate the SRAMS-based method with comparing to other primary algorithms, various atmospheric correction algorithms are tested that officially employed by primary ocean color missions that are the SeaWiFS (Gordon and Wang, 1994), OCTS (Fukushima et al., 1998), and MERIS (Antoine and Morel, 1999). As summarized in Table 8, these three algorithms differ slightly in the process for the aerosol model selection and weight computation for retrieval of the aerosol optical properties in the visible bands, although no studies provided comparison results for these algorithms.

Table 9. Summary of primary schemes to correct aerosol reflectance with using 2 NIR bands for determining aerosol optical properties

Algorithms	SeaWiFS	OCTS	MERIS	GOCI
Aerosol model selection in single-/multiple-scattering space	single-scattering	single-scattering	Multiple-scattering	Multiple-scattering
Compute weight value for aerosol model interpolation	Comparing modeled epsilon to averaged epsilon from observation in NIR	Comparing modeled AOT to weight-averaged AOT from observation in NIR	Comparing modeled $\rho_{am}(NIR)$ to $\rho_{am}(NIR)$ from observation	Solving quadratic equation
Relationships used in the aerosol correction (polynomial degrees)	ρ_{am} and ρ_{as} (4 th order)	ρ_{am} and τ_a (3 rd order)	$(\rho_r + \rho_{am})/\rho_r$ and τ_a (2 nd order)	$\rho_{am}(\lambda_1)$ and $\rho_{am}(\lambda_2)$ (2 nd ~ 4 th order)

5.4.1. Aerosol correction approach for OCTS

The OCTS algorithm (Fukushima et al., 1998) uses the aerosol optical depth values ($\tau_a^{M_i}$) to

provide the epsilon values ($\varepsilon_{\tau_a}^{M_i}$) between two NIR bands,

$$\varepsilon_{\tau_a}^{M_i}(\lambda_1, \lambda_2) = \tau_a^{M_i}(\lambda_1) / \tau_a^{M_i}(\lambda_2), \quad (65)$$

where $\varepsilon_{\tau_a}^{M_i}(\lambda_1, \lambda_2)$ corresponds to the aerosol model M_i . The $\tau_a^{M_i}$ values are derived using look-up tables generated based on the 3rd order polynomial relationships between ρ_{am} and τ_a for a N number of aerosols.

$$\tau_a^{M_i}(\lambda) = \sum_{n=1}^3 c_n^{M2T}(M_i, \lambda, \theta_s, \theta_v, \phi_{sv}) \rho_{am}^{M_i}(\lambda)^n, \quad (66)$$

where c_n^{M2T} is the polynomial coefficient for the respective M_i , θ_s , θ_v , and ϕ_{sv} . Based on the derived $\varepsilon_{\tau_a}^{M_i}$ values, two optimum aerosol models (M_H and M_L) and the corresponding mixture ratios (w^{M_H}) are retrieved using a weighted-average ($\varepsilon_{\tau_a}^{ave}$) of $\varepsilon_{\tau_a}^{M_i}$ derived from

$$\varepsilon_{\tau_a}^{ave}(\lambda) = \frac{\sum_{i=1}^N w_i^{ave} \varepsilon_{\tau_a}^{M_i}(\text{NIR}_S, \text{NIR}_L)}{\sum_{i=1}^N w_i^{ave}}, \quad (67-1)$$

$$w_i^{ave}(\lambda) = \frac{1}{\left| \varepsilon_{\tau_a}^{M_i}(\text{NIR}_S, \text{NIR}_L) - \frac{K_{ext}^{M_i}(\text{NIR}_S)}{K_{ext}^{M_i}(\text{NIR}_L)} \right|}, \quad (67-2)$$

$$w^{M_H} = \frac{\varepsilon_{\tau_a}^{ave}(\lambda)(\text{NIR}_S, \text{NIR}_L) - \varepsilon_{\tau_a}^{M_L}(\text{NIR}_S, \text{NIR}_L)}{\varepsilon_{\tau_a}^{M_H}(\text{NIR}_S, \text{NIR}_L) - \varepsilon_{\tau_a}^{M_L}(\text{NIR}_S, \text{NIR}_L)}, \quad (68)$$

where $K_{ext}^{M_i}$ is the extinction coefficient that is proportional to $\tau_a^{M_i}$.

The aerosol multiple-scattering reflectances (ρ_{am}) for the VIS bands are then computed using two derived aerosol models (M_H and M_L). This is achieved through the inversion of Eq.(66),

$$\rho_{am}(\lambda) = w^{M_H} \sum_{n=1}^3 c_n^{T2M}(M_H, \lambda, \theta_s, \theta_v, \phi_{sv}) \tau_a^{M_H}(\lambda)^n + (1 - w^{M_H}) \sum_{n=1}^3 c_n^{T2M}(M_L, \lambda, \theta_s, \theta_v, \phi_{sv}) \tau_a^{M_L}(\lambda)^n, \quad (69)$$

where c_n^{T2M} is the polynomial coefficient for the respective M_i , θ_s , and θ_v . The OCTS algorithm

provides an estimate of ρ_{am} with an error of ± 0.002 which corresponds to $\pm 0.1 \mu\text{W}/\text{cm}^2/\text{nm}/\text{sr}$ in normalized water-leaving radiance at 443nm (Fukushima et al., 1998).

The OCTS atmospheric correction algorithm is summarized in Fig. 41.

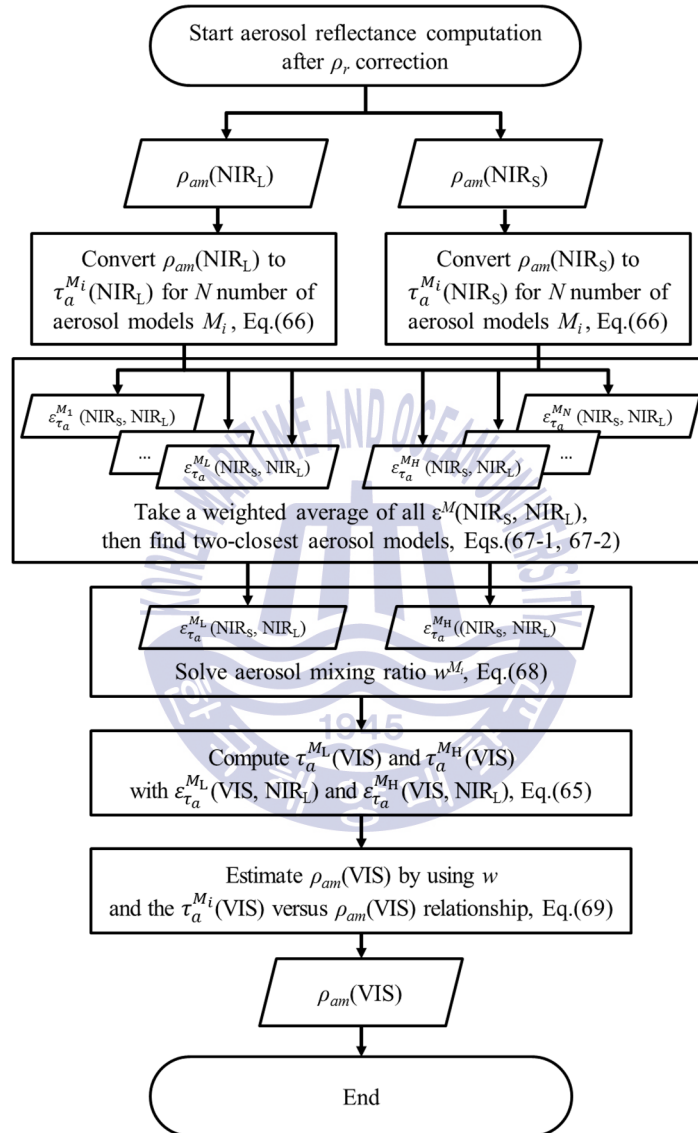


Fig. 41. Scheme of the $\rho_{am}(\text{VIS})$ estimation used by OCTS atmospheric correction (Fukushima et al., 1998). The method uses relationship between AOT and multiple-scattering aerosol reflectance to select optimum aerosol model.

5.4.2. Aerosol correction approach for MERIS

While the OCTS approach uses aerosol optical depth $\tau_a^{M_i}$ to derive the M_H , M_L , and w^{M_H} , the MERIS algorithm (Antoine and Morel, 1999; Antoine, 2010) retrieves these values from the multiple-scattering reflectance ratio (χ)

$$\chi(\lambda) = \frac{\rho_r(\lambda) + \rho_{am}(\lambda)}{\rho_r(\lambda)}, \quad (70)$$

using the second order polynomial relationships between χ and $\tau_a^{M_i}$ as given below

$$\tau_a^{M_i}(\lambda) = \sum_{n=1}^2 c_n^{G2T}(\lambda, M_i, \theta_s, \theta_v, \phi_{sv}) \chi(\lambda)^n, \quad (71-1)$$

$$\chi^{M_i}(\lambda) = \sum_{n=1}^2 h_n(\lambda, M_i, \theta_s, \theta_v, \phi_{sv}) \tau_a^{M_i}(\lambda)^n, \quad (71-2)$$

$$\tau_a^{M_i}(\lambda) = \tau_a^{M_i}(\text{NIR}_L) \frac{K_{ext}^{M_i}(\lambda)}{K_{ext}^{M_i}(\text{NIR}_L)}, \quad (71-3)$$

where c_n^{G2T} is the polynomial coefficient for the respective M_i , θ_s , θ_v , and ϕ_{sv} . The term χ^{M_i} is a theoretical χ value derived through radiative transfer simulations carried out for M_i , θ_s , θ_v , and ϕ_{sv} .

The two optimum aerosol models M_H and M_L are then selected by comparing the observed $\chi(\text{NIR}_S)$ to theoretical $\chi^{M_i}(\text{NIR}_S)$ values that satisfy the following condition,

$$\chi^{M_L}(\text{NIR}_S) < \chi(\text{NIR}_S) \leq \chi^{M_H}(\text{NIR}_S). \quad (72)$$

Then the mixing ratio w^{M_H} is approximately derived assuming that there exists a linear relationship between χ and $\tau_a^{M_i}$,

$$w^{M_H} = \frac{\chi(\text{NIR}_S) - \chi^{M_L}(\text{NIR}_S)}{\chi^{M_H}(\text{NIR}_S) - \chi^{M_L}(\text{NIR}_S)}. \quad (73)$$

In a similar way to Eq.(72), χ values for the VIS bands are computed through

$$\chi(\lambda) = w^{M_H} \sum_{n=1}^2 c_n^{T2G}(M_H, \lambda, \theta_s, \theta_v, \phi_{sv}) \tau_a^{M_H}(\lambda)^n + (1 - w^{M_H}) \sum_{n=1}^2 c_n^{T2G}(M_L, \lambda, \theta_s, \theta_v, \phi_{sv}) \tau_a^{M_L}(\lambda)^n, \quad (74)$$

where c_n^{T2G} is the polynomial coefficient for the respective M_i , θ_s , θ_v , and ϕ_{sv} .

This MERIS atmospheric correction algorithm is summarized in Fig. 42.

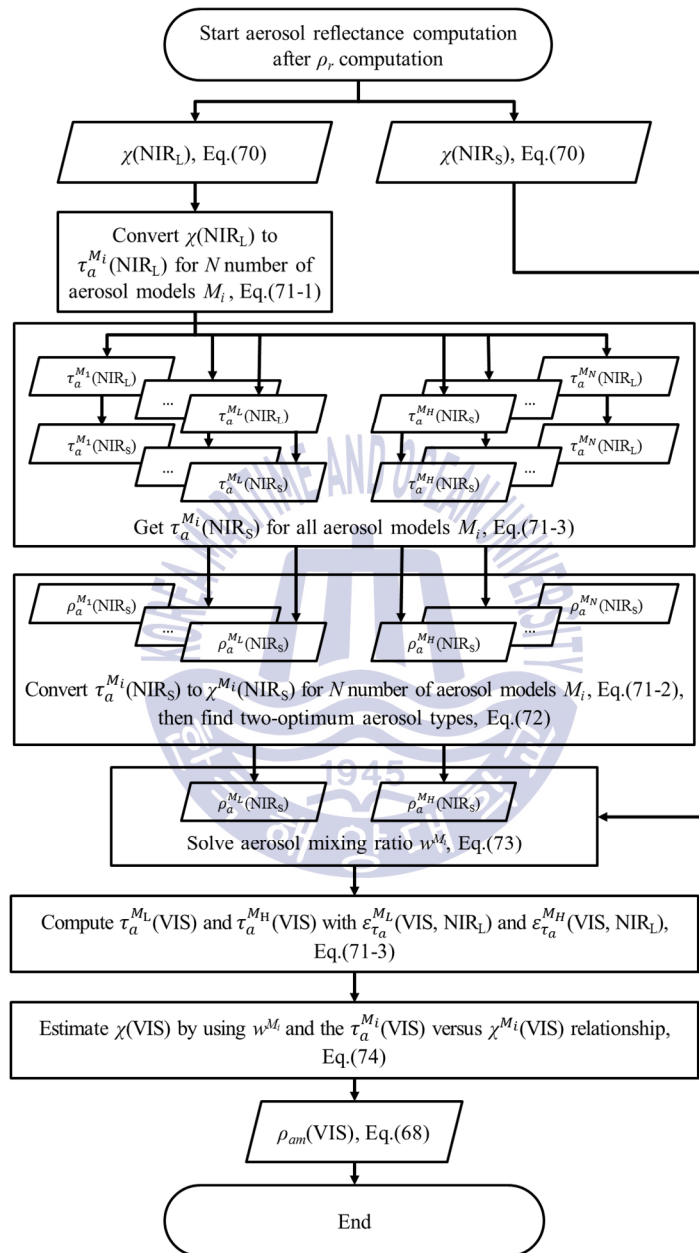


Fig. 42. Scheme of the $\rho_{am}(\text{VIS})$ estimation used by MERIS atmospheric correction (Antoine and Morel, 1999; Antoine, 2010).

5.4.3. Evaluation results

To evaluate a reliability of each aerosol reflectance estimation process, compared the accuracy of polynomial relationships were first compared that are 4th order polynomial relationship between ρ_{am} and ρ_{as} used for SeaWiFS, 3rd order polynomial relationship between ρ_{am} and τ_a used for OCTS, 2nd polynomial relationship between $(\rho_{am} + \rho_r) / \rho_r$ and τ_a used for MERIS, and 2nd, 3rd and 4th order polynomial relationship between $\rho_{am}(\lambda_1)$ and $\rho_{am}(\lambda_2)$ suggested in this study. The relationship agreements were compared by simulation for parameters described in previous chapter (i.e., $4 \times \theta_s$, $4 \times \theta_v$, $5 \times \phi_{sv}$). Figure 43 shows comparison results of ρ_{am} conversion error in % with given relationships of each method for 412, 443, 490, 555, 660, 680, 745, and 865 nm.

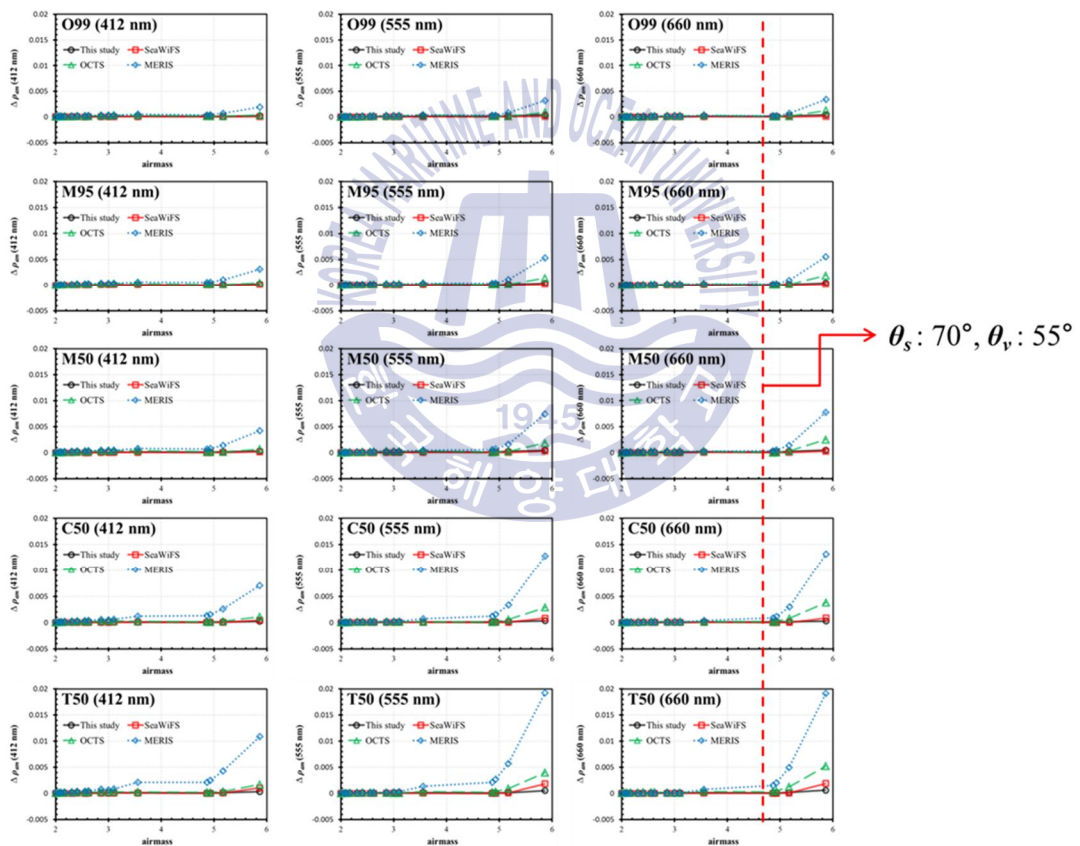


Fig. 43. Accuracy of relationships used for each $\rho_{am}(\text{VIS})$ estimation scheme for SeaWiFS, OCTS, MERIS and GOCI algorithms. For moderate solar/sensor zenith angles, errors during the aerosol reflectance estimation is less than 0.003

As shown in Fig. 43, the 2nd order polynomial relationship between the multiple-scattering reflectance and aerosol optical thickness resulted worse accuracy especially for large zenith angle geometries and fine-size aerosols (i.e., large air-mass cases and tropospheric aerosol type, respectively).

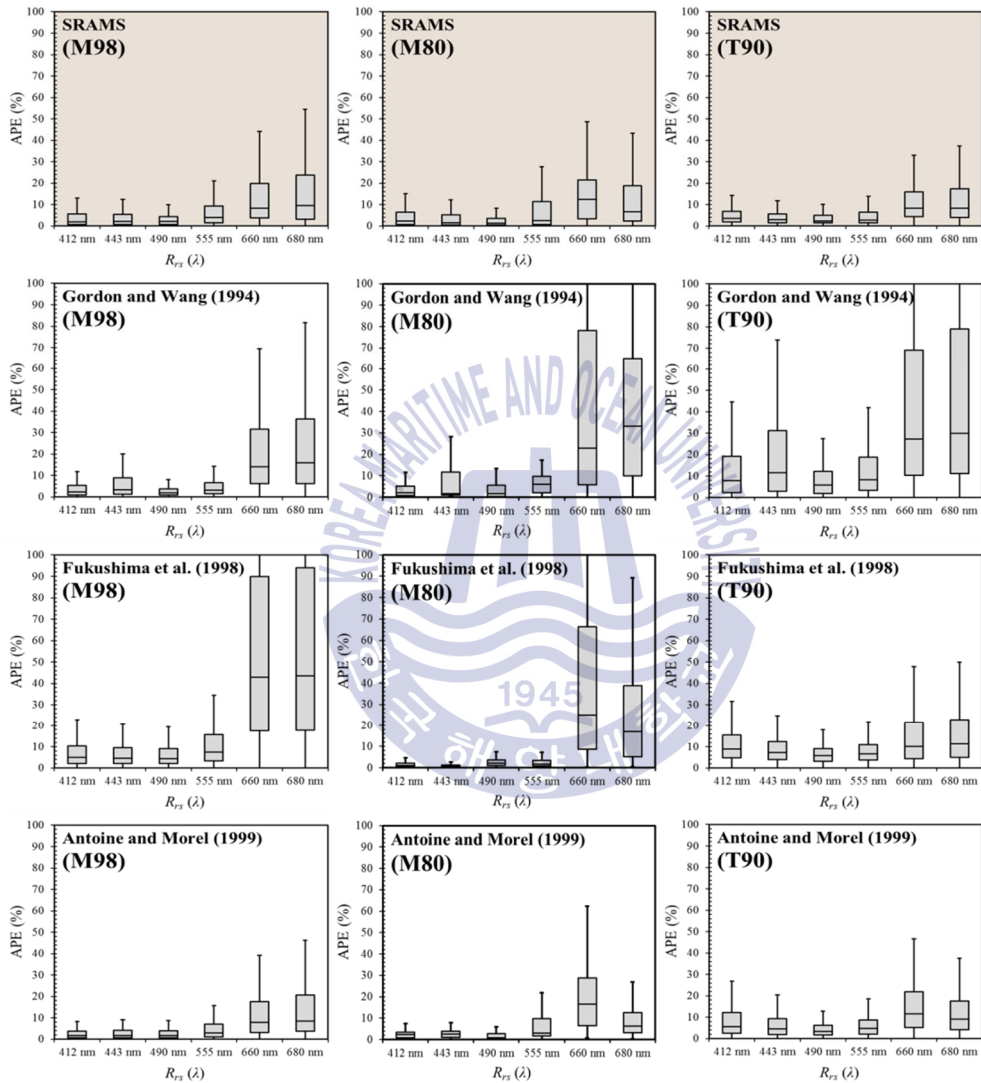


Fig. 44. Comparison result of the SRAMS scheme with other three major methods by the radiative transfer simulations. The assessment is performed for not only candidate aerosol models but also different aerosol models. Two of the most accurate schemes are the MERIS approach and the SRAMS-based method which select aerosol models in multiple-scattering domain.

The efficiency of the SRAMS scheme with other three existing methods is assessed using simulations carried out for the 9 aerosol models: M90, M70, C90, C80, and T90 are candidate models, and M98, M80, C70, T80 are not candidates, and observation geometries: $\theta_s = 0^\circ, 25^\circ, 50^\circ,$ and 75° , $\theta_v = 0^\circ, 20^\circ, 40^\circ,$ and 60° , and $\phi = 0^\circ, 45^\circ, 90^\circ, 135^\circ,$ and 180° .

Figure 44 provides the error in the R_{rs} and chl_a retrieval. These results are truly remarkable, as the relative errors in R_{rs} (412 ~ 680 nm) for the present algorithm are stable across the entire aerosol models and sufficiently small (5-10%) in comparison with other methods. Especially for fine-size aerosol types (coastal and tropospheric) which the multiple-scattering effect is relatively stronger, the accuracy of the SRAMS-based method is outstanding within 10% of errors in red bands while errors in the red bands from other algorithms is exceeding 10~60%. This implies that the errors in atmospheric correction with multiple scattering effects are seen to contribute significantly to the error in R_{rs} . This suggests that accurate results can be obtained with the new algorithm as long as the candidate aerosol models are representative in size and composition of the aerosols actually present over the ocean (they need not be precisely same). It can be remarkable, however, pigment (chl_a) retrieval performance of SeaWiFS algorithm showed the best accuracy due to similar behavior of errors between blue and green bands although its aerosol correction performance needs to be improved.

5.5. Pitfalls in estimation of aerosol reflectance using 2-NIR bands

Aerosol estimation methods using 2-NIR bands sometimes mistakenly carry out aerosol multiple-scattering reflectance in VIS bands due to a discrepancy of optical properties between candidate aerosol models and actual aerosols (e.g., absorbing aerosols), errors from meteorological data as atmospheric correction inputs, considerable contributions of turbid water reflectance in NIR, and the last NIR band (i.e., 865 nm for GOCI) calibration error.

Candidate aerosol models for the atmospheric correction are generally established with assumption of non- or less-absorbing aerosol (Gordon et al., 1997; Yan et al., 2002; Stamnes et al., 2003; Toratani et al., 2007). However, aerosols in GOCI observation area are often affected by

absorbing aerosols originated by biomass burning or mineral dust (Kim et al., 2004; Kim et al., 2005; Lee et al., 2005, 2007, 2010). To overcome this, further spectral information such as UV band (e.g., 380 nm band) or hyperspectral or polarization information are needed (Toratani et al., 2007; Chowdhary et al., 2005; Yang et al., 2010).

Initial atmospheric correction algorithms had not significantly considered whitecap reflectance error estimated by using wind speed meteorological data. Because whitecap has spectrally flat reflectance and treated and removed as maritime aerosols during the atmospheric correction. Afterward, it is revealed that the spectral slope of whitecap reflectance in NIR can be significant (Frouin et al., 1996), and this indicates inaccuracy whitecap estimation would cause failure on aerosol model determination. The GDPS is currently using reanalysis meteorological data distributed by National Centers for Environmental Prediction (NCEP) with 1° spatial and 6 hours temporal resolution that are significantly lower resolution compare to the GOCI data. Therefore, employing higher-resolution reanalysis data such as data distributed by European Centre for Medium-Range Weather Forecasts (ECMWF) should be applied to the GOCI atmospheric correction.

Traditional vicarious calibration approaches including GOCI's method assumes the last NIR calibration band is already calibrated (Gordon, 1998; Eplee et al., 2001; Wang and Gordon, 2002; Murakami et al., 2005; Lerebourg et al., 2011; Werdell et al., 2007; Franz et al., 2007; Wang et al., 2013a; Wang et al., 2013b, Ahn et al., 2015), and then inter calibrate only the second last NIR band for the NIR calibration. Error from the last NIR band calibration gain can erroneously effect to aerosol reflectance estimation in VIS bands because aerosol type and concentration are determined by two NIR bands (Wang et al., 2015). Further effort such as using optimization techniques to calibrate the last NIR band is required for the future work.

5.6. Issues in the vicarious calibration of GOCI VIS and NIR bands

For the first step of the GOCI vicarious calibration, 2-NIR bands are inter-calibrated by assumption of aerosol optical properties in open ocean far from continent are constantly

identical to maritime aerosols. Figure is analysis results for 745 nm calibration gain sensitivity to calibration site. As shown in the figure 45, derived calibration gains at the furthestmost site (site 3) has the least scattered result. In this analysis, 745 nm gain tends to be smaller as a site gets closer to the land.

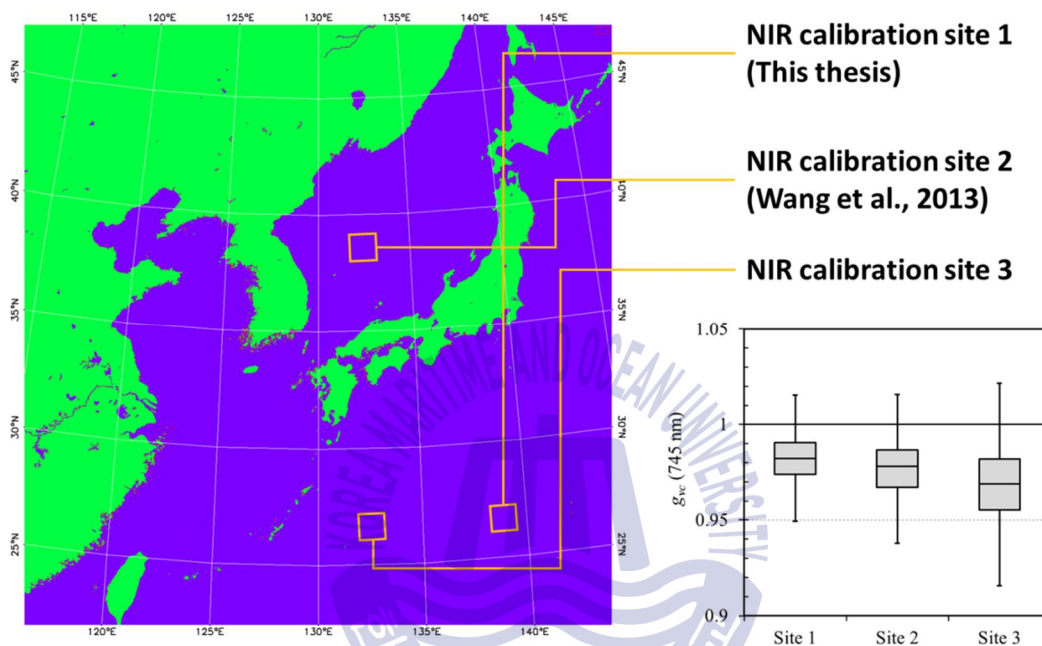


Fig. 45. Analysis results for 745 nm calibration gain sensitivity to calibration site. Furthestmost site (site 3) has the least scattered result.

However, further aerosol trajectory investigation has shown that the NIR vicarious calibration site can be affected by continent aerosols as shown in Fig. 46 (Stein et al., 2015). Moreover, continent aerosols further effect to the NIR calibration site in winter due to a seasonal wind heading from the Northeast Asia to the calibration site (Lau and Li, 1984). To avoid continent aerosols for NIR inter-calibration, observation data have to be selected by aerosol's trajectory statistics.

NOAA HYSPLIT MODEL
 Backward trajectories ending at 0800 UTC 01 Jan 16
 GDAS Meteorological Data

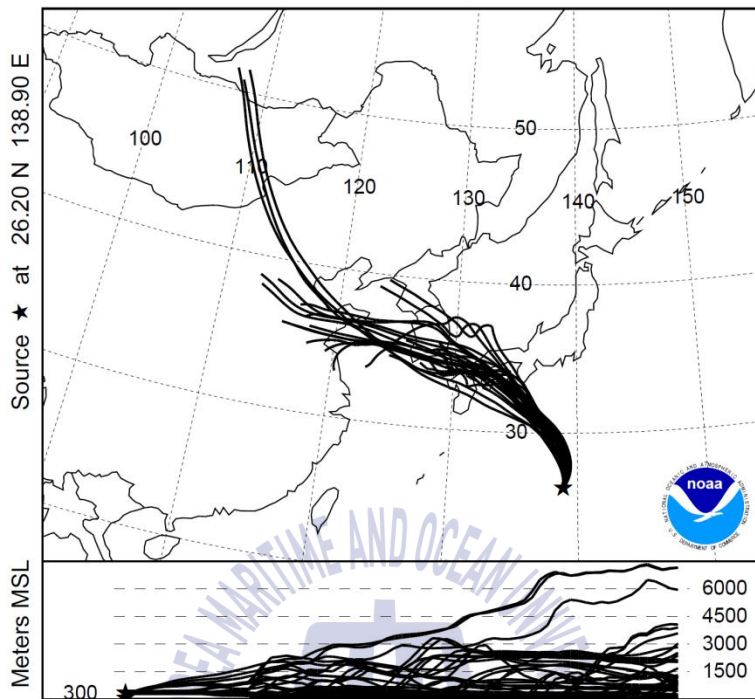


Fig. 46. The result of NOAA HYSPLIT model (Stein et al., 2015) to trace one-week backward aerosol trajectories of GOCI NIR calibration site (at 300 and 1500 m altitude) in winter (26th/Dec./2015 ~ 1st/Jan./2016). This result indicates that the NIR calibration site may be affected by continent aerosols.

In situ radiometric data used for VIS bands calibration has considerable uncertainty involved by above-water radiometry although those data once quality controlled. In the radiometry, sky radiance reflected at air-sea interface is first removed by the Mobley's model, however residual error can be fluctuated by wind-driven sea surface roughness, inhomogeneous sky radiance distribution, micro bubbles, ship rolling, and etc. This residual error can be significant in case of clear waters due to relatively strong reflected sky radiance to the water-leaving radiance. Moreover, this error is more significant in longer wavelengths (i.e., red bands) that is emerging weaker water signals caused by stronger water absorption in this band. Uncertainties from *in situ*

radiometry may cause inaccurate TOA radiance computations, thus further assured *in situ* radiometry such as underwater profiling or sky-blocked above water measurement (Lee et al., 2010) should be adopted.

5.7. Uncertainties from the bidirectional effect correction method

The in-water bidirectional effect correction model of GOCI atmospheric correction relating the f/Q is developed by Morel's biogenic optical model, and this model sometimes causes inaccurate R_{rs} retrieval in turbid waters that water spectrum is dominated by optical properties of inorganic particles (Park and Ruddick, 2005; Lee et al., 2011). IOP-based bidirectional effect correction models has developed previously (Park and Ruddick, 2005; Lee et al., 2011), however, further investigation is still required for practical application due to hardness of these models validation.

Bidirectional effect correction model for air-sea interface upward transmittance (Wang, 2006) developed without considering sky radiance angular distribution change by aerosols. However, aerosols type and concentration also effect to the sky radiance angular distribution (Harrison and Coombes, 1988), and that implies sea-surface Fresnel transmittance can be affected by aerosols especially for longer wavelengths and large solar zenith angles that aerosols radiance is relatively stronger to Rayleigh radiance. GOCI atmospheric correction is requiring further bidirectional effect correction accuracy to observe diurnal variables in ocean environment, thus the correction model for air-sea interface have to be integrated with radiative transfer within aerosols.

Chapter 6. Conclusion

This thesis has described the atmospheric correction algorithm for the GOCI Data Processing System and its improvements (Table 10). The early GOCI atmospheric correction implemented in GDPS ver. 1.1 is based on SeaWiFS method because the SeaWiFS algorithm has been used most widely and GOCI has a similar spectral band design with the SeaWiFS band. Since GDPS version 1.1, the GOCI atmospheric correction has been updated to reduce the uncertainties involved by aerosol model selection, considerable turbid water radiance in NIR bands, gaseous absorptions with considering GOCI out-of-band responses. The vicarious calibration has been applied additionally to reduce discrepancy between the radiative transfer system used for GOCI atmospheric correction and the observation.

In the general atmospheric correction algorithms including the GOCI algorithm, the Rayleigh reflectance can be predicted within 1% of error by a radiative transfer simulation, because temporal and spatial variation of air molecules is changing in a small and expectable range. However, computation of aerosol reflectance takes the most difficult part due to the considerable variations of aerosol type and concentration in space and time. For the aerosol reflectance correction, GOCI first adopted the SeaWiFS method that is using two NIR bands based on the BPA to obtain aerosol's optical information. SeaWiFS and previous GOCI atmospheric correction has used the single-scattering reflectance ratio called as single-scattering epsilon (ϵ) to select the two-most appropriate aerosol models with their mixing factor. In the process, two closest aerosol models and their weighting factor for the mixture are determined by comparison of $\epsilon(\text{NIR}_s, \text{NIR}_L)$ average for all candidate aerosol models. This method has an issue that the aerosol model selection result has dependency on all candidate aerosol models which induce residual errors. To overcome this, the GOCI aerosol correction scheme uses the spectral relationships of aerosol multiple-scattering reflectance (and is named as SRAMS). It uses second-order polynomial relationship on aerosol multiple-scattering reflectance between two NIR then directly solves two most appropriate aerosol models and their weighting factor with no residual error.

Table 10. Summary of the GOCI atmospheric correction algorithm developed for GDPS version 1.1 and 1.5

	Algorithm in GDPS ver. 1.1	This thesis in GDPS ver. 1.5
Correction of O ₃ absorption	Quasi-analytic model (Gordon et al., 1983)	Quasi-analytic model (Gordon et al., 1983)
Correction of H ₂ O absorption	Omitted	Empirical Model derived from RT simulation result
Gravity correction for Rayleigh optical thickness	Omitted	Rayleigh optical thickness correction model (Bodhain et al., 1999)
Sun-glint correction	Omitted	Wind field dependent model (Cox and Munk, 1954)
Aerosol correction method	Using SSE (Gordon and Wang, 1994; Wang and Gordon, 1994)	Using SRAMS (Ahn et al., 2016)
Turbid water NIR correction model	4 th order spectral relationship of water reflectance between 660 and 745 nm, and linear relationship between 745 and 865 nm (Ahn et al., 2012)	4 th order polynomial relationship between $\rho_{wn}(660 \text{ nm})$ and $\rho_{wn}(745 \text{ nm})$, and 2 nd order polynomial relationship between $\rho_{wn}(745 \text{ nm})$ and $\rho_{wn}(865 \text{ nm})$
White-cap correction	Wind speed dependent model (Gordon and Wang, 1994)	Wind speed dependent model (Stramska and Petelski, 2003)
Diffuse transmittance	Quasi-analytic model with assuming isotropic water reflectance (Gordon et al., 1983)	Empirical model based on RT simulation with considering anisotropic water reflectance (Wang, 1999; Antoine 2010)
Bidirectional effect correction	Omitted	In-water bidirectional effect correction model (Morel and Gentili, 2002; Morel et al, 2005), and air-sea interface bidirectional effect correction model (Franz et al., 2003; Wang, 2006)
Vicarious calibration	Omitted	NIR band calibration with pre-assumed aerosol model (M80), and VIS band calibration with calibrated NIR band and <i>in situ</i> water radiance (Franz et al., 2007; Ahn et al., 2015).

The GOCI observation area includes highly turbid waters, and those turbid water spectra are generally dominated by suspended inorganic particles that have strong backscattering coefficient. This strong backscattering involves considerable water-leaving radiance in NIR that mistakenly pretend to aerosol radiance in the aerosol correction process, then causes underestimation of water-leaving radiance in the VIS bands. The GOCI atmospheric correction uses a iterative turbid water NIR radiance correction approach. A spectral relationship of water reflectance between red and two

NIR bands based on the similarity of turbid water spectrum shape while SeaWiFS algorithm considers in water biogenic optical properties.

The vicarious calibration to enhance both the calibration accuracy and agreement between radiative transfer system employed by the GOCI atmospheric correction and the actual observation has increased accuracy in computation of water-leaving radiance (or R_{rs}). The calibration process adopts two main steps as the traditional vicarious calibration methods, *i.e.*, calibration of the NIR bands with an assumed aerosol type, and calibration of the VIS bands using nL_w measurements. For calibration of the NIR bands, the longest NIR band (865 nm) was assumed to be absolutely calibrated, which formed the basis for calibration of the shorter NIR band at 745 nm. The vicarious calibration of the NIR bands was performed with assuming the constant the maritime aerosol type with relative humidity 80% at the calibration site. To achieve this, an open-ocean site in the southeast region of the GOCI observation area far from the continent was selected to assume that all aerosols are free from continent. The estimated TOA radiance at 745 nm was computed using a radiative transfer model with the given aerosol type to obtain the statistical mean of the ratio estimated TOA radiance to estimated TOA radiance at 745 nm, which determines the vicarious gain at 745 nm. It can be assumed that calibrated NIR bands will result the accurate atmospheric path radiance in VIS bands. Thus, TOA radiance in VIS bands can be estimated with water-leaving radiance from *in situ* measurements and atmospheric path radiance from two-calibrated NIR bands, then the VIS bands are calibrated by comparing estimated TOA radiance and observed TOA radiance in VIS bands.

The overall atmospheric correction algorithm is evaluated in two ways, one is validation with *in situ* data after the vicarious calibration, the other is comparison the GOCI atmospheric correction result with other primary atmospheric correction algorithms' results by the radiative transfer simulations. Results from the match-up comparison between *in situ* and GOCI-derived R_{rs} measurements show that the GOCI atmospheric correction algorithm reasonably works in both case-1 and case-2 waters. This implies that the correction for NIR water reflectance and the vicarious calibration works correctly.

There remain a few issues concerning the atmospheric correction and its vicarious calibration.

First issue is discrepancy of optical properties between candidate aerosol models and real aerosols. Candidate aerosol models adopted by general atmospheric correction processes are developed by assumption of non- or less-absorbing aerosols. However, aerosols from continent sometimes include strong-absorbing constituents such as black carbon or mineral dust. Currently, there is no complete way to deal with absorbing aerosols in GOCI bands, because absorbing aerosol effect in NIR bands is relatively weak compare to other aerosol optical properties. Therefore, additional optical observation such as UV bands or polarimetric information will be required in future missions (Toratani et al., 2007). Secondly, the NIR correction scheme of the atmospheric correction for turbid waters, the relationship between the red-NIR water reflectance is variable, depending on the absorption of suspended particles, chl_a , CDOM, moreover vicarious gains. Also, the ocean reflectance at 660 nm wavelength can be saturated for extremely turbid cases like the estuary of the Yangtze River which would cause an increasing error in estimation the NIR reflectance from 660nm. Other NIR bands around 709nm (Moore et al., 1999) or shortwave infrared (SWIR) bands (Wang, 2007) are useful for atmospheric correction in turbid waters, however there is no such NIR or SWIR bands in GOCI sensor, unfortunately. Therefore, further investigates to understand cause of changing relationships regarding inherent optical properties of in-water constituents are required. For the NIR vicarious calibration issue thirdly, the dominant aerosols at the calibration sites were derived from mainly maritime processes, and the relative humidity that determined the aerosol optical properties varied from 55 to 95%. For observation, the aerosol type is assumed to be maritime with relative humidity 80% model for the expectation that the spectral slope in NIR would approximately fall in this range. However, some recent revised study has shown this area can be also affected by aerosols originated from continent. Thus, removal of observation data by using trajectory model is required for the future work. The visible band calibration has used *in situ* nL_w measurements recorded by an above-water radiometry. Although these measurements has been quality controlled, uncertainties can be still significant, because the nL_w is relatively weak compared with the sky radiance reflected at the air-sea surface for clear waters. In particular, the uncertainty is more prominent as the wavelength increases from red and NIR where water absorption is strong and reflectance is weak. Those *in situ* measurement uncertainties can cause erroneous computation of

TOA radiance in VIS bands for the vicarious calibration. Further quality assured *in situ* radiometry such as in-water profiling or sky-blocked above water measurement are required for the next step. Lastly, the bidirectional effect correction scheme (f/Q) which accounts for radiant-path geometry dependencies in the nL_w and the R_{rs} due to the anisotropy of the near-surface light field (Morel et al., 2005) is based on a biogenic optical model that does not fully consider case-2 waters. Since the near-surface light field depends on the absorption and scattering properties of the water column and its constituents, it is essential to consider a more appropriate model (Park and Ruddick, 2005; Lee et al., 2011) for case-2 waters. It is expected to implement these schemes in the GOCI data processing system in future work.



Appendix. Glossary of symbols

- ◆ λ : wavelength
- ◆ θ_s : solar zenith angle
- ◆ θ_v : viewing (satellite) zenith angle
- ◆ ϕ_{s-v} : Azimuth angle difference between the sun and the sensor at the position
- ◆ $0+$: just above the water
- ◆ $0-$: just beneath the water
- ◆ Ed : downward irradiance
- ◆ Eu : upward irradiance
- ◆ chl_a : chlorophyll-a
- ◆ L_{TOA} : top-of-atmosphere radiance observed by satellite
- ◆ L_{TOA}^{VC} : simulated top-of-atmosphere radiance for the vicarious calibration
- ◆ L_w^{VC} : water-leaving radiance for the vicarious calibration
- ◆ L_{TOA}^{cor} : top-of-atmosphere radiance after the correction of white cap and gaseous absorption
- ◆ $L_a(\lambda)$: multiple scattering radiance by aerosols in the absence of air molecules
- ◆ $L_{ra}(\lambda)$: radiance by light interaction between air molecules and aerosols
- ◆ L_r : multiple scattering radiance by air molecules (Rayleigh scattering) in the absence of aerosols
- ◆ L_{wc} : whitecap radiance
- ◆ L_w : water-leaving radiance
- ◆ nL_w : normalized water-leaving radiance
- ◆ L_{sea}^{0+} : total above water radiance leaving the water surface with including sea-surface reflected sky radiance
- ◆ L_{sky} : Sky radiance at the surface
- ◆ $L_b(\lambda)$: the residual radiance from light reflected by the ship's superstructure, microfoam, or

fluctuated $f_{surf} \times L_{sky}$

- ◆ R_b : L_b/Ed
- ◆ R_{rs} : remote-sensing reflectance
- ◆ R_{rs}^m : remote sensing reflectance before the bidirectional effect correction
- ◆ ρ_{TOA} : top-of-atmosphere reflectance
- ◆ ρ_w : water reflectance (reflectance at the top-of-atmosphere)
- ◆ ρ_{wn} : normalized water reflectance (reflectance at the surface)
- ◆ ρ_{wc} : whitecap reflectance
- ◆ ρ_r : multiple scattering reflectance by air molecules (Rayleigh scattering) in the absence of aerosols
- ◆ ρ_r^{latm} : preliminary computed Rayleigh scattering reflectance for 1 atmospheric pressure
- ◆ ρ_a : multiple scattering reflectance by aerosols in the absence of air molecules
- ◆ ρ_{ra} : reflectance by light interaction between air molecules and aerosols
- ◆ ρ_{as} : aerosol single-scattering reflectance
- ◆ ρ_{am} : $\rho_a + \rho_{ra}$
- ◆ ρ_{am}^{Mod} : theoretically computed $\rho_{am}(\lambda)$ for specific aerosol model
- ◆ ρ_{am}^{VC} : simulated $\rho_{am}(\lambda)$ for the vicarious calibration
- ◆ ρ_g : sun-glint reflectance that is spectrally independent
- ◆ r_{rs}^{model} : the remote-sensing reflectance just below the surface
- ◆ b_b : total backscattering coefficient
- ◆ a : total absorption coefficient
- ◆ \mathfrak{R} : Fresnel transmittance at the air-sea interface
- ◆ f : ratio of underwater IOP term to under water reflectance
- ◆ Q : underwater bidirectional effect term
- ◆ c_{BF} : bidirectional effect coefficient (i.e., $\mathfrak{R} \cdot f / Q$)
- ◆ ε : aerosol single-scattering reflectance ratio (i.e., single-scattering epsilon, SSE)
- ◆ ε^{pre} : theoretical SSE value

- ◆ ε^{ave} : averaged ε for candidate aerosol models
- ◆ td^s : total downward diffuse transmittances including both the aerosols and the air molecules
- ◆ td^v : total upward diffuse transmittances including both the aerosols and the air molecules
- ◆ td_r^s : downward diffuse transmittance by air molecules
- ◆ td_r^v : upward diffuse transmittance by air molecules from the sea surface to the sensor
- ◆ tg^s : total downward direct transmittances including both the aerosols and the air molecules
- ◆ tg^v : total upward direct transmittances including both the aerosols and the air molecules
- ◆ t_{oz}^s : downward gaseous transmittance by ozone from the sun to the sea surface
- ◆ t_{oz}^v : upward gaseous transmittance from the sea surface to the sensor
- ◆ t_{wv}^s : downward gaseous transmittance by water vapor from the sun to the sea surface
- ◆ t_{wv}^v : upward gaseous transmittance by water vapor from the sun to the sea surface
- ◆ tdm^s : downward diffuse transmittance model established with assuming that the single scattering albedo multiply forward scattering probability is 0.95 for i^{th} aerosol models
- ◆ tdm^v : upward diffuse transmittance model established with assuming that the single scattering albedo multiply forward scattering probability is 0.95 for i^{th} aerosol models
- ◆ $t_{wv} : t_{wv}^s \times t_{wv}^v$
- ◆ τ_r : Rayleigh optical thickness
- ◆ $\eta(\lambda)$: forward scattering probability of aerosols
- ◆ F_0 : the extraterrestrial solar irradiance with considering sun-earth distance
- ◆ f_0 : extraterrestrial solar irradiance without considering sun-earth distance
- ◆ c_{we} : spectral correction function (Frouin et al., 1996) for whitecap reflectance
- ◆ ws : wind speed at the sea level in m/s
- ◆ wv : water vapor concentration in g/cm²
- ◆ c_{s-e} : sun-earth distance coefficient
- ◆ c_p : the air pressure in mb
- ◆ d_y : day of year
- ◆ M_i : i^{th} aerosol model
- ◆ w^{M_i} : weighting factor of M_i for aerosol reflectance fraction

- ◆ g_{vc} : vicarious gain
- ◆ f_{surf} : air-sea Fresnel reflectance ratio



Acknowledgements

박사과정을 마무리 하는 시점에서 지난 3 년간의 박사과정을 다시 뒤돌아보면 새삼스럽게 많은 아쉬움이 남지만, 많은 분들의 도움과 따뜻한 관심 속에서의 질책들은 저를 또 다시 한 층 성숙해질 수 있는 계기를 마련해주었던 것 같습니다. 본 과정을 통하여 박사는 연구 자체를 수행할 능력뿐 아니라 연구를 처음부터 끝까지 혼자 힘으로 기획하고 관리하며 이를 다른 사람에게 설득할 수 있는 능력 또한 갖추어야 함을 알게 되었습니다. 이와 관련해서는 저 스스로가 부족함을 여러모로 많이 느끼지만 박사학위 취득을 시작으로 이런 부족한 부분들을 최대한 보충하도록 노력해야 할 것 같습니다. 많은 우여곡절 끝에 박사학위과정을 마치며, 많은 도움을 주신 분들께 이렇게 지면으로나마 감사의 인사를 남길 수 있어서 정말 다행인 것 같습니다.

우선 지도교수이자 선배연구자로서 한없이 부족한 저를 올바르게 이끌어 주시고, 지금의 논문이 있기까지 학문적으로 인간적으로 아낌없는 가르침을 주신 박영제 지도교수님께 진심으로 감사 드립니다. 또, 연구 내용뿐 아니라 박사학위를 가지고 연구에 임하는 자세에 대해서도 정말 많은 조언을 해주신 한국해양과학기술원 김원국 박사님께도 감사의 말씀을 드립니다. 언제나 저를 따뜻하게 맞아주시고 제 연구분야가 어떻게 활용되고 확장되는지 전체적인 큰 그림을 볼 수 있도록 도와주신 한국해양과학기술원 노재훈 박사님께도 감사 드립니다. 또, 저를 항상 믿어주시고 응원해주셨던 한국해양과학기술원 조성익 해양위성센터장님께도 진심으로 감사 드립니다. 바쁜 일정 속에서도 실질적으로 연구진행에 많은 도움을 주시고 시간을 할애해주셨던 이보람 연구원님을 비롯한 해양위성센터 연구팀 분들께도 감사 드리며, 함께 학위과정을 거치며 서로 많은 조언과 응원을 주고받은 대학원 동기들에게도 감사의 마음을 전하고 싶습니다. 덧붙여서 멀리 떨어져 제 연구분야 선배로써 조언뿐 아니라 많은 인간적인 격려와 응원을 해주셨던 Tokai 대학 Hajime Fukushima 교수님께도 이 기회를 통해 감사의 뜻을 전해야 할 것 같습니다. 선배 연구자일 뿐 아니라 인생의 선배로써도 항상 관심 가져주시고 격려해주신 NOAA 의 손승현 박사님께도 감사 드리며, 제 연구에 저 스스로가 어느 정도 자신감을 가질 수 있도록

많은 도움을 주신 NASA 의 Bryan Franz, JAXA 의 Hiroshi Murakami, NOAA 의 Menghua Wang 박사님, Tokai 대학의 Mitsuhiro Toratani 교수님께도 멀리서나마 감사의 말씀을 전해드려야 할 것 같습니다.

마지막으로 항상 저를 믿고 응원해주며 마음 한구석에 언제나 든든하게 자리잡고 있는 아내 수빈이와 존재 그 자체 만으로도 응원이 되는 딸 서윤이, 뒤늦은 나이에 학문에 뛰어들었음에도 불구하고 한결같이 사랑과 믿음으로 지켜봐 주시며 지원해주신 사랑하는 부모님들께 진심으로 감사 드리며 이 논문을 바칩니다.



References

- Ahmad Z., and Franz B., 2014, Atmospheric correction using multiple-scattering epsilon values. *in proceeding of Ocean Optics XXII.*
- Ahmad Z., and Franz B., 2016, Recent enhancements in atmospheric correction algorithm for ocean color retrievals from remotely sensed data. *in proceeding of Ocean Optics XXIII.*
- Ahn, J.H., Park, Y.J., Ryu, J.H. and Lee, B., 2012. Development of atmospheric correction algorithm for Geostationary Ocean Color Imager (GOCI). *Ocean Science Journal*, 47(3), pp.247-259.
- Ahn, J.H., Park, Y.J., Kim, W. and Lee, B., 2015. Vicarious calibration of the Geostationary Ocean Color Imager. *Optics express*, 23(18), pp.23236-23258.
- Ahn, J. H., Park, Y. J., Kim, W., & Lee, B. (2016). Simple aerosol correction technique based on the spectral relationships of the aerosol multiple-scattering reflectances for atmospheric correction over the oceans. *Optics Express*, 24(26), 29659-29669..
- Ahn, Y.H., 1990. Optical properties of biogenous and mineral particles present in the ocean. Application: inversion of reflectance. *Paris-VI university.(61) Maritime Atmospheres," Limnology and Oceanography*, 35(8), pp.1657-1675.
- André, J.M. and Morel, A., 1989. Simulated effects of barometric pressure and ozone content upon the estimate of marine phytoplankton from space. *Journal of Geophysical Research: Oceans*, 94(C1), pp.1029-1037.
- Antoine, D. and Morel, A., 1999. A multiple scattering algorithm for atmospheric correction of remotely sensed ocean colour (MERIS instrument): principle and implementation for atmospheres carrying various aerosols including absorbing ones. *International Journal of Remote Sensing*, 20(9), pp.1875-1916.

- Antoine, D., 2010. Atmospheric corrections over Case 1 waters (CWAC). *OLCI Level 2 ATBD*, v.2.2. S3-L2-SD-03-C07-LOV-ATBD.
- Bailey, S. W., Franz, B. A., & Werdell, P. J. (2010). Estimation of near-infrared water-leaving reflectance for satellite ocean color data processing. *Optics Express*, 18(7), 7521-7527.
- Blanchard, D.C., 1971. Whitecaps at sea. *Journal of the Atmospheric Sciences*, 28(4), pp.645-645.
- Bodhaine, B.A., Wood, N.B., Dutton, E.G. and Slusser, J.R., 1999. On Rayleigh optical depth calculations. *Journal of Atmospheric and Oceanic Technology*, 16(11), pp.1854-1861.
- Bowers, D.G., Boudjelas, S. and Harker, G.E.L., 1998. The distribution of fine suspended sediments in the surface waters of the Irish Sea and its relation to tidal stirring. *International Journal of Remote Sensing*, 19(14), pp.2789-2805.
- Clark, D.K., Gordon, H.R., Voss, K.J., Ge, Y., Broenkow, W. and Trees, C., 1997. Validation of atmospheric correction over the oceans. *J. Geophys. Res*, 102(17), pp.209-17.
- Cho, S., Ahn, Y.H., Han, H.J. and Ryu, J.H., 2009, August. Prelaunch characterization of the geostationary ocean color imager. In *SPIE Optical Engineering+ Applications* (pp. 74590I-74590I). International Society for Optics and Photonics.
- Clark, D.K., Gordon, H.R., Voss, K.J., Ge, Y., Broenkow, W. and Trees, C., 1997. Validation of atmospheric correction over the oceans. *J. Geophys. Res*, 102(17), pp.209-17.
- Chowdhary, J., Cairns, B., Mishchenko, M.I., Hobbs, P.V., Cota, G.F., Redemann, J., Rutledge, K., Holben, B.N. and Russell, E., 2005. Retrieval of aerosol scattering and absorption properties from photopolarimetric observations over the ocean during the CLAMS experiment. *Journal of the Atmospheric Sciences*, 62(4), pp.1093-1117.
- Cox, C. and Munk, W., 1954. Measurement of the roughness of the sea surface from photographs of the sun's glitter. *JOSA*, 44(11), pp.838-850.
- Ding, K., and Gordon, H. R. (1994). Atmospheric correction of ocean-color sensors: effects of the Earth's curvature. *Applied Optics*, 33(30), 7096-7106.

- Doron, Maéva, et al. "Spectral variations in the near-infrared ocean reflectance." *Remote Sensing of Environment* 115.7 (2011): 1617-1631.
- Doxaran, D., Froidefond, J.M., Lavender, S. and Castaing, P., 2002. Spectral signature of highly turbid waters: Application with SPOT data to quantify suspended particulate matter concentrations. *Remote sensing of Environment*, 81(1), pp.149-161.
- Eplee, R.E., Robinson, W.D., Bailey, S.W., Clark, D.K., Werdell, P.J., Wang, M., Barnes, R.A. and McClain, C.R., 2001. Calibration of SeaWiFS. II. Vicarious techniques. *Applied Optics*, 40(36), pp.6701-6718.
- Faure, F., Coste, P. and Kang, G., 2008, October. The GOCI instrument on COMS mission-The first geostationary ocean color imager. In *Proceedings of the International Conference on Space Optics (ICSO)* (pp. 14-17).
- Franz, B. A., Eplee, R. E., Bailey, S. W., & Wang, M. (2003). Changes to the atmospheric correction algorithm and retrieval of oceanic optical properties. *NASA Tech. Mem.* 2003-206892, 22.
- Franz, B.A., Bailey, S.W., Werdell, P.J. and McClain, C.R., 2007. Sensor-independent approach to the vicarious calibration of satellite ocean color radiometry. *Applied Optics*, 46(22), pp.5068-5082.
- Frouin, R., Schwindling, M. and Deschamps, P.Y., 1996. Spectral reflectance of sea foam in the visible and near-infrared: In situ measurements and remote sensing implications. *Journal of Geophysical Research: Oceans*, 101(C6), pp.14361-14371.
- Fukushima, H., Higurashi, A., Mitomi, Y., Nakajima, T., Noguchi, T., Tanaka, T. and Toratani, M., 1998. Correction of atmospheric effect on ADEOS/OCTS ocean color data: Algorithm description and evaluation of its performance. *Journal of Oceanography*, 54(5), pp.417-430.
- Fukushima, H., Toratani, M., Ahn, J.H, Kim, W. and Park Y., 2015. Cloud-Affected Pixel Identification on COMS/GOCI Ocean Color Imagery in Consideration to Fast-moving Cloud Fragments. In *Proceedings of the International Symposium on Remote Sensing (ISRS)*, Tainan, April 22–24.

- Gordon, H.R., 1978. Removal of atmospheric effects from satellite imagery of the oceans. *Applied Optics*, 17(10), pp.1631-1636.
- Gordon, H.R., Clark, D.K., Mueller, J.L. and Hovis, W.A., 1980. Phytoplankton pigments from the Nimbus-7 Coastal Zone Color Scanner: comparisons with surface measurements. *Science*, 210(4465), pp.63-66.
- Gordon, H.R., Clark, D.K., Brown, J.W., Brown, O.B., Evans, R.H. and Broenkow, W.W., 1983. Phytoplankton pigment concentrations in the Middle Atlantic Bight: comparison of ship determinations and CZCS estimates. *Applied optics*, 22(1), pp.20-36.
- Gordon, H.R., Brown, J.W. and Evans, R.H., 1988. Exact Rayleigh scattering calculations for use with the Nimbus-7 coastal zone color scanner. *Applied optics*, 27(5), pp.862-871.
- Gordon, H.R. and Wang, M., 1992. Surface-roughness considerations for atmospheric correction of ocean color sensors. 1: The Rayleigh-scattering component. *Applied optics*, 31(21), pp.4247-4260.
- Gordon, H.R. and Wang, M., 1994. Retrieval of water-leaving radiance and aerosol optical thickness over the oceans with SeaWiFS: a preliminary algorithm. *Applied optics*, 33(3), pp.443-452.
- Gordon, H.R., Du, T. and Zhang, T., 1997. Remote sensing of ocean color and aerosol properties: resolving the issue of aerosol absorption. *Applied Optics*, 36(33), pp.8670-8684.
- Gordon, H.R., 1998. In-orbit calibration strategy for ocean color sensors. *Remote sensing of Environment*, 63(3), pp.265-278.
- Gower, J. F. R. "Observations of in situ fluorescence of chlorophyll-a in Saanich Inlet." *Boundary-Layer Meteorology* 18, no. 3 (1980): 235-245.
- Gower, J. F. R., and G. Borstad. "Use of the in vivo fluorescence line at 685 nm for remote sensing surveys of surface chlorophyll a." In *Oceanography from space*, pp. 329-338. Springer US, 1981.
- Goyens, C., Jamet, C. and Ruddick, K.G., 2013a. Spectral relationships for atmospheric correction. I. Validation of red and near infra-red marine reflectance relationships. *Optics express*, 21(18), pp.21162-21175.

- Goyens, C., Jamet, C. and Ruddick, K.G., 2013b. Spectral relationships for atmospheric correction. II. Improving NASA's standard and MUMM near infra-red modeling schemes. *Optics express*, 21(18), pp.21176-21187.
- Harrison, A.W. and Coombes, C.A., 1988. Angular distribution of clear sky short wavelength radiance. *Solar Energy*, 40(1), pp.57-63.
- Hu, C., Carder, K.L. and Muller-Karger, F.E., 2000. Atmospheric correction of SeaWiFS imagery over turbid coastal waters: a practical method. *Remote sensing of Environment*, 74(2), pp.195-206.
- Hu, C., Feng, L. and Lee, Z., 2012. Evaluation of GOCI sensitivity for at-sensor radiance and GDPS-retrieved chlorophyll-a products. *Ocean Science Journal*, 47(3), pp.279-285.
- Jiang, L., & Wang, M. (2014). Improved near-infrared ocean reflectance correction algorithm for satellite ocean color data processing. *Optics express*, 22(18), 21657-21678.
- Joo, H., Son, S., Park, J.W., Kang, J.J., Jeong, J.Y., Lee, C.I., Kang, C.K. and Lee, S.H., 2015. Long-Term Pattern of Primary Productivity in the East/Japan Sea Based on Ocean Color Data Derived from MODIS-Aqua. *Remote Sensing*, 8(1), p.25.
- Kang, G., Coste, P., Youn, H., Faure, F. and Choi, S., 2010. An in-orbit radiometric calibration method of the geostationary ocean color imager. *IEEE Transactions on Geoscience and Remote Sensing*, 48(12), pp.4322-4328.
- Kim, D.H., Sohn, B.J., Nakajima, T., Takamura, T., Takemura, T., Choi, B.C. and Yoon, S.C., 2004. Aerosol optical properties over East Asia determined from ground-based sky radiation measurements. *Journal of Geophysical Research: Atmospheres*, 109(D2).
- Kim, S.W., Yoon, S.C., Jefferson, A., Ogren, J.A., Dutton, E.G., Won, J.G., Ghim, Y.S., Lee, B.I. and Han, J.S., 2005. Aerosol optical, chemical and physical properties at Gosan, Korea during Asian dust and pollution episodes in 2001. *Atmospheric Environment*, 39(1), pp.39-50.

- Kim, W., Ahn, J.H. and Park, Y.J., 2015. Correction of Stray-Light-Driven Interslot Radiometric Discrepancy (ISRDR) Present in Radiometric Products of Geostationary Ocean Color Imager (GOCI). *Geoscience and Remote Sensing, IEEE Transactions on*, 53(10), pp.5458-5472.
- Kim, W., Moon, J.E., Park, Y.J., Salisbury, J. and Mannino, A., 2016. Preliminary Result of the Korea-US Joint Field Campaign for Ocean Color (KORUS-OC, 2016). *International GOCI Symposium 2016*, pp.76.
- Kou, L., Labrie, D. and Chylek, P., 1993. Refractive indices of water and ice in the 0.65-to 2.5- μm spectral range. *Applied Optics*, 32(19), pp.3531-3540.
- Lau, K.M. and Li, M.T., 1984. The monsoon of East Asia and its global associations-A survey. *Bulletin of the American Meteorological Society*, 65(2), pp.114-125.
- Lee, K.H., Kim, J.E., Kim, Y.J., Kim, J. and von Hoyningen-Huene, W., 2005. Impact of the smoke aerosol from Russian forest fires on the atmospheric environment over Korea during May 2003. *Atmospheric Environment*, 39(1), pp.85-99.
- Lee, K.H., Li, Z., Wong, M.S., Xin, J., Wang, Y., Hao, W.M. and Zhao, F., 2007. Aerosol single scattering albedo estimated across China from a combination of ground and satellite measurements. *Journal of Geophysical Research: Atmospheres*, 112(D22).
- Lee, K.H. and Kim, Y.J., 2010. Satellite remote sensing of Asian aerosols: a case study of clean, polluted, and Asian dust storm days. *Atmos Meas Tech*, 3, pp.1771-1784.
- Lee, Z., Lubac, B., Werdell, J. and Arnone, R., 2009. An update of the quasi-analytical algorithm (QAA_v5). *International Ocean Color Group Software Report*.
- Lee, Z., Ahn, Y.H., Mobley, C. and Arnone, R., 2010. Removal of surface-reflected light for the measurement of remote-sensing reflectance from an above-surface platform. *Optics Express*, 18(25), pp.26313-26324.

- Lee, Z.P., Du, K., Voss, K.J., Zibordi, G., Lubac, B., Arnone, R. and Weidemann, A., 2011. An inherent-optical-property-centered approach to correct the angular effects in water-leaving radiance. *Applied Optics*, 50(19), pp.3155-3167.
- Lerebourg, C., Mazeran, C., Huot, J. and Antoine, D., 2011. Vicarious adjustment of the MERIS ocean colour radiometry. *ESA/MERIS Algorithm Theoretical Basis Document*, 2.
- Jiang, L. and Wang, M., 2014. Improved near-infrared ocean reflectance correction algorithm for satellite ocean color data processing. *Optics express*, 22(18), pp.21657-21678.
- Loisel, H. and Morel, A., 1998. Light scattering and chlorophyll concentration in case 1 waters: A reexamination. *Limnology and Oceanography*, 43(5), pp.847-858.
- Mannino, A., 2015. Ocean Color Science Working Group Highlights.
- McClatchey, R. A., Fenn, R. W., Selby, J. A., Volz, F. E., & Garing, J. S. (1972). *Optical properties of the atmosphere* (No. AFCRL-72-0497). AIR FORCE CAMBRIDGE RESEARCH LABS HANSCOM AFB MA.
- Mobley, C.D., 1999. Estimation of the remote-sensing reflectance from above-surface measurements. *Applied Optics*, 38(36), pp.7442-7455.
- Mobley, C.D. and Sundman, L.K., 2008. Hydrolight 5 Ecolight 5 technical documentation. *Sequoia Scientific, Incorporated, Bellevue, WA, 98005*, p.95.
- Mobley, C., Boss, E. and Roesler, C., 2010. Ocean optics web book.
- Moon, J.E., Park, Y.J., Ryu, J.H., Choi, J.K., Ahn, J.H., Min, J.E., Son, Y.B., Lee, S.J., Han, H.J. and Ahn, Y.H., 2012. Initial validation of GOCI water products against in situ data collected around Korean peninsula for 2010–2011. *Ocean Science Journal*, 47(3), pp.261-277.
- Moore, G.F., Aiken, J. and Lavender, S.J., 1999. The atmospheric correction of water colour and the quantitative retrieval of suspended particulate matter in Case II waters: application to MERIS. *International Journal of Remote Sensing*, 20(9), pp.1713-1733.

- Morel, A. and Prieur, L., 1977. Analysis of variations in ocean color. *Limnology and oceanography*, 22(4), pp.709-722.
- Morel, A., 1988. Optical modeling of the upper ocean in relation to its biogenous matter content(case I waters). *Journal of Geophysical Research*, 93(10), pp.749-10.
- Morel, A. and Maritorena, S., 2001. Bio-optical properties of oceanic waters- A reappraisal. *Journal of Geophysical research*, 106(C4), pp.7163-7180.
- Morel, A., Antoine, D. and Gentili, B., 2002. Bidirectional reflectance of oceanic waters: accounting for Raman emission and varying particle scattering phase function. *Applied Optics*, 41(30), pp.6289-6306.
- Morel A., Gentili B., and Antoine D., 2005. Assessing the Atmospheric and Marine Signal from a Geostationary Orbit (part II). *COMS Ocean Data Processing System Development Project (3)*
- Mueller, J.L., Davis, C., Arnone, R., Frouin, R., Carder, K., Lee, Z.P., Steward, R.G., Hooker, S., Mobley, C.D. and McLean, S., 2000. Above-water radiance and remote sensing reflectance measurements and analysis protocols. *Ocean Optics protocols for satellite ocean color sensor validation Revision*, 2, pp.98-107.
- Murakami, H., Yoshida, M., Tanaka, K., Fukushima, H., Toratani, M., Tanaka, A. and Senga, Y., 2005. Vicarious calibration of ADEOS-2 GLI visible to shortwave infrared bands using global datasets. *Geoscience and Remote Sensing, IEEE Transactions on*, 43(7), pp.1571-1584.
- Neukermans, G., Ruddick, K., Bernard, E., Ramon, D., Nechad, B. and Deschamps, P.Y., 2009. Mapping total suspended matter from geostationary satellites: a feasibility study with SEVIRI in the Southern North Sea. *Optics Express*, 17(16), pp.14029-14052.
- O'Reilly, John E., Stephane Maritorena, B. Greg Mitchell, David A. Siegel, Kendall L. Carder, Sara A. Garver, Mati Kahru, and Charles McClain. "Ocean color chlorophyll algorithms for SeaWiFS." *Journal of Geophysical Research: Oceans* 103, no. C11 (1998): 24937-24953.

- Park, Y.J. and Ruddick, K., 2005. Model of remote-sensing reflectance including bidirectional effects for case 1 and case 2 waters. *Applied Optics*, 44(7), pp.1236-1249.
- Pope, R.M. and Fry, E.S., 1997. Absorption spectrum (380–700 nm) of pure water. II. Integrating cavity measurements. *Applied optics*, 36(33), pp.8710-8723.
- Robinson, W.D., Franz, B.A., Mannino, A. and Ahn, J.H., 2016. Cloud motion in the GOCI/COMS ocean colour data. *International Journal of Remote Sensing*, 37(20), pp.4948-4963.
- Ruddick, K.G., Ovidio, F. and Rijkeboer, M., 2000. Atmospheric correction of SeaWiFS imagery for turbid coastal and inland waters. *Applied optics*, 39(6), pp.897-912.
- Ruddick, K., De Cauwer, V., Park, Y.J. and Moore, G., 2006. Seaborne measurements of near infrared water-leaving reflectance: The similarity spectrum for turbid waters.
- Ruddick, K., Nechad, B., Neukermans, G., Park, Y., Doxaran, D., Sirjacobs, D. and Beckers, J.M., 2008, October. Remote sensing of suspended particulate matter in turbid waters: State of the art and future perspectives. In *Proceedings of the Ocean Optics XIX conference, Barga* (pp. 6-10).
- Ryu, J.H. and Ishizaka, J., 2012. GOCI data processing and ocean applications. *Ocean Science Journal*, 47(3), pp.221-221.
- Ryu, J.H., Han, H.J., Cho, S., Park, Y.J. and Ahn, Y.H., 2012. Overview of geostationary ocean color imager (GOCI) and GOCI data processing system (GDPS). *Ocean Science Journal*, 47(3), pp.223-233.
- Salisbury, J., 2016. The Korea-US Ocean Color Cruise (KORUS-OC) in support of the GOCI and GEO-CAPE Ocean Color Missions. *International GOCI Symposium 2016*, pp.75.
- Siegel, D.A., Wang, M., Maritorena, S. and Robinson, W., 2000. Atmospheric correction of satellite ocean color imagery: the black pixel assumption. *Applied optics*, 39(21), pp.3582-3591.
- Shettle, E.P. and Fenn, R.W., 1979. *Models for the aerosols of the lower atmosphere and the effects of humidity variations on their optical properties* (No. AFGL-TR-79-0214). AIR FORCE GEOPHYSICS LAB HANSCOM AFB MA.

- Shi, W. and Wang, M., 2009. An assessment of the black ocean pixel assumption for MODIS SWIR bands. *Remote Sensing of Environment*, 113(8), pp.1587-1597.
- Shim, J.S., Chun, I.S. and Min, I.K., 2004, January. Construction of Ieodo Ocean Research Station and its Operation. In *The Fourteenth International Offshore and Polar Engineering Conference*. International Society of Offshore and Polar Engineers.
- Smith, R.C. and Baker, K.S., 1981. Optical properties of the clearest natural waters (200–800 nm). *Applied optics*, 20(2), pp.177-184.
- Stamnes, K., Yan, B., Li, W., Stamnes, J.J. and Tsay, S.C., 2003. Pitfalls in atmospheric correction of ocean color imagery: how should aerosol optical properties be computed?: reply to comment. *Applied optics*, 42(3), pp.545-549.
- Stein, A.F., Draxler, R.R., Rolph, G.D., Stunder, B.J.B., Cohen, M.D. and Ngan, F., 2015. NOAA's HYSPLIT atmospheric transport and dispersion modeling system. *Bulletin of the American Meteorological Society*, 96(12), pp.2059-2077.
- Stramska, M. and Petelski, T., 2003. Observations of oceanic whitecaps in the north polar waters of the Atlantic. *Journal of Geophysical Research: Oceans*, 108(C3).
- Stumpf, R.P., Arnone, R.A., Gould, R.W., Martinolich, P.M. and Ransibrahmanakul, V., 2003. A partially coupled ocean-atmosphere model for retrieval of water-leaving radiance from SeaWiFS in coastal waters. *NASA Tech. Memo*, 206892, pp.51-59.
- Toratani, M., Fukushima, H., Murakami, H. and Tanaka, A., 2007. Atmospheric correction scheme for GLI with absorptive aerosol correction. *Journal of oceanography*, 63(3), pp.525-532.
- Vermote, E., Tanré, D., Deuzé, J.L., Herman, M., Morcrette, J.J. and Kotchenova, S.Y., 2006. Second simulation of a satellite signal in the solar spectrum-vector (6SV). *6S User Guide Version*, 3, pp.1-55.
- Wang, M., 1991. Atmospheric correction of the second generation ocean color sensors(Ph. D. Thesis).

- Wang, M. and Gordon, H.R., 1994. A simple, moderately accurate, atmospheric correction algorithm for SeaWiFS. *Remote Sensing of Environment*, 50(3), pp.231-239.
- Wang, M., 1999. Atmospheric correction of ocean color sensors: computing atmospheric diffuse transmittance. *Applied optics*, 38(3), pp.451-455.
- Wang, M. and Bailey, S.W., 2001. Correction of sun glint contamination on the SeaWiFS ocean and atmosphere products. *Applied Optics*, 40(27), pp.4790-4798.
- Wang, M., 2002. The Rayleigh lookup tables for the SeaWiFS data processing: Accounting for the effects of ocean surface roughness. *International Journal of Remote Sensing*, 23(13), pp.2693-2702.
- Wang, M. and Gordon, H.R., 2002. Calibration of ocean color scanners: how much error is acceptable in the near infrared?. *Remote Sensing of Environment*, 82(2), pp.497-504.
- Wang, M., 2003. An efficient method for multiple radiative transfer computations and the lookup table generation. *Journal of Quantitative Spectroscopy and Radiative Transfer*, 78(3), pp.471-480.
- Wang, M., 2005. A refinement for the Rayleigh radiance computation with variation of the atmospheric pressure. *International journal of remote sensing*, 26(24), pp.5651-5663.
- Wang, M., 2006. Effects of ocean surface reflectance variation with solar elevation on normalized water-leaving radiance. *Applied optics*, 45(17), pp.4122-4128.
- Wang, M. and Shi, W., 2006. Cloud masking for ocean color data processing in the coastal regions. *IEEE Transactions on Geoscience and Remote Sensing*, 44(11), pp.3196-3105.
- Wang, M. and Shi, W., 2007. The NIR-SWIR combined atmospheric correction approach for MODIS ocean color data processing. *Optics Express*, 15(24), pp.15722-15733.
- Wang, M., 2010. Atmospheric correction for remotely-sensed ocean-colour products. *Reports and Monographs of the International Ocean-Colour Coordinating Group (IOCCG)*.

- Wang, M., Shi, W. and Jiang, L., 2012. Atmospheric correction using near-infrared bands for satellite ocean color data processing in the turbid western Pacific region. *Optics Express*, 20(2), pp.741-753.
- Wang, M., Ahn, J.H., Jiang, L., Shi, W., Son, S., Park, Y.J. and Ryu, J.H., 2013a. Ocean color products from the Korean Geostationary Ocean Color Imager (GOCI). *Optics express*, 21(3), pp.3835-3849.
- Wang, M., Liu, X., Tan, L., Jiang, L., Son, S., Shi, W., Rausch, K. and Voss, K., 2013b. Impacts of VIIRS SDR performance on ocean color products. *Journal of Geophysical Research: Atmospheres*, 118(18).
- Wang, Menghua, et al. "Technique for monitoring performance of VIIRS reflective solar bands for ocean color data processing." *Optics express* 23.11 (2015): 14446-14460.
- Wang, M., 2016. Rayleigh radiance computations for satellite remote sensing: accounting for the effect of sensor spectral response function. *Optics Express*, 24(11), pp.12414-12429.
- Werdell, P.J., Bailey, S.W., Franz, B.A., Morel, A. and McClain, C.R., 2007. On-orbit vicarious calibration of ocean color sensors using an ocean surface reflectance model. *Applied optics*, 46(23), pp.5649-5666.
- Yan, B., Stamnes, K., Li, W., Chen, B., Stamnes, J.J. and Tsay, S.C., 2002. Pitfalls in atmospheric correction of ocean color imagery: how should aerosol optical properties be computed?. *Applied optics*, 41(3), pp.412-423.
- Yang, H., & Gordon, H. R. (1997). Remote sensing of ocean color: assessment of water-leaving radiance bidirectional effects on atmospheric diffuse transmittance. *Applied Optics*, 36(30), 7887-7897.
- Yang, K., Liu, X., Bhartia, P.K., Krotkov, N.A., Carn, S.A., Hughes, E.J., Krueger, A.J., Spurr, R.J. and Trahan, S.G., 2010. Direct retrieval of sulfur dioxide amount and altitude from spaceborne

hyperspectral UV measurements: Theory and application. *Journal of Geophysical Research: Atmospheres*, 115(D2).

Zibordi, G., Holben, B., Hooker, S., Mélin, F., Berthon, J.F., Slutsker, I., Giles, D., Vandemark, D., Feng, H., Rutledge, K. and Schuster, G., 2006. A network for standardized ocean color validation measurements.

Zibordi, G., Mélin, F., Berthon, J.F., Holben, B., Slutsker, I., Giles, D., D'Alimonte, D., Vandemark, D., Feng, H., Schuster, G. and Fabbri, B.E., 2009. AERONET-OC: a network for the validation of ocean color primary products. *Journal of Atmospheric and Oceanic Technology*, 26(8), pp.1634-1651.

